A study on synthesis and assembly of metallic nanostructures for plasmonic gas sensors

郭, 昊

A study on synthesis and assembly of metallic nanostructures for plasmonic gas sensors

Hao Guo

Graduate School of Information Science and Electrical Engineering
Kyushu University

This dissertation is submitted for the degree of
Doctor of Engineering

January 2025

Abstract

Optical sensing technology has found extensive applications across multiple fields owing to its ultrahigh sensitivity, real-time response characteristics, and non-destructive detection advantages. Surface Plasmon Resonance (SPR), serving as an effective tool for investigating optical properties of nanomaterials and biomaterials, achieves ultrasensitive detection of molecular surface changes through resonant coupling between incident light and free electrons on metallic surfaces. This unique detection mechanism has driven its innovative applications in food safety, drug screening, environmental monitoring, and medical diagnostics. While Localized Surface Plasmon Resonance (LSPR) and Surface-Enhanced Raman Scattering (SERS) technologies based on the plasmonic sensors have achieved major breakthroughs in biomacromolecule detection, traditional applications have primarily been confined to macromolecular systems, with efficient detection of small molecules such as gases remaining a significant challenge.

The optimization of sensor performance mainly relies on rational design of plasmonic nanostructures and precise control of their surface properties. Through careful engineering of material composition and nanoscale architecture, significant improvements in detection sensitivity and response characteristics can be achieved. This research focuses on enhancing nano plasmonic-based gas sensing performance through material design and fabrication methods.

The thesis comprises five chapters, with the main contents:

Chapter 1 describes an overview of the research background, systematically introducing various gas sensing technologies and focusing on the detection principles, existing detection strategies, and fabrication methods of plasmonic nanosensors.

Chapter 2 introduces a fabrication approach for plasmonic nanosensors based on Au@Ag core-shell nanoarchitectures. The synthesis protocol begins with the controlled preparation of Au nanoseeds on glass substrates through thermal dewetting, followed by plasmon-enhanced photochemical deposition of Ag shells. Under visible light irradiation, the localized surface plasmon resonance of Au nanoseeds generates enhanced electromagnetic fields that

direct the selective reduction of silver ions, enabling precise control over the formation of uniform Ag shells.

Chapter 3 presents an advanced plasmonic nanosensors design incorporating metal-organic frameworks (MOF). The sensor is fabricated by in-situ growth of ZIF-8 shells over Au nano-urchin substrates, creating core-shell structures. This hierarchical design was further enhanced by spin-coating a PEDOT: PSS conductive polymer layer, resulting in a multilayer sensor architecture that exhibited significantly improved gas detection performance.

Chapter 4 details a scalable fabrication strategy for plasmonic nanosensors utilizing interfacial self-assembly. The approach begins with the synthesis of monodisperse silver nanoparticles with precisely controlled size. These nanoparticles are then assembled into densely packed monolayers through a sophisticated Marangoni effect-driven oil/water/oil (O/W/O) tri-phase interfacial system. The interfacial tension gradient directs the controlled migration and assembly of silver nanoparticles, while the addition of $TBA^{+}NO_3^{-}$ effectively reduces the Coulomb forces between nanoparticles due to charge effects, enabling more compact nanoparticle arrays. Subsequently, by integrating the fabricated sensors with SERS detection technology, we achieved partial visualization of gases.

Chapter 5 summarizes the main research findings and provides perspectives on future research directions.

Table of contents

List of figures

List of tables

List of Symbols and Abbreviations

C	Concentration
Dr	Diffusion rate
F	Detection flow rate
K	The factor for converting gas weight to volume
t	Gas temperature
M	Molecular weight
P	Gas pressure
VOCs	Volatile organic compounds
LDA	Linear discriminant analysis
PCA	Principal component analysis
APTES	3-aminopropyl triethoxysilane
MISGs	Molecularly imprinted sol-gels
TBOT	Titanium butoxide
$TiCl_4$	Titanium chloride
TEOS	Tetraethoxysilane
$R_{normalized}$	Normalized response
SEM	Scanning electron microscope
ΔA	The change of absorption
A_{air}	Absorption in air
A_{gas}	Absorption in gas
R	Reflection
Ag NPs	Ag nanoparticles
E-nose	Electronic nose
LSPR	Localized surface plasmon resonance
MIP	Molecular imprinted polymer
MOS	Metal oxide semiconductor
MOF	Metal organic framework
ZIF-8	Zeolitic imidazolate framework
TC	Trisodium citrate
CTAB	Hexadecyl trimethyl ammonium Bromide
DMSO	Dimethyl sulfoxide

PEDOT: PSS	Poly(3,4-ethylenedioxythiophene) polystyrene sulfonate
OB	Olfactory bulble
OM	Odor map
OR	Olfactory receptor
QCM	Quartz crystal microbalance
RI	Refractive index
SERS	Surface-enhanced Raman scattering
MFC	Mass flow controller
AA	L-ascorbic acid
4-ATP	4-aminothiophenol
EBZD	4-ethylbenzaldehyde
BZD	Benzaldehyde
UV-vis	Ultraviolet-visible
LB	Left-Bottom
RU	Right-Up
RB	Right-Bottom
NMF	Non-negative matrix factorization
CNN	Convolutional neural network

Chapter 1

Introduction

1.1 Olfactory and Olfactory System

Olfaction, as one of the fundamental sensory systems in living organisms, plays an irreplaceable role in life activities [1]. Recent studies have revealed the remarkable molecular recognition capabilities of the olfactory system: among over 400,000 known chemicals that can trigger olfactory perception, humans can distinguish up to a trillion different odor combinations [2]. Richard and Buck's discovery of olfactory receptors and their elucidation of olfactory system organization pioneered a new era in understanding olfactory mechanisms at the molecular level [3]. They identified a gene family of approximately 1,000 members encoding different types of olfactory receptors, which are distributed across olfactory neurons in the nasal epithelium and responsible for detecting inhaled odor molecules.

The olfactory bulb, serving as the primary processing center for olfactory information, has provided crucial insights into biological olfactory mechanisms through studies of its neuronal activity patterns. As illustrated in **Figure 1.1a**, olfactory information processing begins with volatile chemicals binding to receptors on sensory neurons in the nasal olfactory epithelium. This process requires initial absorption of odor molecules by nasal mucus, followed by interaction with specific receptors on olfactory cilia [4]. Receptor potentials are conducted via neurons to the olfactory bulb for primary processing, ultimately forming neuronal activation patterns reflecting molecular characteristics of odors, known as "odor maps." This spatial encoding pattern serves as the basis for mammals to differentiate and identify various odors.

Artificial gas sensing systems are designed to mimic biological olfactory systems. These systems convert chemical information, such as gas composition and concentration, into measurable electrical signals through sensing units. Different sensing units exhibit differentiated response characteristics to target gases, thereby constructing specific response spectra (chemical fingerprints). Accurate identification of different gases can be achieved through analysis of

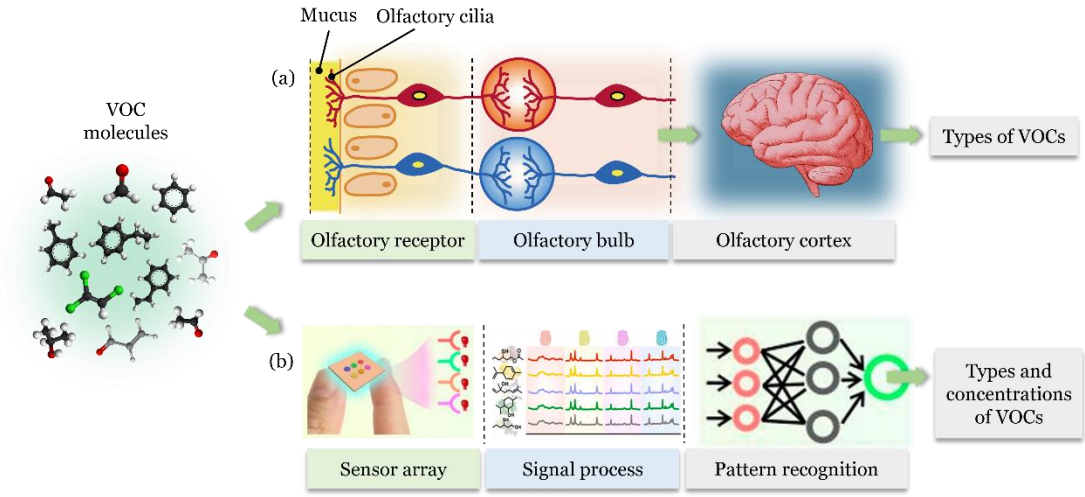

Figure 1.1 Composition and working principles of biological and artificial olfactory systems: (a) biological olfactory system, (b) artificial gas sensing system.

these characteristic fingerprints using appropriate pattern recognition algorithms.

As shown in **Figure 1.1 b**, artificial gas sensing system consists of three main parts: gas sensor array, a signal preprocessing module [5], and a pattern recognition module. The gas sensor array, serving as the core sensing unit, mimics the function of numerous olfactory receptors in biological nasal cavities. Each sensing element in the array converts chemical information (such as composition and concentration) into measurable electrical signals through physical adsorption, chemical reaction, and desorption processes with target gas molecules. The signal preprocessing unit, analogous to the primary information processing function of the olfactory bulb, is responsible for systematic processing of raw signals from the sensor array. This includes digital filtering to remove interference signals, noise reduction to improve signal-to-noise ratio, and feature extraction to obtain key parameters most representative of gas characteristics. The pattern recognition system corresponds to advanced information processing in the cerebral cortex, analyzing preprocessed feature data through mathematical models and algorithms. This module achieves qualitative identification and quantitative analysis of gases, ultimately outputting detection results.

1.2 Gas sensing application

Gas sensors represent a critical class of analytical instruments for identifying and analyzing chemical compositions of gaseous substances, encompassing gas chromatography-mass spectrometry systems [6-8], catalytic combustion sensors [9,10], electrochemical sensors [11,12], colorimetric sensor arrays [13], and optical gas sensors [14-16]. As shown in **Figure 1.2**, these devices play irreplaceable roles in environmental monitoring, food safety, medical diagnostics, and national defense security.

In industrial production environments, the preparation, storage, and transportation of hazardous materials pose potential leakage risks, including harmful gases such as alkanes [17], aromatic hydrocarbons [18], alcohols [19], hydrogen [20], hydrogen sulfide [21], and carbon monoxide [22]. Once leaked, these substances rapidly create environments with explosive or toxic hazards. Gas sensing systems provide effective safeguards for industrial safety through real-time monitoring and alarm capabilities.

In food safety applications, gas sensors provide innovative solutions for food quality monitoring. For instance, meat and seafood products emit volatile amines, aldehydes, and sulfur compounds during spoilage [23-25], while fruits and vegetables release ethylene, alcohols, and esters during ripening and decay processes [26-28]. Real-time monitoring of these signature gas concentration changes enables effective assessment of food freshness and safety. Additionally, gas sensing systems can detect packaging integrity and storage conditions, identifying potential risks such as microbial contamination and mycotoxin production, providing technical support for comprehensive food quality control. This rapid and non-destructive detection method based on gas analysis not only improves food safety monitoring efficiency but also offers new perspectives for intelligent packaging and cold chain logistics development.

In agricultural applications, gas sensing technology provides effective tools for crop growth monitoring and pest control. Plants release characteristic volatile organic compounds during different growth stages and under stress conditions, serving as important indicators of plant growth status, pathogen infection, and environmental stress. Research has shown that healthy plants and those affected by pathogens or pests emit distinct volatile profiles, enabling early warning of crop health status through real-time monitoring of these

substances using gas sensing systems. For example, in rice pest management, gas sensors can detect volatile changes caused by fungal infections or pest infestations at early stages [29-30], providing guidance for precise pesticide application. Additionally, by monitoring concentration variations of gases such as CO2 and ethylene in greenhouses, optimal crop growth environments can be maintained, improving agricultural production efficiency.

In medical diagnostics, gas sensors demonstrate unique advantages. While traditional disease biomarkers (such as proteins, exosomes, and nucleic acids) show low concentrations in early stages, volatile organic compounds (VOCs) produced through human metabolism can reach alveoli via blood circulation and be expelled through exhaled breath. This discovery has made breath analysis a highly promising non-invasive diagnostic approach. Studies have revealed significant changes in breath composition among patients with chronic airway inflammation, gastric cancer, liver cirrhosis, and breast cancer. Particularly in lung cancer diagnostics, various VOC biomarkers including

Figure 1.2 Schematic of gas sensors for VOCs detection in potential applications.

alcohols, aldehydes, ketones, and aromatic compounds have been successfully identified. Compared to traditional blood tests and tissue biopsies, breath analysis offers advantages in simple sample matrix, non-invasive sampling, high safety, and suitability for frequent testing, providing new perspectives for large-scale disease screening [31-32].

Through advancements in gas sensor technology, these devices are becoming indispensable tools for improving safety and health across various fields, from industrial and environmental applications to food and medical sciences.

1.3 Gas detection Method

1.3.1 Traditional methods

Gas Chromatography-Mass Spectrometry (GC-MS), as a high-accuracy and high-sensitivity analytical method, plays a crucial role in complex mixture analysis. As shown in **Figure 1.3**, this technique separates mixtures through chromatographic columns, followed by molecular ionization, acceleration, and detection using mass spectrometry, enabling precise molecular composition identification. When combined with Solid-Phase Microextraction (SPME), it effectively achieves gaseous sample enrichment and analysis. While this hyphenated technique has found widespread applications in pharmaceuticals [33], food [34], fragrances [35], and biological research [36], its high equipment costs, long analysis cycles, and large instrument size limit its applicability for

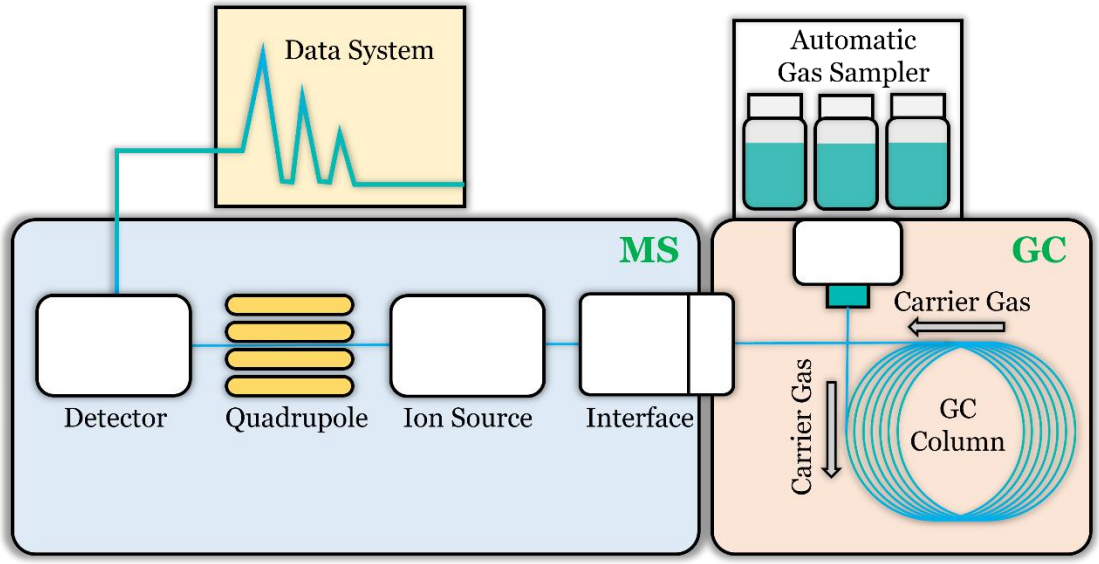

Figure 1.3 Schematic diagram of GC-MS.

real-time monitoring.

1.3.2 Gas sensing methods

Semiconductor gas sensors achieve gas detection by measuring changes in electrical properties induced by interactions between gas molecules and semiconductor materials. These interactions cause alterations in semiconductor conductivity, dielectric constant, and work function, which transform into changes in resistance, capacitance, or inductance signals, enabling quantitative analysis of target gases.

Currently, semiconductor gas sensor fabrication materials primarily include metal oxides, conducting polymers, carbon materials, metal nanoparticles, and their composites. Metal Oxide Semiconductor (MOS) sensors are most common, categorized into p-type (hole conducting) represented by CuO and n-type (electron conducting) represented by WO_3, SnO_2, TiO_2, and ZnO.

MOS sensors operate based on oxygen molecule adsorption and charge transfer processes at material surfaces as illustrated in **Figure 1.4**. In air, oxygen molecules combine with semiconductor surfaces forming charged oxygen ions [37], leading to electron depletion layers in n-type materials and

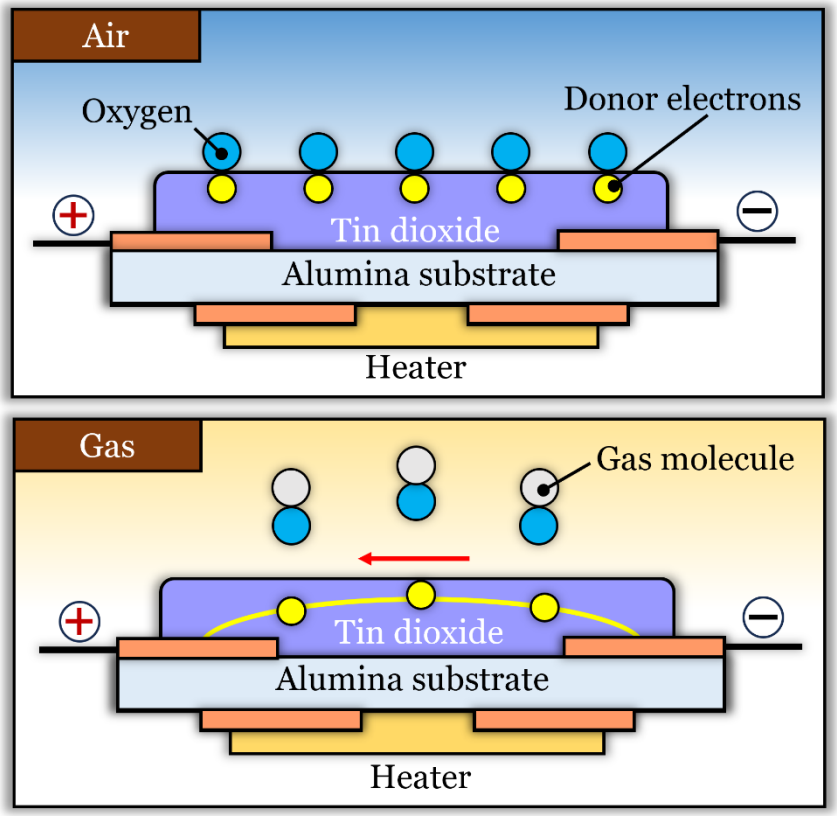

Figure 1.4 Schematic diagram of MOS sensor.

hole accumulation layers in p-type materials. When reducing gases interact with surface oxygen ions, n-type materials show decreased resistance due to thinning of electron depletion layers, while p-type materials exhibit increased resistance from thinning of hole accumulation layers. Oxidizing gases produce opposite effects.

Through material and structural innovations, MOS sensors demonstrate excellent performance in various gas detection applications. For instance, hydrothermally synthesized ZnO nanorods show rapid response and high sensitivity in ethanol detection [38]; electrospun TiO2 nanofibers achieve CO gas detection at 1 ppm levels [39]; and template assisted electrodeposited CuO nanowires demonstrate detection limits as low as 2.5 ppb for H2S gas with excellent reproducibility [40]. Additionally, MOS sensors find broad applications in detecting hydrogen, nitrogen oxides, ammonia, and volatile organic compounds.

Although MOS sensors offer advantages in high sensitivity, good reversibility, low cost, and rapid response, their limitations in selectivity and high operating temperature requirements somewhat restrict their application scope.

Chemical resistive gas sensors have gained widespread adoption due to their simple fabrication process and low cost. As shown in **Figure 1,5**, conducting polymers, serving as active sensing layers, can be controllably

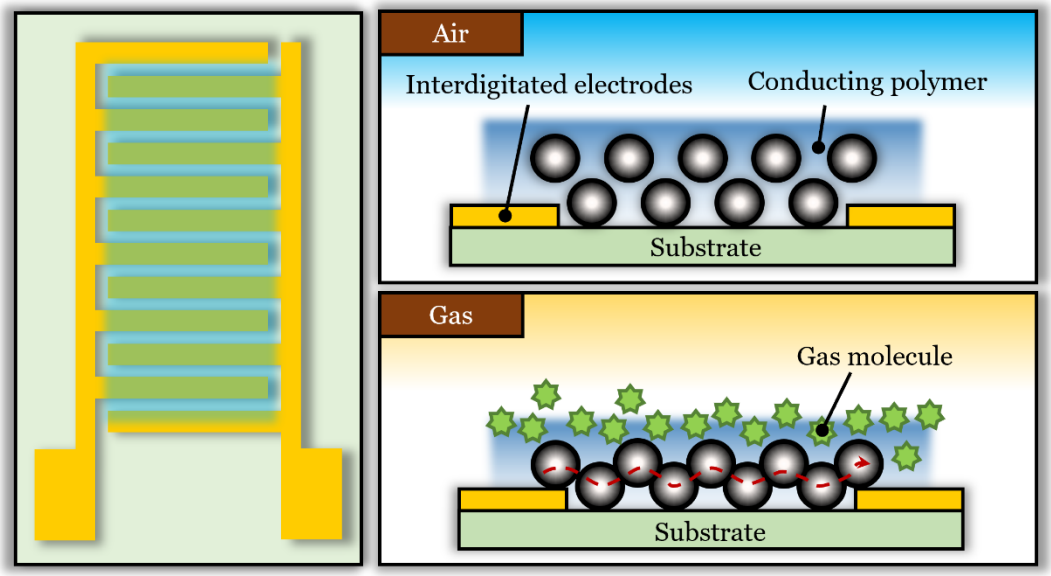

Figure 1.5 Device configuration of chemical resistive gas sensors Coated with conducting polymer films.

deposited on interdigitated electrodes through methods such as spin-coating, drop-casting, or vapor deposition. Research has shown that incorporating conductive materials (such as polypyrrole or carbon black) into polymer matrices significantly enhances sensor sensitivity and selectivity [41]. Gas molecule interactions with polymers induce material swelling, leading to resistance changes that enable gas detection.

Recent years have witnessed significant progress in conducting polymer sensor development: polypyrrole-based flexible sensors have achieved ppb-level ammonia detection [42]; gold nanoparticle-modified conducting polymer transparent films demonstrate excellent performance in organic gas detection [43]; and nanostructured polypyrrole-modified chemiresistor have achieved high sensitivity and selectivity in trinitrotoluene detection (TNT) [44，45]. Conducting polymers offer advantages in easy synthesis, tunable molecular structure, high sensitivity, rapid response, and room-temperature operation, though their service lifetime remains limited.

Quartz Crystal Microbalance (QCM) sensors represent a class of highly sensitive gas detection devices based on mass changes. As illustrated in **Figure 1.6**, their operating principle involves quantitative gas analysis through monitoring resonant frequency shifts caused by gas adsorption on crystal surfaces. While QCMs inherently show low selectivity, surface modification with functional materials (such as polymers [46], metal oxides [47], carbon nanotubes [48], and molecularly imprinted polymers [49]) significantly enhances their selectivity. QCM sensors offer advantages in rapid response,

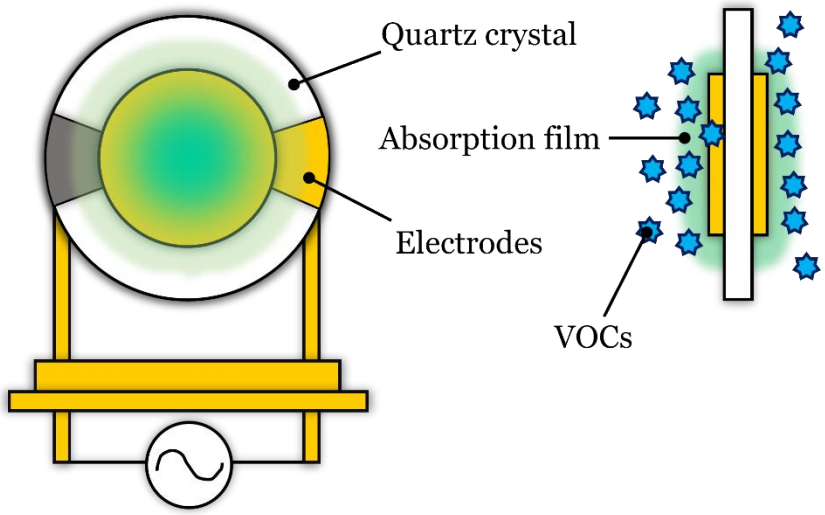

Figure 1.6 QCM sensor for gas detection.

high sensitivity, moderate cost, and room-temperature operation, though their detection accuracy is susceptible to environmental humidity, and sensing material preparation and modification significantly impact sensing performance.

Colorimetric sensing technology based on chemically reactive dyes enables VOCs detection through molecular structure rearrangement. When target VOCs interact specifically with dye molecules, they induce changes in the dye's electronic structure, leading to alterations in optical absorption characteristics manifested as visible color changes [50-53], as shown in **Figure 1.7**. Different dye molecules exhibit differentiated response characteristics to various VOCs, generating unique color change spectra that enable selective detection.

For quantitative analysis, color changes can be converted into RGB three-channel digital signals. However, in low-concentration VOC detection, subtle color changes are often challenging to observe by the naked eye. To enhance detection sensitivity, RGB values are typically mapped from a 0-10 range to a broader dynamic range of 0-255. While this signal enhancement processing improves the distinguishability of minor color changes, it simultaneously amplifies background noise, necessitating optimization of data processing algorithms to balance the signal-to-noise ratio.

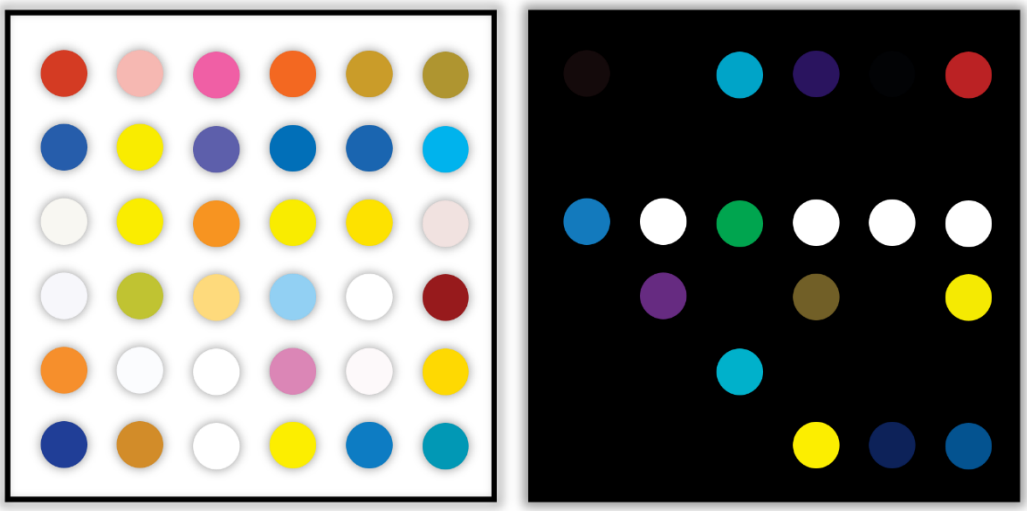

Figure 1.7 Gas detected by colorimetric sensor.

1.3.3 Electronic nose

Electronic nose systems demonstrate unique advantages in gas detection through their rapid response, selective recognition, and stability characteristics.

These sensing systems offer significant cost-effectiveness while enabling seamless integration with existing industrial processes. As previously discussed, the core component of electronic noses is a sensor array that mimics biological olfactory bulb functions, generating differential responses to various odor molecules through multiple sensing units. Combined with pattern recognition algorithms processing complex response signals from the sensor array, odor feature extraction and identification are achieved, simulating biological brain processing of olfactory information.

Currently, commercial electronic noses primarily utilize two types of sensing elements: metal oxide semiconductor (MOS) sensors and conducting polymer sensors. Although these devices show promising prospects across multiple application domains, their performance remains constrained by factors such as stability, selectivity, and reproducibility. Particularly in molecular-level information acquisition, existing sensing platforms still require performance enhancement.

Electronic nose technology applications are rapidly expanding, penetrating diverse fields including agricultural production [54-57], biomedicine [58-60], environmental monitoring [61-64], food quality control [65-67], industrial manufacturing [68,69], military security, pharmaceutical industry, and regulatory enforcement.

With deepening understanding of biological olfactory mechanisms, particularly advances in olfactory receptor functions and odor recognition mechanisms, developing novel sensing units with biomimetic capabilities has become a crucial research direction in this field.

The sensors mentioned above are all summarized in **table 1.1.**

Table 1.1 Comparison of gas sensors based on methods

Methods	Mechanism	Merit	Drawback	Sensitivity	Selectivity	Cost
GC-MS	Separate and identify compounds by their mass	High precision and sensitivity	Expensive, Large size	Excellent	Excellent	High
MOS sensor	Detect gases by conductivity changes on metal oxide surfaces	Fast response, Long lifetime	High operating temperature	High	Surface modification/Algorithm combination	Fair
Chemical resistive sensor	Measures gas through changes in resistance	Easy fabrication, Low cost	Aging problem	Moderate	Chemical polymer	Low
QCM	Detect gases by frequency shift due to added mass on a crystal	Small size, high sensitivity	Easily effected by noise	High	Chemical polymer/Surface modification	High
Colorimetric sensor	Uses color change to indicate gas presence	Visual result, Small size	Irreversible	Moderate	Moderate	Low

1.4 Localized surface plasmon resonance and surface enhanced Raman scattering

Metallic materials play a crucial role in nanoscale device fabrication and emerging technology development. Compared to bulk materials, metallic nanostructures exhibit unique physicochemical properties, with Surface Plasmon Resonance (SPR) being one of their most distinctive characteristics: as shown in **Figure 1.8**, under specific wavelength illumination, collective oscillations of free electrons occur at metal surfaces. Surface plasmons are electromagnetic waves that propagate along conductor-dielectric interfaces and decay perpendicular to the interface. Exciting surface plasmons requires matching conditions between incident photons and plasmons in both frequency and momentum. Since free-space photons typically possess lower momentum than surface plasmons, prism coupling or grating coupling methods are necessary for effective excitation [70,71].

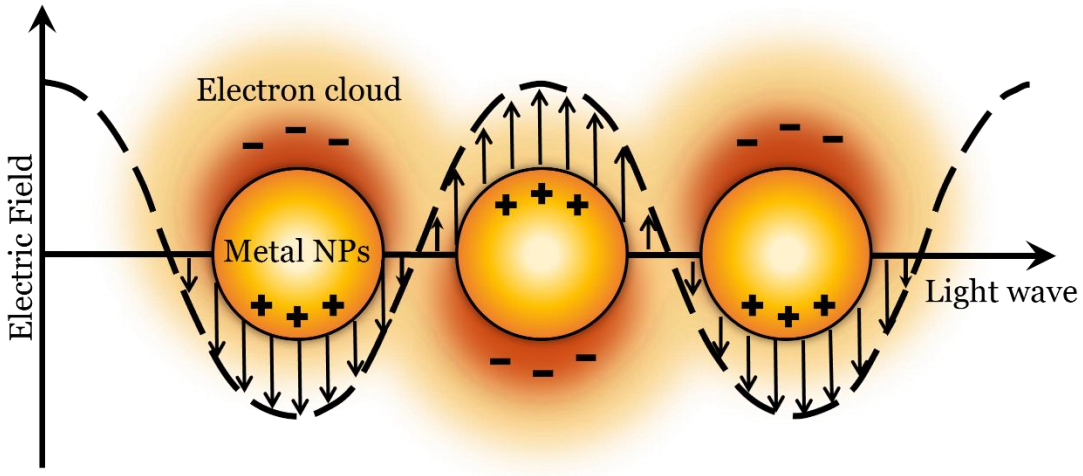

Figure 1.8 Schematic diagrams of Surface plasmon resonance.

SPR detection principles rely on monitoring variations in reflected light intensity with changes in incident angle or wavelength as shown in **Figure 1.9**. This technique offers exceptional detection sensitivity, enabling real-time monitoring of nanoscale thickness changes, refractive index variations, surface chemical reactions, and biomolecular adsorption [72]. SPR-based sensors not only provide high sensitivity but also enable parallel multi-channel detection. Through surface modification with different chemical or biomolecular

recognition units [73-75], SPR imaging techniques can generate enhanced contrast based on differential molecular adsorption.

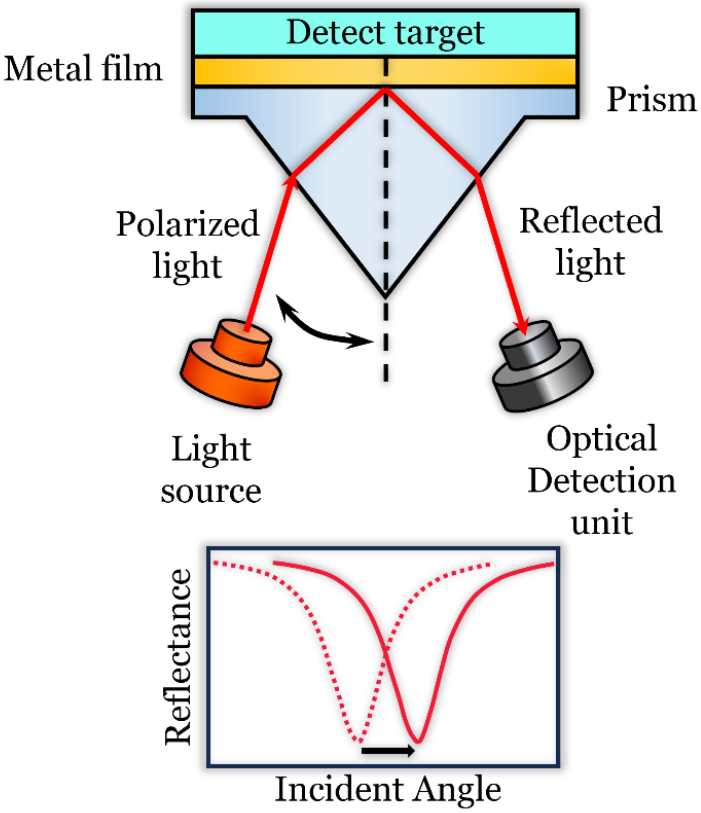

Figure 1.9 Detection based on surface plasmon resonance.

Furthermore, Localized Surface Plasmon Resonance (LSPR) as shown in **Figure 1.10**, can be directly excited through metallic nanostructures without requiring prism or grating coupling. LSPR originates from localized collective oscillations of free electrons in metal nanoparticles, and compared to continuous metal films, nanoparticle systems more readily facilitate LSPR effects [76]. This transmission-based optical detection approach offers advantages in structural simplicity and integration capability over reflective systems, enabling the development of portable detection devices.

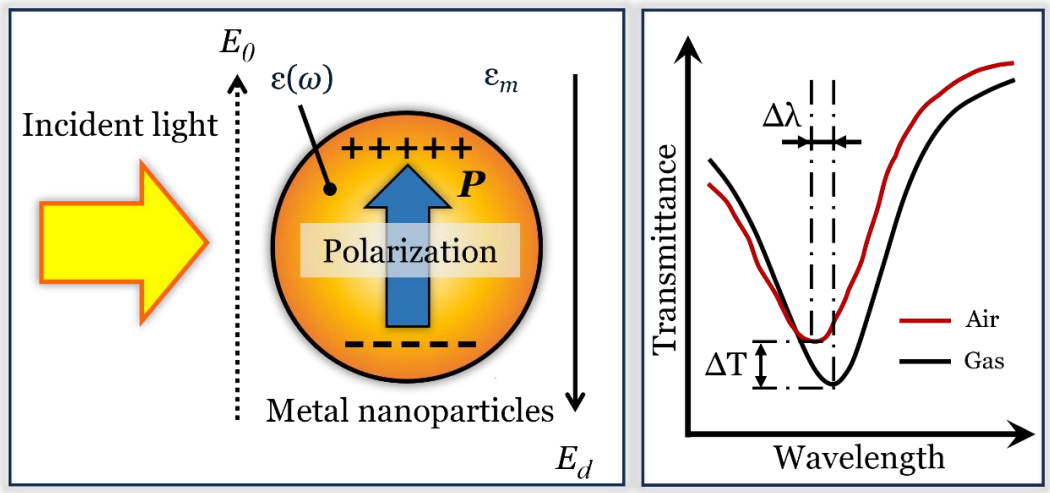

Figure 1.10 Schematic diagram of localized surface plasmon resonance.

Noble metal nanostructures composed of gold, silver, and copper exhibit significant localized absorption characteristics in the UV-visible-near infrared spectral region, with absorption peak positions modulated by nanostructure dimensions, morphology, material composition, and surrounding medium refractive index. These unique optical properties enable LSPR's broad application prospects in chemical sensing, gas detection, and biological analysis. LSPR's high-sensitivity response to environmental refractive index changes provides an effective means for real-time monitoring of molecular-scale interactions.

The detection sensitivity of LSPR devices is primarily determined by material selection, dimensional parameters, and geometric configuration of nanostructures. Through optimization of these key factors, LSPR sensors can achieve detection performance comparable to traditional SPR devices. Currently, thermal annealing represents one of the most common methods for LSPR substrate preparation, enabling controlled nanoparticle growth through precise regulation of annealing temperature, duration, and initial film thickness [77, 78].

LSPR-based photonic devices are also widely employed to enhance various optical processes including Raman scattering, infrared absorption, and fluorescence, etc. Particularly in Surface-Enhanced Raman Spectroscopy (SERS), LSPR effects significantly enhance Raman scattering signals of target molecules through localized electromagnetic field enhancement [79] as shown in **Figure 1.11**. Under optimized conditions, SERS enhancement factors can reach 10^{10} to 10^{11}, achieving ultrasensitive detection at the single-molecule level. This remarkable signal enhancement originates from cooperative interactions between localized plasmons and incident/scattered photon electromagnetic fields

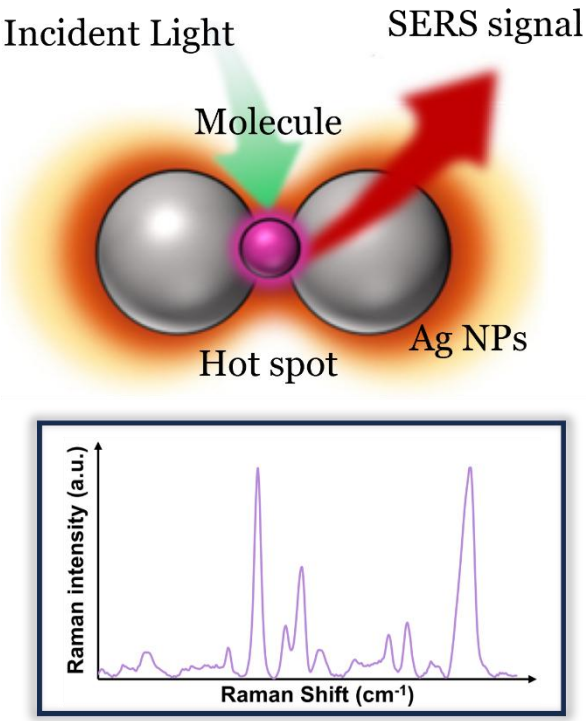

Figure 1.11 Schematic diagram of Raman signal enhanced by surface enhanced Raman scattering technology.

SERS demonstrates exceptional molecular detection capabilities, achieving ultrahigh sensitivity with limits of detection (LODs) typically in the parts per billion (ppb) range and can even reach as low as parts per trillion (ppt) levels through precise design of plasmonic nanostructures [80, 81]. Multiple factors including excitation wavelength, sample characteristics, and testing environment must be comprehensively considered when constructing SERS-active substrates. Developing nanostructures with tunable plasmonic

properties and reliable fabrication processes holds significant importance for expanding SERS applications. Notably, while LSPR sensors primarily achieve detection based on refractive index changes induced by molecular binding, SERS enables qualitative identification through acquisition of molecular vibrational spectral fingerprints. SERS spectroscopy demonstrates significant advantages in molecular recognition and high-throughput detection within complex environments due to its sharp characteristic peaks and unique molecular fingerprint features.

1.5 Research status of plasmonic gas sensors

LSPR sensing technology has experienced significant development in gas detection. Compared with biomolecule detection, achieving high-sensitivity gas sensing at room temperature is more challenging because the refractive index of gas molecules, such as volatile organic compounds (VOCs) and inorganic gases (e.g., n (ethanol) = 1.000878, n (CO_2) = 1.000449, n (NH_3) = 1.000376, and n (CH_4) = 1.000444), are close to that of air (n (air) = 1.000292) [82]. Early studies demonstrated the reversible LSPR signal response of silver nanoparticles in H_2 (n (H_2) = 1.000132) and CO (n (CO) = 1.000336) [83-86], revealing the potential of noble metal nanostructures in gas sensing. Subsequently, researchers achieved selective detection of volatile organic compounds through self-assembled monolayer modification [87,88]. More and more groups successfully detected volatile organic compounds through LSPR.

In 2008, Alexander and his team demonstrated a sensor using gold nanoparticles coated with polymer for sensing various gases, including chloroform, toluene, and methanol [89]. Chen. et al. introduced gold nanoparticle substrates prepared through dewetting methods [90,91] exhibited excellent response to terpene gases after thiol modification [92]. Subsequently, they developed a more sensitive gold nano-sea urchin LSPR substrate through solution synthesis-self-assembly [93,94]. In order to improve the molecular

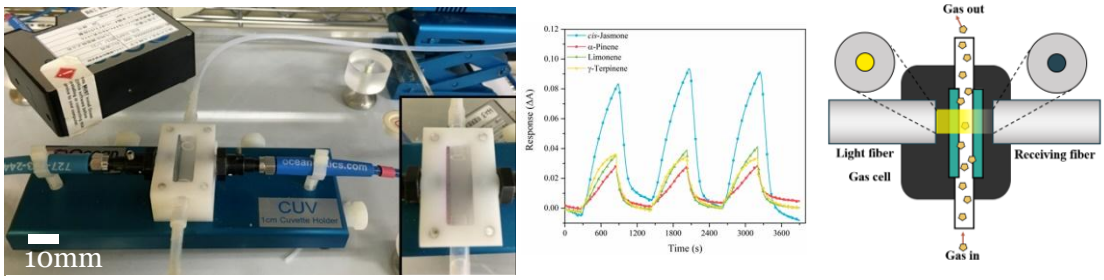

Figure 1.12 Schematic of LSPR optical fiber detection system [95].

recognition ability of the substrate, Chen et al. further integrated molecular imprinting technology with LSPR sensing developed composite sensing substrates with selective recognition capabilities, successfully achieving specific detection of plant volatiles and human organic acids [95-97]; introduction of sol-gel technology improved molecular imprinted polymers to molecular imprinted sol-gel materials, significantly enhancing sensing film stability and selectivity [98-102].

Detection technology has also achieved important advances: evolving from traditional fiber-optic single-point detection ash shown in **Figure 1.12**, to gas distribution visualization technology based on CCD imaging as shown in **Figure 1.13**. This spatially resolved detection method not only obtains gas concentration information but also enables dynamic monitoring of gas diffusion processes. These visualization capabilities provide essential tools for enhancing industrial safety measures and facilitating the use of robots in rescue operations [103, 104].

In terms of SERS sensor VOCs detection. Through the construction of three-dimensional multilayer Ag@MOF core-shell composite structures,

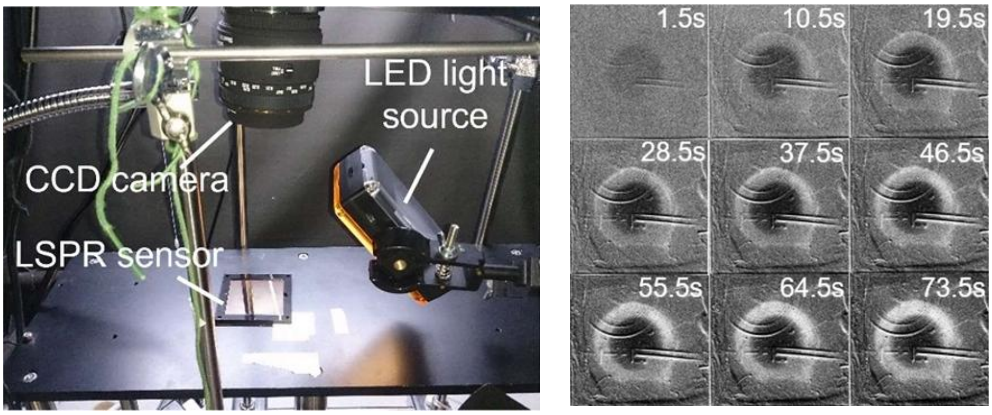

Figure 1.13 Construction of gas visualization detected by CCD camera and "Q" shape odor source visualized [104].

researchers achieved micron-scale hotspot depth and enhanced molecular enrichment capabilities. The integration of this novel sensing substrate with remote Raman systems successfully enabled real-time long-distance detection of multiple target substances in air. Further research combining SERS technology with electrochemical gas sensing achieved quantitative analysis of aromatic hydrocarbons in large-volume open spaces (approximately 60 m^3) with detection distances reaching 5 meters [105].

In biomedical applications, researchers developed a capillary-encapsulated VOC sensor based on Ag@ZIF-67 composite materials. Through cross-validation of 118 clinical samples (including 57 gastric cancer patients and 61 healthy controls), this sensing system achieved 89.83% detection accuracy in gastric cancer diagnosis [106]. Another breakthrough utilized solid-phase extraction technology to prepare multifunctional composite membranes, establishing a highly sensitive sensing platform for detecting aldehyde biomarkers associated with lung cancer, achieving nanomolar-level detection limits (1.35 nM) and providing new perspectives for non-invasive cancer diagnosis [107].

In previous research, Chen et al. constructed single- and double-layer polymer composite film systems on SERS sensing substrates through spin-coating technology [108]. Using polymers with different gas affinities, including polyacrylic acid, poly (methyl methacrylate), and polydimethylsiloxane, precise film deposition was achieved through optimization of spin-coating parameters. By processing SERS spectral characteristic peak intensity information through principal component analysis, we successfully achieved selective recognition and discrimination of structurally similar aromatic compounds, including benzyl alcohol, acetophenone, and anethole.

1.6 Fabrication of plasmonic sensor and surface modification

Gold (Au) and silver (Ag) are commonly used in LSPR/SERS sensing substrate fabrication due to their unique surface plasmon properties. Currently, three main strategies are utilized for noble metal nanostructure substrate preparation:

Solid-state dewetting represents a simple and efficient fabrication method as shown in **Figure 1.14**, where nanoscale metal films are deposited on

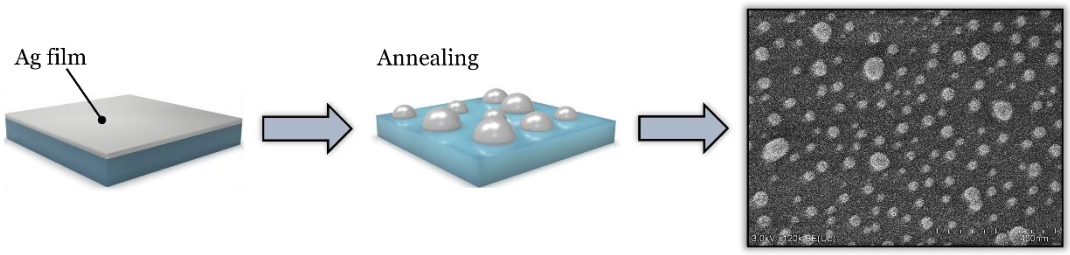

Figure 1.14 Nanofabrication procedure for solid-state dewetting of Ag film.

substrate surfaces and subsequently annealed at appropriate temperatures. This process induces spontaneous formation of uniformly sized nanoisland arrays driven by surface energy minimization principles. Precise control over nanostructure morphology can be achieved through optimization of initial film thickness, annealing temperature, and duration parameters [109-115].

Stencil Lithography technology, as a precise physical preparation method showed in **Figure 1.15**, enables construction of nanoscale patterns with controllable spacing on substrate surfaces, followed by selective metal growth through physical vapor deposition [116-119]. This method allows precise control of nanostructure geometric features (such as shape, size, and gap), yielding highly reproducible sensing substrates, though it involves high equipment costs and complex processing.

Chemical synthesis-self-assembly first prepares metal nanoparticles of specific morphology and size through solution chemistry methods, followed by directed assembly of nanoparticles onto substrate surfaces driven by

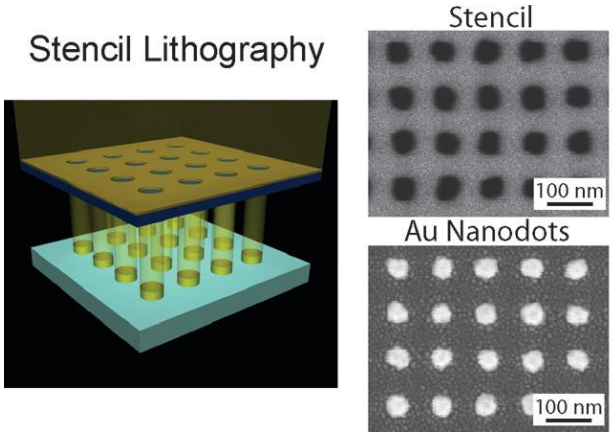

Figure 1.15 Nano-substrate preparation based on lithography technology [116].

electrostatic interactions [120-122] as shown in **Figure 1.16a** and interfacial tension [123-125] as illustrated in **Figure 1.16b**, etc. While this method offers lower costs and scalability potential, it demands stringent control over synthesis processes.

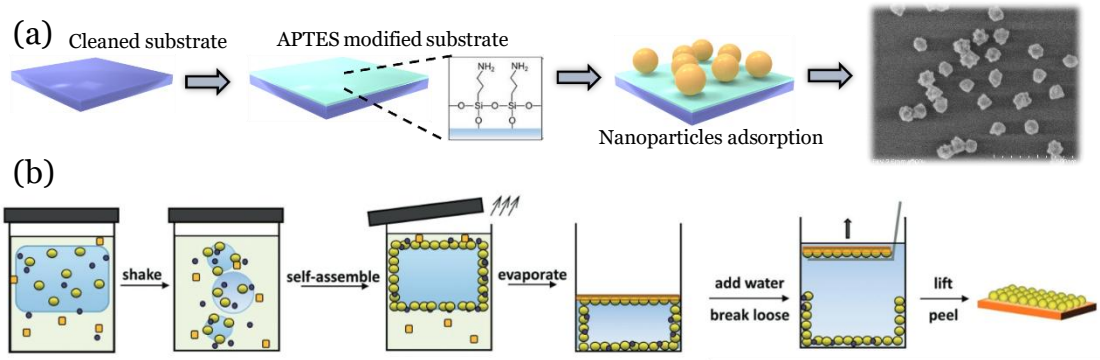

Figure 1.16 Substrate fabrication processes of chemical synthesis-self-assembly (a) electrostatic interactions (b) interfacial tension [123].

To enhance chemical stability and molecular recognition capabilities of sensing substrates, surface modification is typically required. Common modification strategies include thiol self-assembled monolayer construction [126], functional shell coating [128], and molecular imprinting [127], etc. as illustrated in **Figure 1.17**. These surface engineering techniques significantly improve the selective recognition performance of substrates.

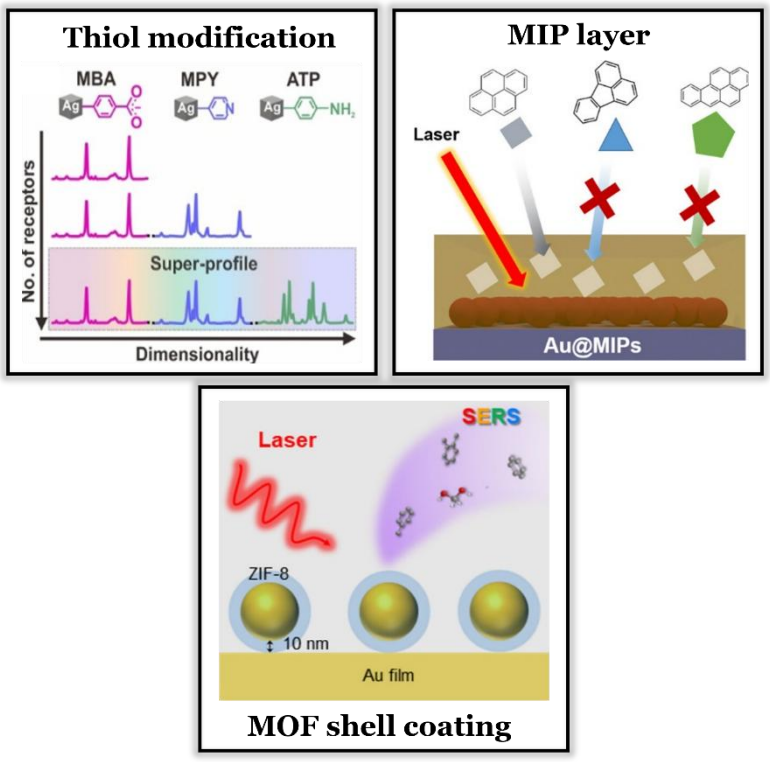

Figure 1.17 Surface modification methods for nanosensors.

1.7 Purpose and novelty

In recent years, plasmonic metal nanoparticle sensors have attracted increasing attention due to their miniature size, excellent sensitivity, and fair cost. However, assembling nanoparticles from solutions onto solid supports remains challenging. In some papers on complex structured nanoparticles synthesized in the liquid phase, the performance of nanoparticles is tested by dropping the nanoparticle solution onto the support substrate and waiting for the solvent to evaporate and dry before testing. Although this method can be used for testing, it is difficult to produce surface plasmon sensors with uniform, large-scale and reproducible distribution of surface nanoparticles. This research aims to develop plasmonic gas sensors using metal nanoparticles on glass substrates by creating plasmonic nanosensors for gas sensing through simple chemical synthesis (in-situ nanoparticle growth) and physical driving methods (surface tension gradient-driven self-assembly).

Novelty:

1. Using in-situ growth methods to create different types of plasmonic gas sensors on glass substrates, including Au@Ag core-shell and Au@MOF core-shell nano structures.
2. Using surface tension differences to drive the interfacial self-assembly of uniform-size silver nanoparticles in solution, forming dense single-layer plasmonic gas sensors.

These methods aim to create structures at the nanoscale while being simple enough for large-scale production of plasmonic gas sensors. Our approach offers practical solutions for making uniform and repeatable plasmonic gas sensors.

1.8 Thesis Organization

The roadmap of the dissertation is illustrated in Figure 1.18.

Chapter 1 provides the theoretical foundation, reviewing biological olfactory models and gas sensing mechanisms with a focus on the fundamental characteristics and fabrication methods of plasmonic sensors.

Chapter 2 presents the development of Au@Ag core-shell nanostructures through a simple yet effective synthesis method. enabling enhanced electromagnetic field amplification through metal-metal coupling for improved plasmonic sensors for gas sensing.

Chapter 3 complements the electromagnetic enhancement approach of Chapter 2 by exploring another crucial aspect of gas sensor performance: gas

molecule adsorption capability. We integrated porous MOF materials by in situ growing ZIF-8 structures on metallic nanoparticles. This strategy significantly enhanced the gas adsorption capabilities and overall sensing performance.

Chapter 4 addresses a key limitation of the sensors discussed in Chapters 2 and 3: while capable of high-speed sensing, they were unable to identify gases. By developing highly uniform plasmonic sensors through triphasic self-assembly and utilizing the molecular fingerprinting capability of SERS detection technology, we achieved gas visualization.

Chapter 5 summarizes the experimental works and outlines future research directions.

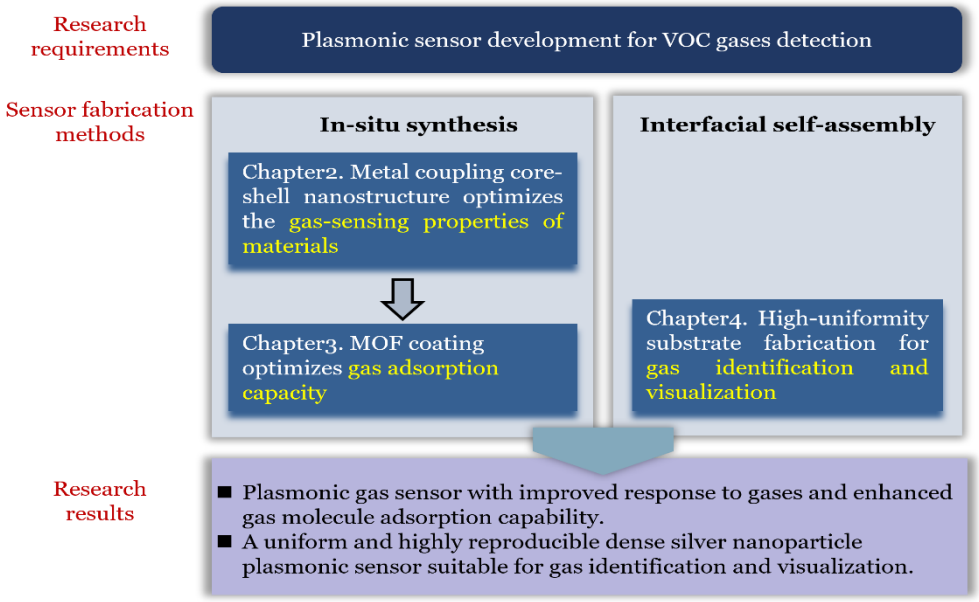

Figure 1.18 Roadmap of the thesis.

Chapter 2

2. Visible light-induced synthesis of Au@Ag core-shell nanostructures for plasmonic gas sensor

2.1 Introduction

Bimetallic nanoparticles exhibit unique physicochemical properties and surface characteristics due to the synergistic interactions between the electronic states of two metals, which are distinctly different from their monometallic counterparts. Extensive research has been conducted on the morphology, size, and shape-dependent properties of monometallic nanoparticles. Bimetallic nanostructures can adopt various configurations, including alloys, one-dimensional nanowires, dendritic structures, and core-shell architectures. Among these nanostructures, Au@Ag core-shell nanostructures have attracted considerable attention due to their unique surface plasmon resonance properties, excellent catalytic activity, and potential applications in sensing [129-131].

In this chapter, I present a simple and efficient method for synthesizing Au@Ag core-shell nanomaterials, as illustrated in **Figure 2.1a**. The synthesis protocol involves the precise control of Au nanoseed formation on glass substrates through thermal dewetting, followed by plasmon-enhanced photochemical deposition of the Ag shell. Under visible light irradiation, the localized surface plasmon resonance of Au nanoseeds generates enhanced electromagnetic fields, which significantly accelerate the reduction rate of silver ions in the vicinity of Au nanoparticles, enabling precise control over Ag shell formation. For gas detection applications, as shown in **Figure 2.1b**, I have developed an innovative reflective fiber-optic probe system that integrates both incident and receiving fibers on the same side, not only simplifying the system architecture but also providing a promising way for the development of portable gas detectors.

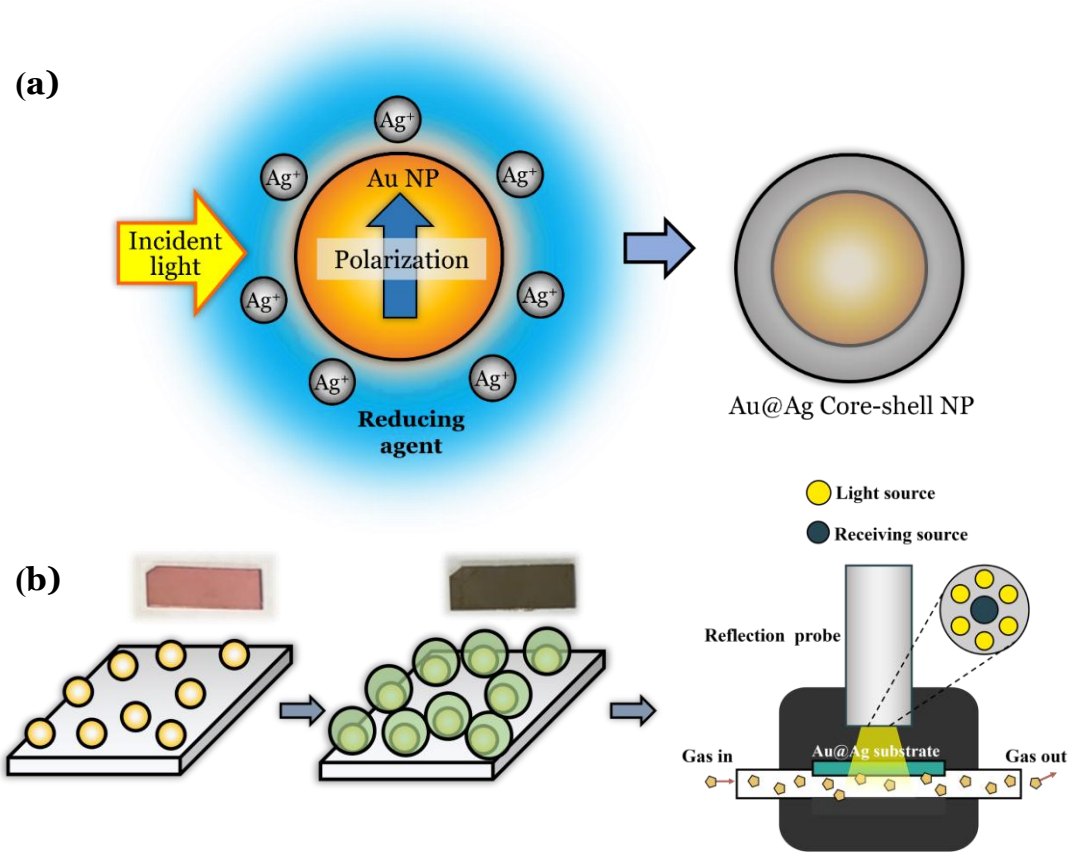

Figure 2.1 (a) Schematic diagram of in-situ growth of silver shell. (b) construction of reflection probe gas detection platform

2.2 Materials and methods

2.2.1 Materials

Trisodium citrate, silver nitrate ($AgNO_3$), and ethanol were purchased from Wako Pure Chemical Industries Co., Ltd. (Osaka, Japan). All reagents were used as received.

2.2.2 Au nanoseed substrate preparation

A 5 nm Au film was deposited onto pre-cleaned microscope glass slide using a magnetron sputtering system (SC-701HMCII, JEOL, Japan). Subsequently, the Au film substrate was transferred to a preheated tube furnace at 580°C (SMF-1, As One). The sample was then annealed for 5 hours to induce thermal dewetting of the Au film, followed by allowing it to cool naturally to room temperature.

2.2.3 Ag shell growth over Au nanoseed substrate

Figure 2.2 schematically illustrates the plasmon-mediated photochemical deposition process. The growth solution was prepared by mixing aqueous solutions of $AgNO_3$ (10 mM) and trisodium citrate (100 mM) with ultrapure water at a volume ratio of 1 : 1 : 8. Subsequently, Au nanoseed substrates were immersed in the well-mixed growth solution and positioned above a halogen lamp for light irradiation.

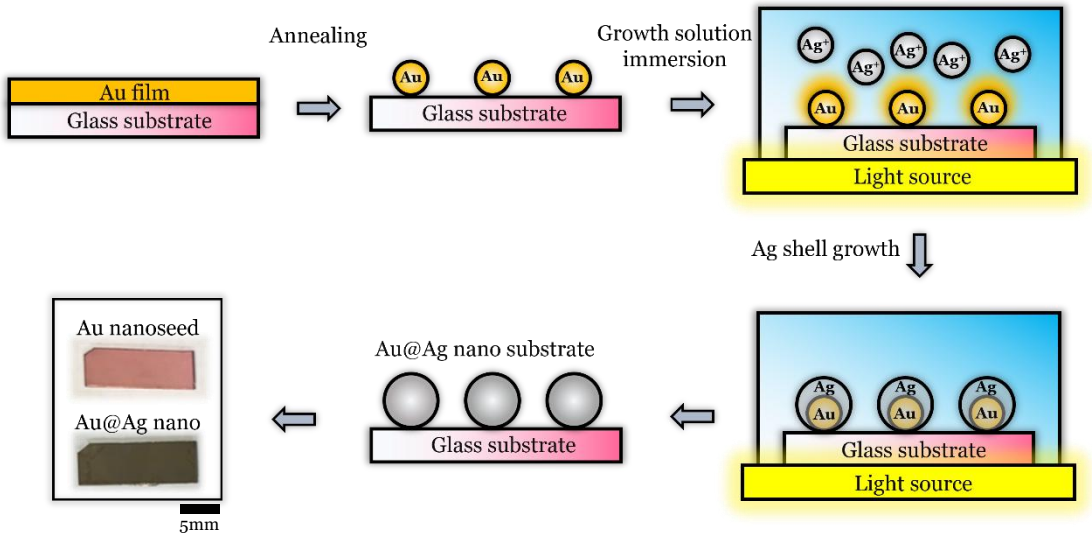

Figure 2.2 Fabrication process of Au@Ag core-shell substrate

2.2.4 Gas detection platform based on reflection probe

The experimental setup for reflectance spectral measurements is illustrated in **Figure 2.3 a**. The composition of the reflection probe is shown in **Figure 2.3 b**, which consists of 1 receiving optical fiber and 6 surrounding illuminating optical fibers.The system primarily consists of a reflection probe (Ocean Optics), a sample holder, and a gas delivery system. The reflection probe is vertically mounted above the sensor substrate through a precision-adjusted holder, maintaining a fixed distance of 10 mm between the probe tip and the substrate surface. 2 mL of acetic acid solution is placed in a 10 mL vial. A micro gas pump is used to blow air into the vial at a flow rate of 0.3 mL/min, generating ammonia gas by the gas blowing method. The target gas is then directionally delivered to the sensor surface from the left side of the setup. When gas molecules diffuse to the vicinity of the sensor surface, their presence directly alters the refractive index of the environment surrounding the metal nanoparticles, which subsequently changes the surface plasmon resonance

characteristics of the sensor. These changes are manifested as shifts in both the position and intensity of the reflected spectrum.

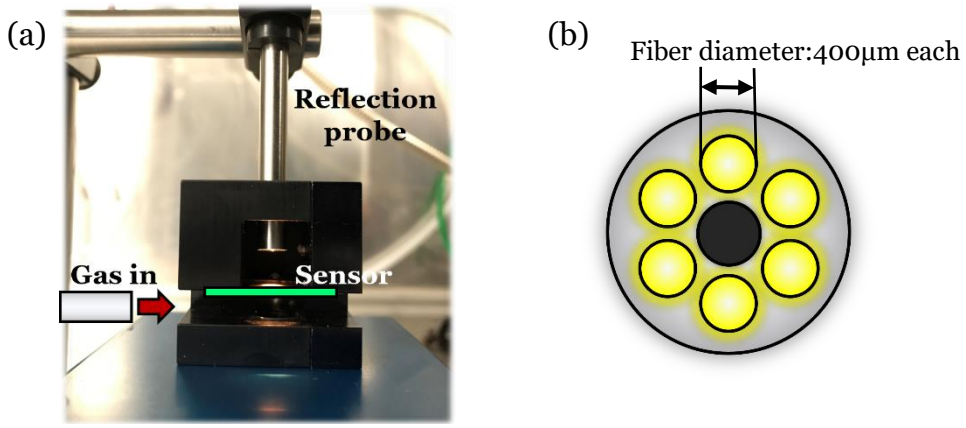

Figure 2.3 (a) Gas detection platform based on reflection probe. (b) reflection probe structure diagram

2.3 Results and discussion

2.3.1 Structure of Au@Ag core-shell substrates

Figure 2.4 illustrates the evolution of the average Ag shell thickness as a function of photochemical deposition time. Morphological characterization using scanning electron microscopy (SEM) of samples at different deposition times (t = 0, 180, 540 min) clearly reveals the progressive increase in Ag shell thickness within the core-shell nanostructures as the reaction time extends. As observed from the leftmost SEM image, the initial Au nanoparticles formed by dewetting exhibit a size distribution ranging from 20 to 30 nm with distinct interparticle spacing. As the Ag shell grows epitaxially, the nanoparticle size gradually increases while the interparticle spacing decreases correspondingly. At t = 180 min, adjacent nanoparticles begin to show signs of aggregation. When the deposition time reaches 540 min, significant particle coalescence and agglomeration are observed throughout the sample surface.

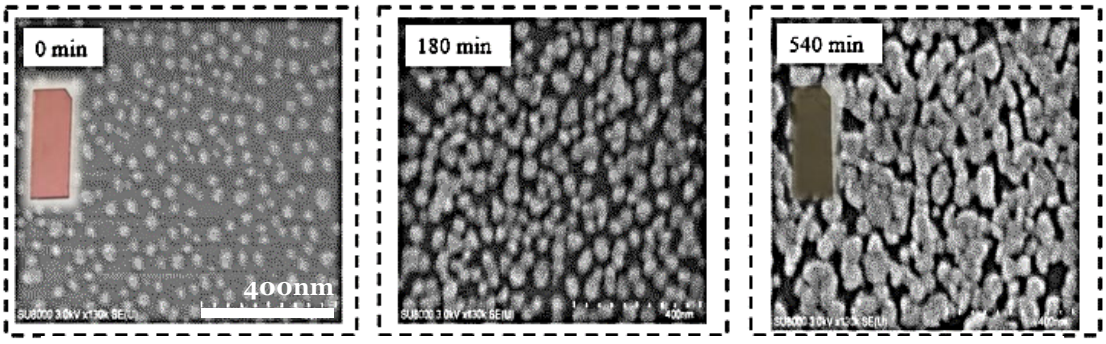

Figure 2.4 SEM images of substrate with different Ag shell growth

2.3.2 Optical characteristics of the substrates

As illustrated in **Figure 2.5**, this study implements an innovative reflective spectral detection mode, which differs from the conventional transmission-based approach where incident and receiving fibers are positioned on opposite sides of the substrate.

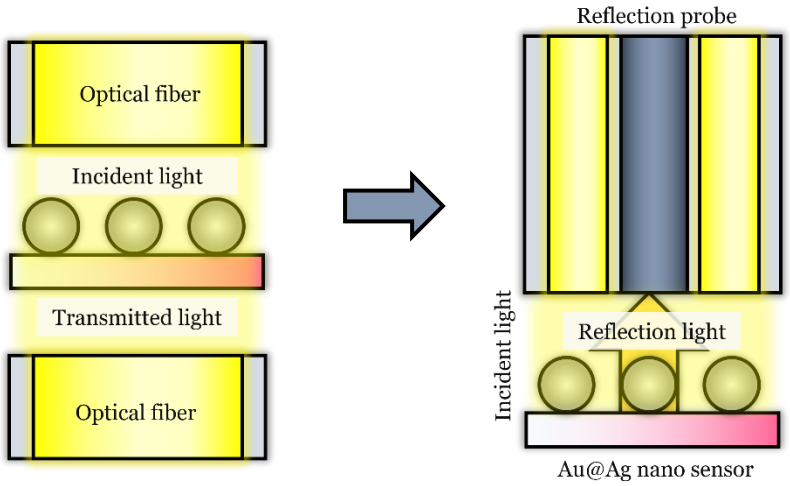

Figure 2.5 Two spectral detection methods: (a) transmittance, (b) reflection.

Figure 2.6 presented a comparative study of two probe placement configurations: one with the reflection probe facing the nanoparticle side (**Figure 2.6a**) and the other facing the glass substrate side (**Figure 2.6b**). Spectral measurements reveal distinct surface plasmon resonance peaks in the wavelength range of 550–600 nm. As the Ag shell growth time increased, the plasmon resonance peak exhibited a blue shift towards shorter wavelengths. Because of the different surface roughness (the nanoparticle side was rougher, and the glass side was smoother), the reflected light detected from different sides would be different. The results in **Figure 2.6b** demonstrated that spectral signals obtained from the glass substrate side showed more well-defined resonance peak characteristics. Notably, in samples with 9-hour Ag shell growth, while the resonance peak became indistinguishable from the nanoparticle side (Figure 6a), a clear resonance feature remains observable from the glass substrate side (Figure 6b). Based on these experimental findings, I opted to conduct spectral measurements from the glass substrate side to achieve higher-quality measurement spectra.

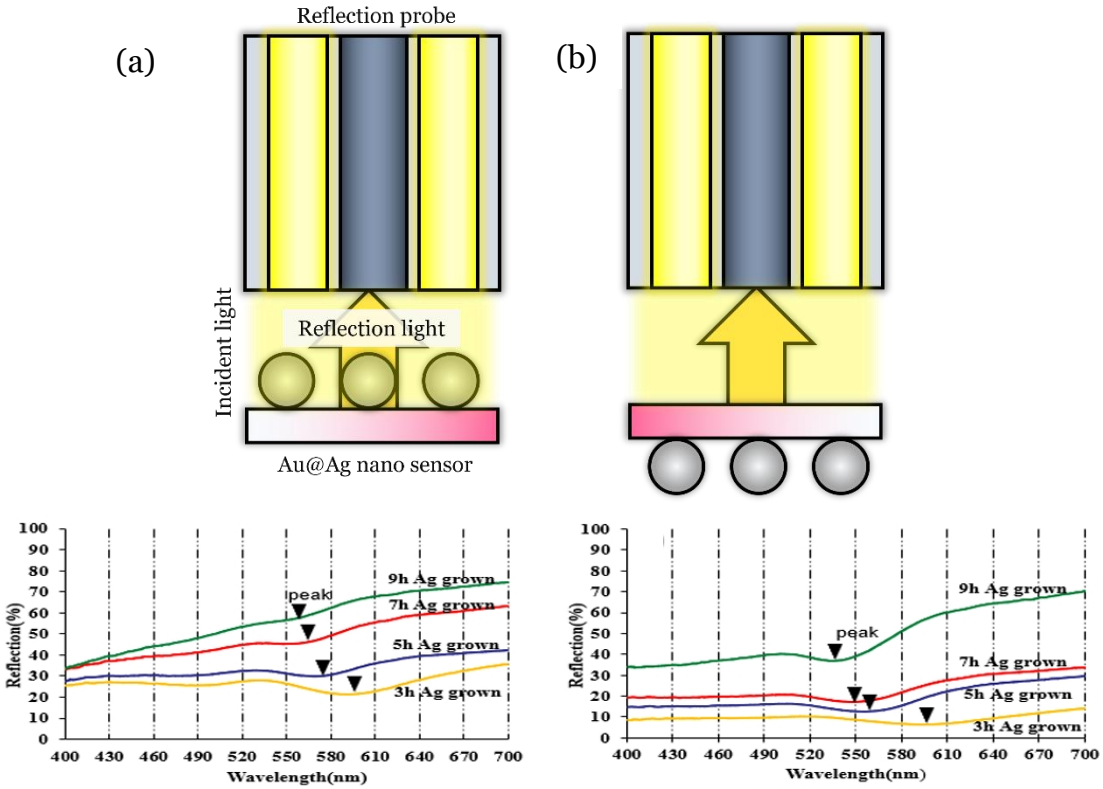

Figure 2.6 Reflection spectra with different side directions of incident light (a) metal nanoparticle side(b) glass side

I further investigated the influence of incident angle between the reflection probe and substrate on spectral detection sensitivity, with results shown in **Figure 2.7**. When the reflection probe was positioned perpendicular to the substrate surface (incident angle θ = 90°), not only was a clear surface plasmon resonance spectrum of the nanoparticles obtained, but the reflectance spectrum also exhibited distinct dynamic response characteristics in the presence of gas molecules. In contrast, when the probe was oriented at an oblique angle to the substrate surface (θ < 90°), the detected reflectance spectral intensity significantly decreased, making it difficult to distinguish characteristic resonance peaks. Based on these experimental findings, I established the optimal detection configuration: the reflection probe positioned perpendicular to the glass substrate side, enabling maximum spectral detection sensitivity.

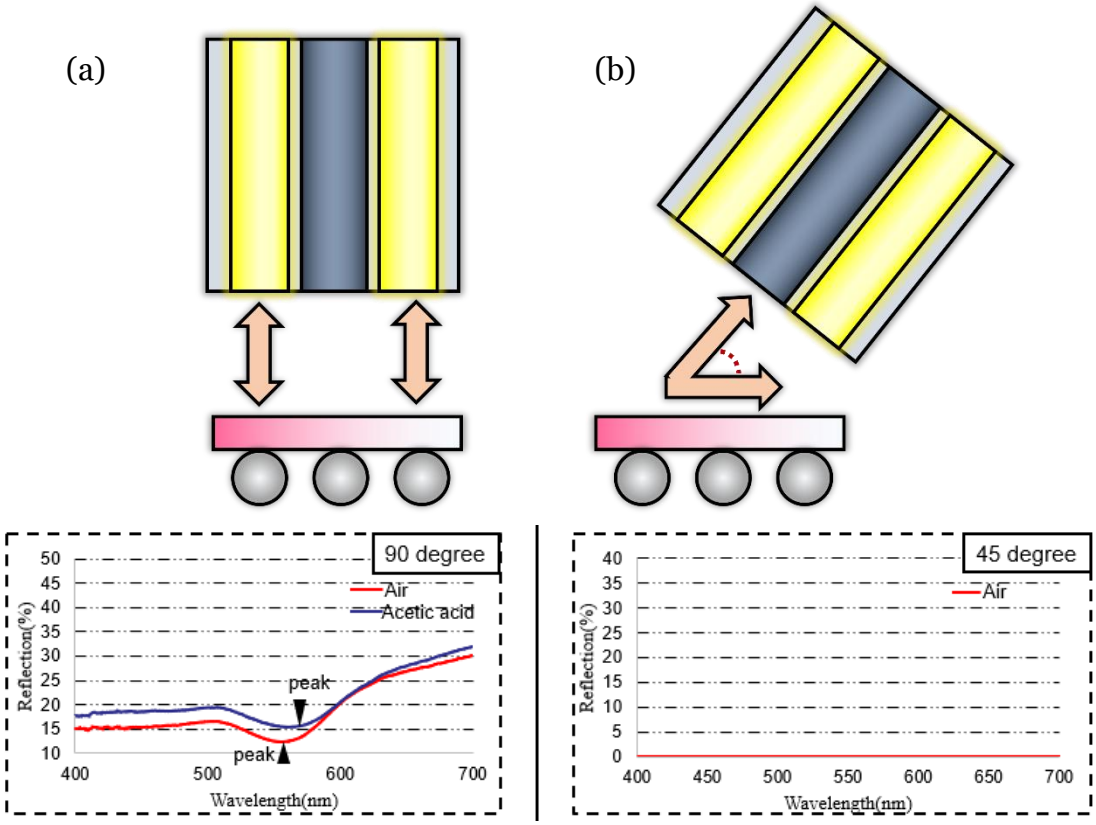

Figure 2.7 Reflection spectra with different probe detecting angels.

2.3.3 Gas detection with reflection system

Acetic acid, a common volatile organic compound characterized by strong irritant and corrosive properties, finds widespread applications in food, fermentation, chemical, and manufacturing industries [133-135]. Given its extensive detection requirements, I conducted sensing studies of acetic acid vapor under room temperature conditions. I systematically investigated the influence of Ag shell growth time on the sensitivity of Au@Ag core-shell nanostructures towards acetic acid gas detection as shown in **Figure 2.8**. The experimental demonstrated that when the Ag growth time increased from 3 to 5 hours, the sensor's response sensitivity to acetic acid improved significantly. However, further extending the growth time to 7 and 9 hours led to a dramatic decrease in detection sensitivity. This non-monotonic sensitivity variation can be attributed to two competing processes: in the initial growth stage, the gradual development of the Ag shell optimizes the plasmonic properties of the Au@Ag core-shell structure, thereby enhancing sensing sensitivity; however, when Ag deposition exceeds a critical threshold, significant particle aggregation

occurs, which weakens the LSPR effect [166], ultimately deteriorating the sensor's detection performance.

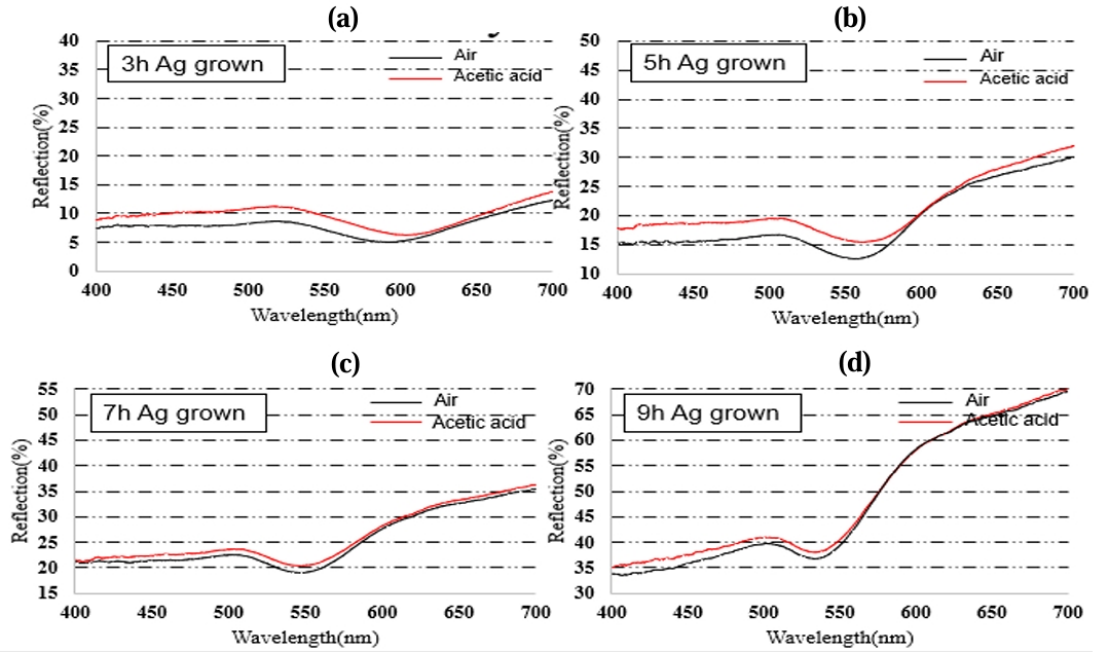

Figure 2.8 Response of 3h Ag shell grown sensor to acetic acid(a), 5h Ag grown (b), 7h Ag grown (c), 9h Ag grown (d)

2.4 Conclusion

In summary, I have successfully fabricated Au@Ag core-shell nanostructures through visible light-induced plasmon-enhanced photochemical reduction. Specifically, size-controlled Au nanoseeds were first prepared on glass substrates via thermal dewetting, followed by the controlled growth of Ag shells through catalytic reduction of Ag^+ ions in the near-field region, accelerated by the enhanced electromagnetic field generated from visible light-excited Au nanoparticles. In terms of sensing detection, this study innovatively employed a reflective spectral detection mode, distinct from conventional transmission-based methods. Through systematic optimization of the reflection probe's incident angle and detection orientation, high-quality reflection spectra of the Au@Ag core-shell nanostructures were successfully obtained. The sensing platform was further applied to detect acetic acid gas, demonstrating the feasibility of gas sensing based on the reflective detection mode, thereby providing crucial experimental foundations for developing novel portable gas sensors.

Chapter 3

3. In-situ Growth of Au@ZIF-8 Core-shell Nanostructures for Plasmonic Sensor Enhanced Gas Sensing

3.1 Introduction

In chapter 2, while I designed Au@Ag core-shell nanostructures in the previous chapter to enhance plasmonic gas sensor sensitivity through metal-metal coupling effects, I also recognized that gas molecule adsorption capability significantly influences sensor performance. Gas sensing based on LSPR faces key challenges are noble metal nanostructures inherently lack enrichment capabilities for gas molecules. To overcome these limitations, researchers have developed functional material composite modification strategies [89] [136].

Early studies primarily employed functional polymer film modification of LSPR sensing substrates [95-102]. While achieving certain progress in sensitivity and selectivity, material adsorption capacity and cycling stability still required improvement. Metal-Organic Framework (MOF) materials demonstrate unique advantages in gas adsorption through their ordered crystal structures, ultrahigh specific surface areas, and tunable pore characteristics [137, 138].

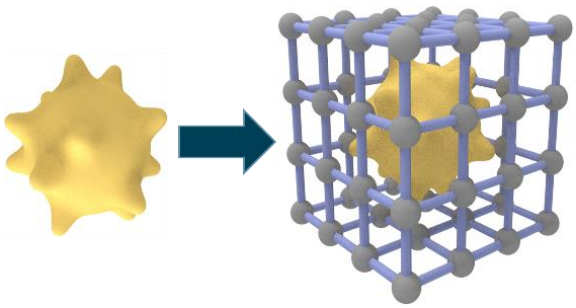

Figure 3.1 Schematic of Au nano-urchin coating MOF.

This study selected Zeolitic Imidazolate Framework-8 (ZIF-8) [139, 140], with its typical topological structure as shown in **Figure 3.1**, as a functionalization layer, developing a new in-situ MOF growth method on nanoparticle surfaces that simplifies device fabrication processes.

To further optimize sensing performance, poly(3,4-ethylenedioxythiophene): poly (styrene sulfonate) (PEDOT: PSS) conductive polymer layer, as shown in Figure 2.2, was introduced into the composite structure. The sulfonic acid groups in PEDOT: PSS molecular structure exhibit specific interactions with ammonia molecules, significantly enhancing the sensor's selective recognition capability for ammonia [141, 142].

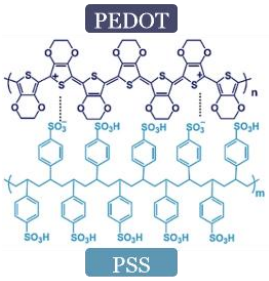

Figure 3.2 Chemical structure of PEDOT: PSS.

As shown in **Figure 3.3**, in this chapter, multi-layer functional material composite design strategy not only improves the comprehensive performance of LSPR gas sensing but also provides new insights for expanding its practical applications.

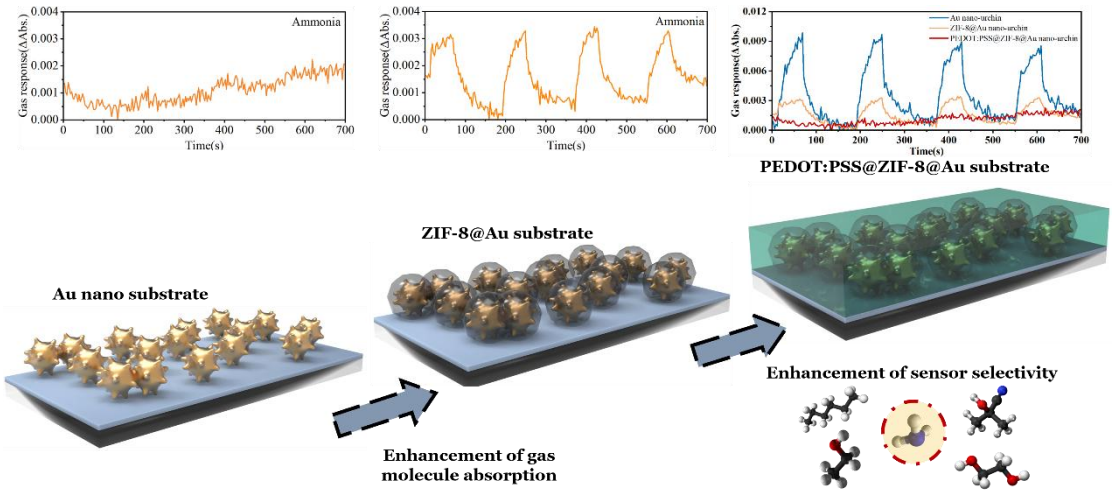

Figure 3.3 The schematic diagram of gas detection using PEDPT：PSS@ZIF-8@Au nano-urchin substrate.

3.2 Materials and methods

3.2.1 Materials

Titanium tetrabutoxide (TBOT), isopropanol, titanium tetrachloride ($TiCl_4$), acetone, trisodium citrate, hydroquinone, and ethanol were purchased from

Wako Pure Chemical Industries Co., Ltd. (Osaka, Japan). (3-mercaptopropyl) trimethoxysilane (APTES) was purchased from Shin-Etsu Chemical Co., Ltd (Tokyo, Japan). $HAuCl_4 \cdot 3H_2O$ was purchased from Sigma-Aldrich (St. Louis, MO, USA). 2-methylimidazole and zinc nitrate hexahydrate were purchased from Sigma Aldrich. All reagents were used as received.

3.2.2 Synthesis of Au nano-urchins solution

The preparation of gold nano-urchins was accomplished through a modified seed-growth method [143]. Gold nanoseeds were first synthesized: 75 μL of chloroauric acid ($HAuCl_4$, 100 mM) solution was added to 30 mL of boiling ultrapure water under vigorous stirring, followed by rapid injection of 900 μL trisodium citrate solution (1 w/v%). The mixture was continuously heated and stirred until displaying the characteristic wine-red color, indicating nanoseed formation, then cooled to room temperature.

Gold nano-urchin growth proceeded as follows: Under vigorous stirring, 25 μL of chloroauric acid solution (100 mM) was mixed with 9.6 mL ultrapure water, followed by sequential addition of 150 μL gold seed solution, 22 μL trisodium citrate solution (1 w/v%), and 1.2 mL hydroquinone solution (30 mM). Growth was completed after 30 minutes of stirring at room temperature.

3.2.3 Fabrication of PEDOT：PSS@ZIF-8@Au nano-urchin substrate

The composite sensing substrate preparation involved multiple steps as shown in **Figure 3.4**: The glass substrate surface was modified with amino groups through APTES functionalization by immersing it in APTES/ethanol solution (1:100 v/v) for 30 minutes, followed by ethanol washing, nitrogen drying, and heat treatment at 120℃ for 3 hours [93]. The APTES-modified glass surface, bearing amino groups (-NH2), can interact with citrate-capped gold nano-urchins through electrostatic attraction. Based on this electrostatic interaction, the modified glass substrate was immersed in the gold nano-urchin solution overnight to achieve self-assembly of nanoparticles on the substrate surface.

The construction of composite functional layers employed a sequential modification strategy. First, substrates loaded with gold nano-urchins were vertically immersed in cetyltrimethylammonium bromide (CTAB) solution (0.1 M, 5 mL) for 1 hour to establish a surfactant molecular layer. After ethanol

washing and nitrogen drying, CTAB-modified substrates were placed vertically in 2-methylimidazole solution (1.3 M, 2 mL), followed by sequential addition of CTAB solution (0.1 M) and zinc nitrate hexahydrate solution (24 mM, 2 mL). ZIF-8 crystal layers were constructed on gold nano-urchin surfaces through in-situ growth by maintaining at room temperature for varying durations.

The final step involved conductive polymer modification: PEDOT: PSS solution was mixed with dimethyl sulfoxide (DMSO) at specific ratios, and 30 μL of the mixture was drop-cast onto ZIF-8@Au nano-urchin substrates and spin-coated at 2000 rpm for 30 seconds. Subsequent thermal treatment at 80°C for several minutes completed the fabrication of PEDOT: PSS@ZIF-8@Au nano-urchin composite sensing substrates.

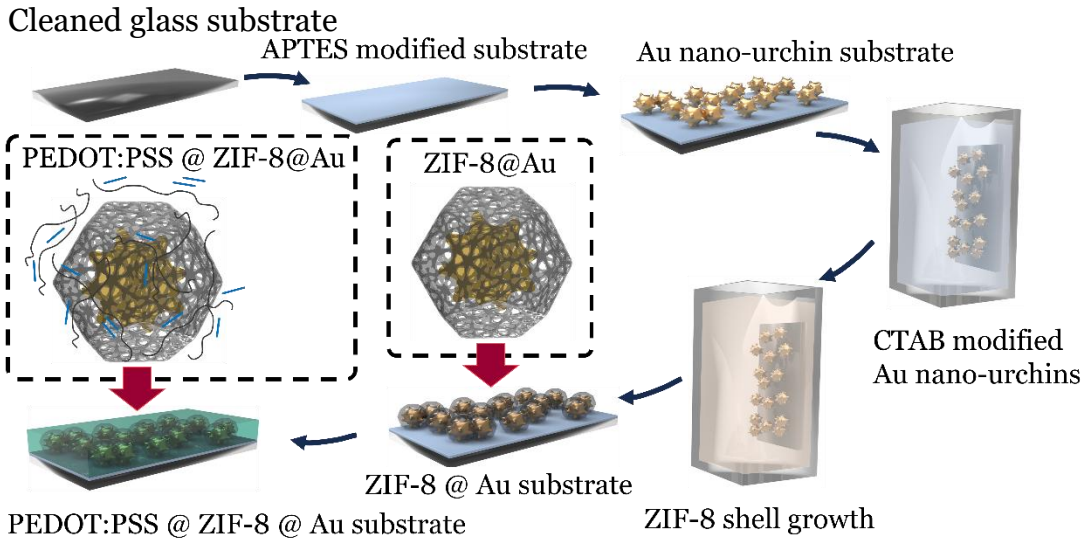

Figure 3.4 Fabrication process of LSPR gas sensor.

3.2.4 Real-time spectra measurement system

The absorption spectral measurement system was shown in **Figure 3.5**, comprises a light source, UV-visible spectrometer, custom-designed Teflon gas detection chamber, optical fiber transmission system, and data acquisition/processing unit. Two optical fibers are positioned on opposite sides of the LSPR sensing substrate: the incident fiber connects to the light source, guiding incident light perpendicular to the substrate surface; the collection fiber links to the spectrometer, capturing transmitted light signals. Real-time monitoring of absorption intensity changes at the plasmon resonance peak was achieved through OPwave+ software (Ocean optics, USA), with absorbance change (ΔA) calculated according to the formula:

$$\Delta A = A_{gas} - A_{air}$$

Here, A_{air} and A_{gas} represent absorbance in air environment and target gas presence, respectively. For different sensing substrates, monitoring was conducted at their characteristic plasmon resonance peaks: 538 nm for bare gold nano-urchin substrates, 552 nm for ZIF-8@Au nano-urchin composites, and 564 nm for PEDOT: PSS@ZIF-8@Au nano-urchin composites.

When gas molecules interact with sensing substrates, local refractive index changes induce plasmon resonance peak shifts, resulting in absorption intensity variations at characteristic wavelengths. Quantitative gas detection is achieved through continuous recording of these absorption intensity changes.

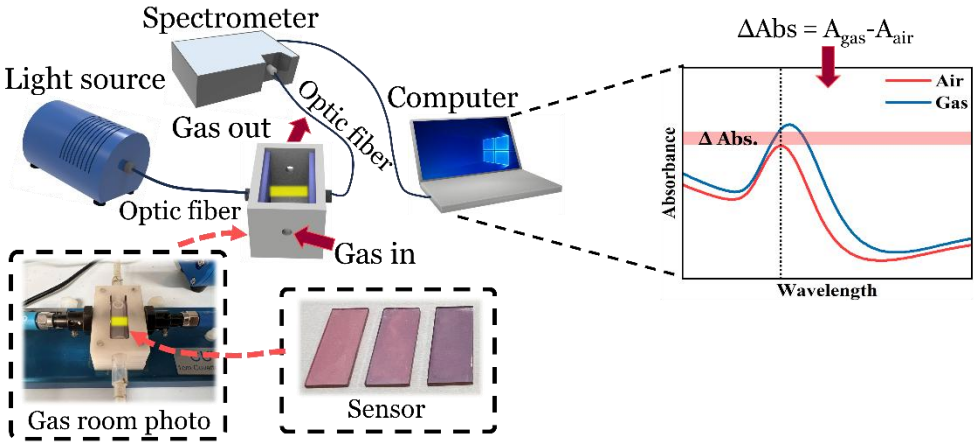

Figure 3.5 Schematics of the optical gas sensing system for absorbance LSPR measurement.

3.2.5 Gas generation system

Gas generation and delivery system showed in **Figure 3.6** consists of: LV-125A micro pump (Linicon, Japan), air purification unit filled with molecular sieves

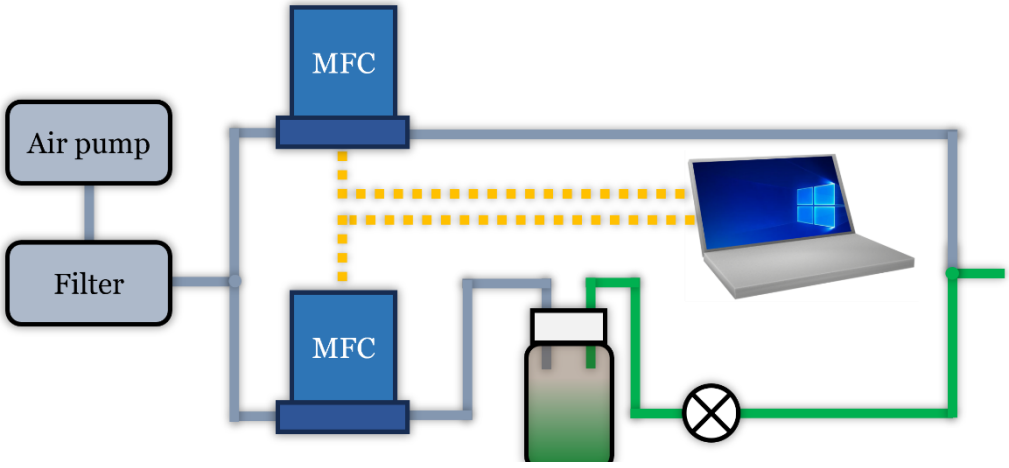

Figure 3.6 Schematics of gas generation system.

and activated carbon, dual-channel 3660 mass flow controllers (Kofloc, Japan), FSM-0408Y three-way solenoid valve (FLON Industry, Japan), 6 mL standard glass sampling vial, and control terminal. The system utilizes purified dry air as carrier gas, with all connections achieved through inert polytetrafluoroethylene tubing. Precise control of mass flow controllers and solenoid valves is implemented through USB-6009 data acquisition card (National Instruments, USA) and customized LabView programming.

3.3 Results and discussion

3.3.1 Structure of ZIF-8@Au nano-urchin substrates

Surface morphological evolution of gold nano-urchin substrates during ZIF-8 growth was systematically investigated using scanning electron microscopy (SEM) as shown in **Figure 3.7**. Prior to ZIF-8 growth, the substrate surface exhibited uniformly distributed arrays of gold nano-urchins, each nanostructure featuring distinctly sharp protrusions. While minor aggregation existed in localized areas, nanoparticles maintained good separation, with substrate surfaces remaining clean except for the nanostructures.

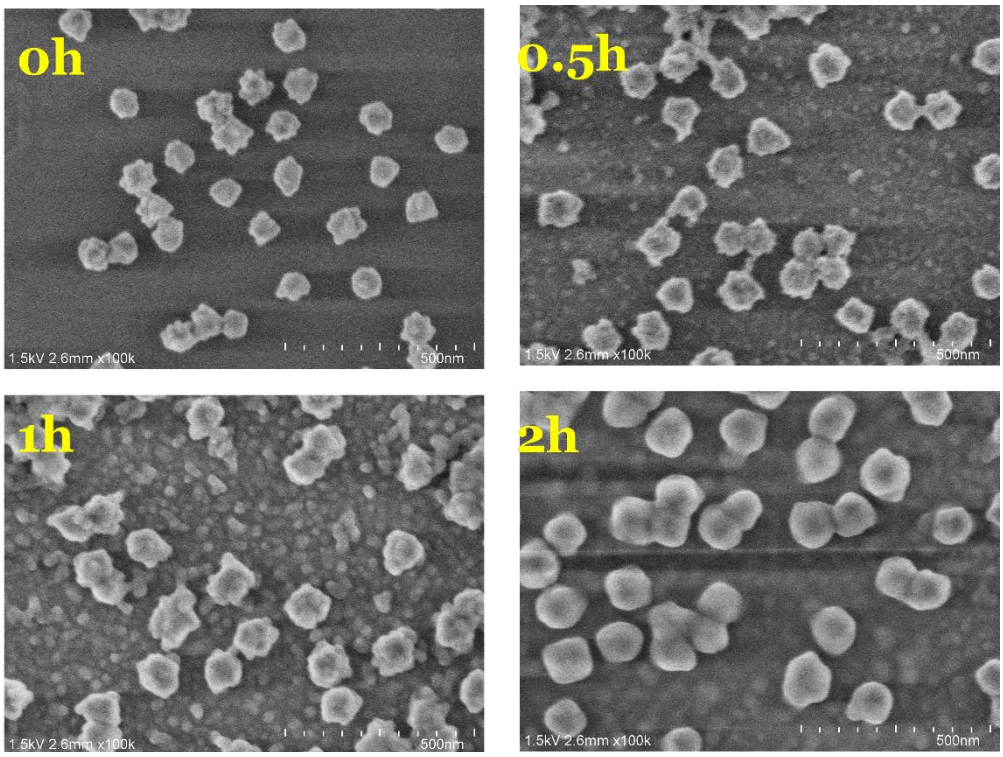

Figure 3.7 SEM images of the Au nano-urchin substrate with different time ZIF-8 growth.

After 30 minutes of growth, the sharp features of nano-urchins began to diminish, accompanied by the appearance of numerous fine particles. This morphological transformation primarily resulted from CTAB-mediated ZIF-8 nucleation. As growth extended to 1-hour, abundant ZIF-8 crystallites not only formed on the glass substrate surface but also achieved encapsulation of gold nano-urchins, leading to significant increase in overall nanostructure dimensions. Notably, previously separated nanoparticles began forming connections through ZIF-8 crystals, with this bridging effect becoming increasingly prominent as ZIF-8 growth proceeded.

Following 2 hours of growth, nanostructure morphology underwent fundamental transformation, evolving from original urchin-like to cubic characteristics. Initial sharp protrusions completely disappeared, with adjacent nanoparticles effectively merging through ZIF-8 crystals, confirming successful construction of the ZIF-8 shell layer.

3.3.2 Optical characteristics of the substrates

Growth process dynamics were monitored through UV-visible absorption spectroscopy. As shown in **Figure 3.8a**, initial gold nanoseeds exhibited plasmon resonance peak at 519 nm, experiencing significant red-shift to 580 nm secondary growth into urchin structures. Upon self-assembly deposition onto glass substrate surfaces, the resonance peak further adjusted to 538 nm.

To optimize ZIF-8 growth conditions, comparative studies investigated CTAB modification's influence on growth processes. As shown in **Figure 3.8b**, under identical growth conditions, CTAB-modified gold nanoparticle surfaces demonstrated enhanced ZIF-8 growth kinetics, forming more uniform and complete encapsulation layers, while unmodified substrates exhibited heterogeneous growth characteristics.

Further kinetic studies revealed ZIF-8 growth primarily concentrated within the first 2 hours, as shown in **Figure 3.8c**, manifested through continuous plasmon resonance peak red-shifts and steady absorption intensity

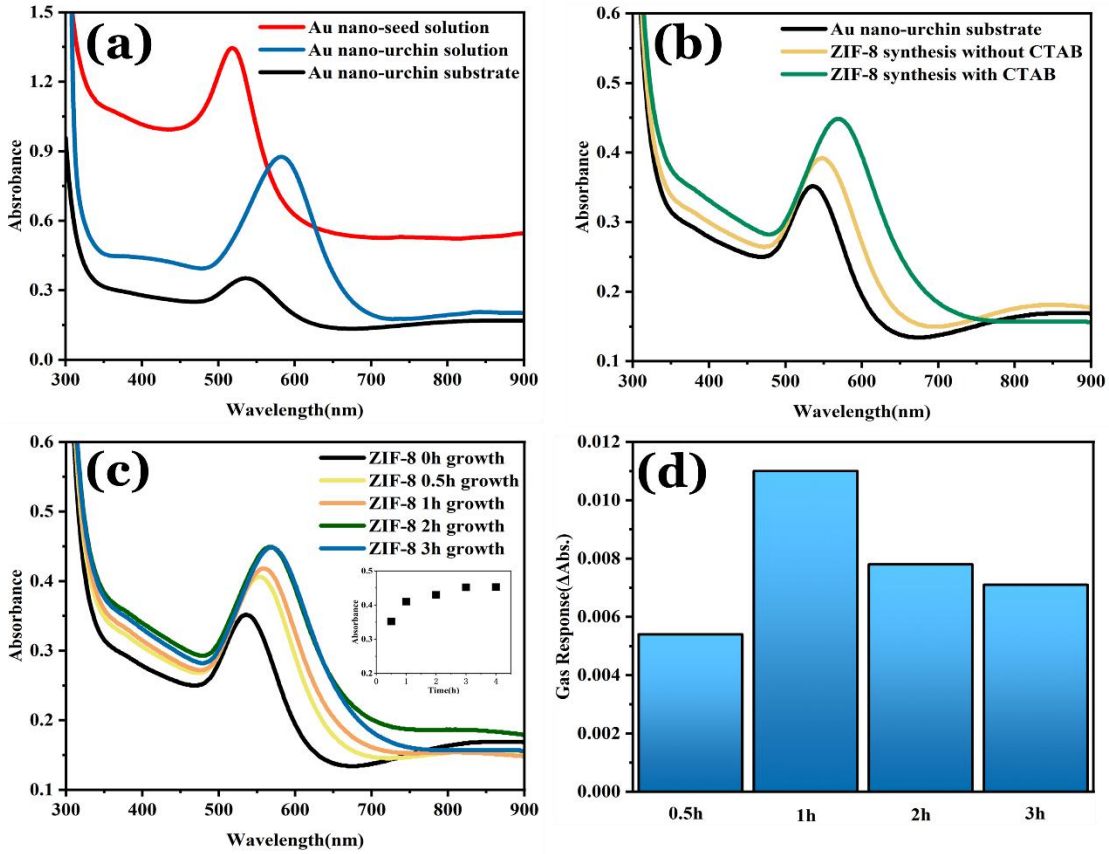

Figure 3.8 (a) Absorption spectra for the fabrication of the Au nano urchin substrate. (b) The effect of CTAB modification on the growth of ZIF-8 nanoparticles. (c) Absorption spectra of ZIF-8 at various growth times. (d) Response of ZIF-8 to ethanol gas across different growth times.

increases. Beyond 2 hours, spectral characteristics remained essentially stable, indicating completion of ZIF-8 growth.

Gas response performance evaluation showed in **Figure 3.8d** demonstrated distinctly different response characteristics to ethanol gas among composite substrates with varying ZIF-8 growth times. The ZIF-8@Au composite substrate with 1-hour growth time exhibited optimal gas response performance, thus establishing this condition as the standard process parameter for subsequent detection experiments.

Table 3.1 Vapor pressure of 5 detected gases around room temperature.

	Acetone	Ethanol	Ethylene Glycol	Hexane	Ammonia
Vapor pressure (around 20.0 °C)	24.6 kPa	5.8 kPa	0.0053 kPa	16.5kPa	861.1 kPa

3.3.3 Gas sensing performance

Gas sensor response performance evaluation employed five typical gases. The vapor pressure of these five gases around room temperature were shown in **Table 3.1**. Gas generation utilized a purging method: 2 mL of test liquid was added to a 10 mL sealed amber glass vial, with pure air introduced at 0.3 L/min to generate gas samples. The experimental process comprised 60-second gas exposure and 120-second air purging, constituting a complete detection cycle.

Assessment of bare gold nano-urchin substrates demonstrated rapid and strong response characteristics to acetone, ethanol, and hexane, relatively weak response to ethylene glycol (low vapor pressure indicated that the concentration of ethylene glycol generated by the gas blowing method was very low, only few ethylene glycol molecule would be presented around the bare gold

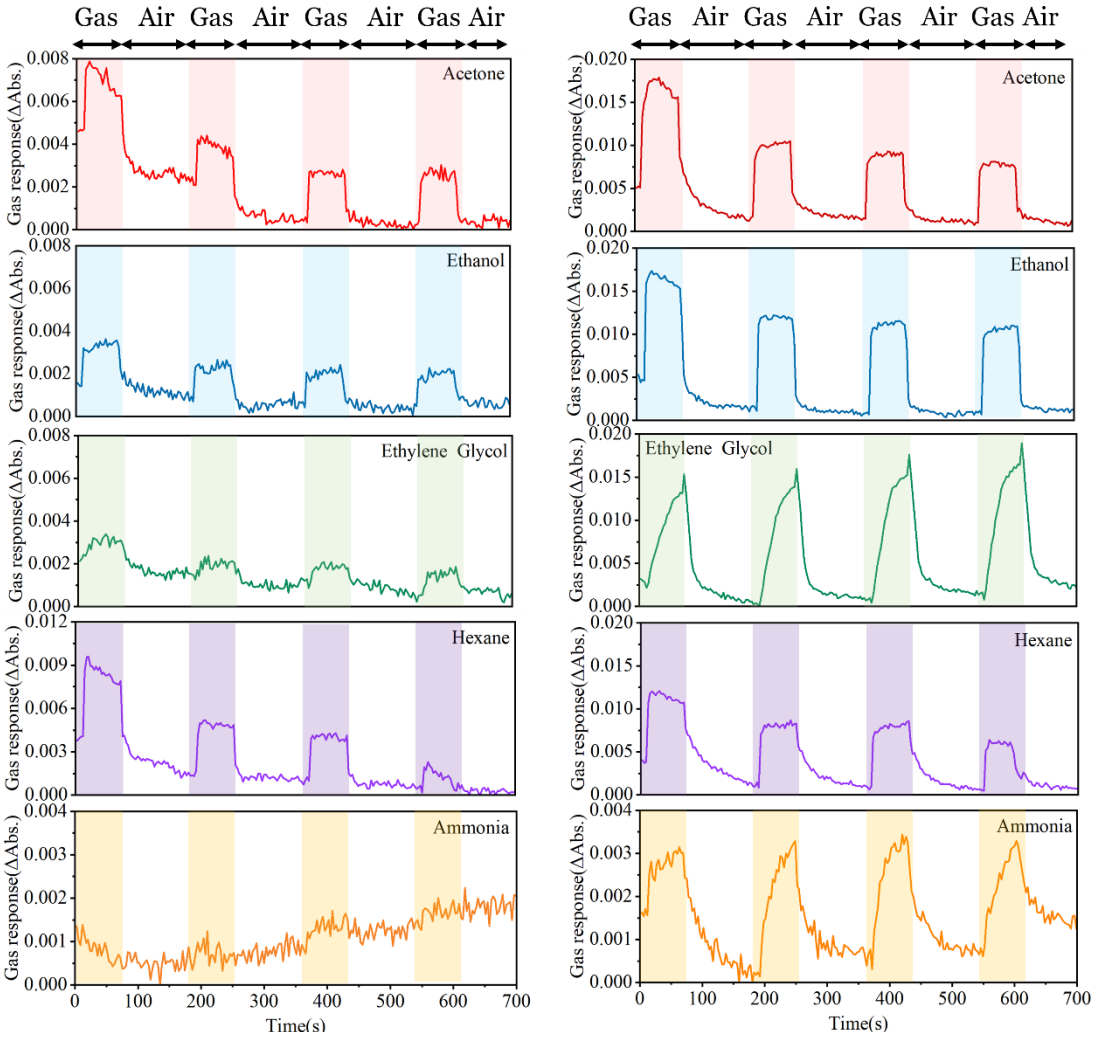

Figure 3.9 (a) Response of Au nano-urchin substrates to five gases. (b) Response of Au nano-urchin substrates with 1h growth of ZIF 8 to five gases.

nanoparticles, so the response was not obvious), while showing only noise-level signals for ammonia (high vapor pressure indicated that ammonia evaporated very quickly, the ammonia molecules dispersed too fast, and the bare gold nanoparticles could not effectively adsorb ammonia molecules, resulting in no response signal.), as shown in **Figure 3.9a**. **Figure 3.9b** showed that after 1-hour ZIF-8 growth on substrate surfaces, sensing performance achieved significant enhancement: response sensitivity to acetone, ethanol, and hexane increased 5-7-fold, ethylene glycol detection signals markedly improved, and effective ammonia detection was achieved. The improvement in the response to ethylene glycol and ammonia were attributed to the ability of the porous structure of ZIF-8 to effectively adsorbed these two gas molecules near the nanoparticles. The selection of these gases was guided by previous studies demonstrating enhanced adsorption through ZIF-8 structures. Enhanced adsorption effects have been extensively reported for acetone [144, 145], ethanol [146, 147], ethylene glycol [148, 149], hexane [150], and ammonia [151, 152]. The ubiquitous presence of these gases in both industrial production and daily life, coupled with my sensor's demonstrated response to all of them, illustrates the broad applicability of the developed gas sensor.

Notably, in **Figure 3.9**, most gases exhibited slight response attenuation following the initial detection cycle. This phenomenon can be attributed to two factors: first, system instability caused by gas flow fluctuations during initial detection; second, slight decrease in sensor sensitivity leading to signal intensity reduction. However, the coefficient of variation for signal intensity in

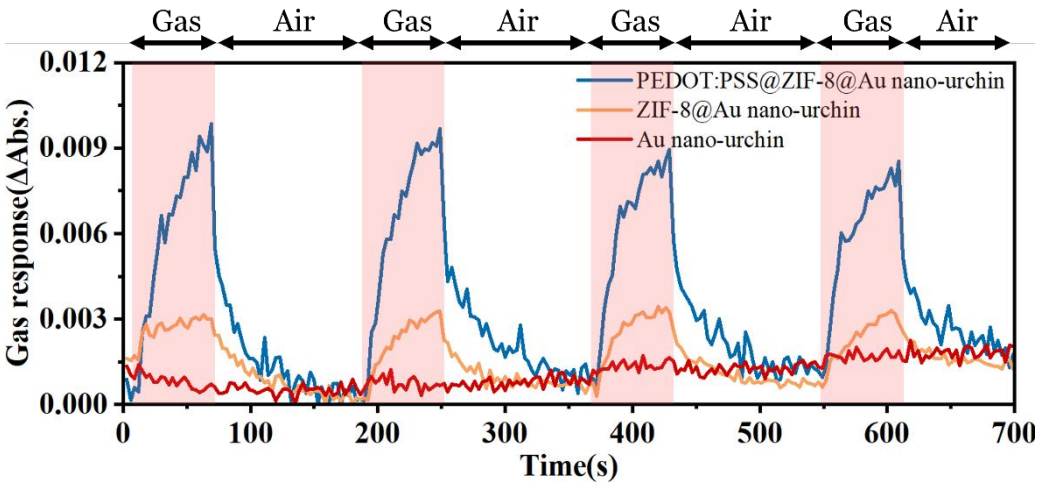

Figure 3.10 Response of different substrates to ammonia sensing.

subsequent detection cycles remained below 10%, indicating that sensors achieved stable operating conditions after initial cycling, meeting requirements for repeated detection.

To further enhance ammonia detection performance, PEDOT: PSS conductive polymer thin layers were spin-coated onto composite substrate surfaces. **Figure 3.10** showed the enhancement effect of PEDOT: PSS conductive polymer. PEDOT: PSS serves as an ideal gas-sensitive material due to its excellent conductivity and ease of fabrication into thin films through various deposition methods like spin-coating, printing, or spray coating. Regarding the enhanced sensitivity of PEDOT: PSS in ammonia detection, researchers have proposed several possible sensing mechanisms. In this study, the enhancement effect can be primarily attributed to two mechanisms: the charge transfer interaction between PEDOT: PSS and ammonia molecules, and the swelling effect induced by the diffusion of ammonia molecules into the PEDOT: PSS polymer [153, 154]. Some past studies have also reported on PEDOT: PSS-coated ZIF-8 nanomaterials. Through synthesis, PEDOT: PSS can be densely and evenly coated on the surface of ZIF-8 [155, 156].

The synergistic effects of this multi-layer functional material system are manifested in: ZIF-8's porous structure providing efficient gas molecule enrichment pathways, PEDOT: PSS layer enabling selective capture of ammonia molecules through specific interactions, Meanwhile, the presence of PEDOT: PSS thin film layer reduced the permeation of other gas molecules,

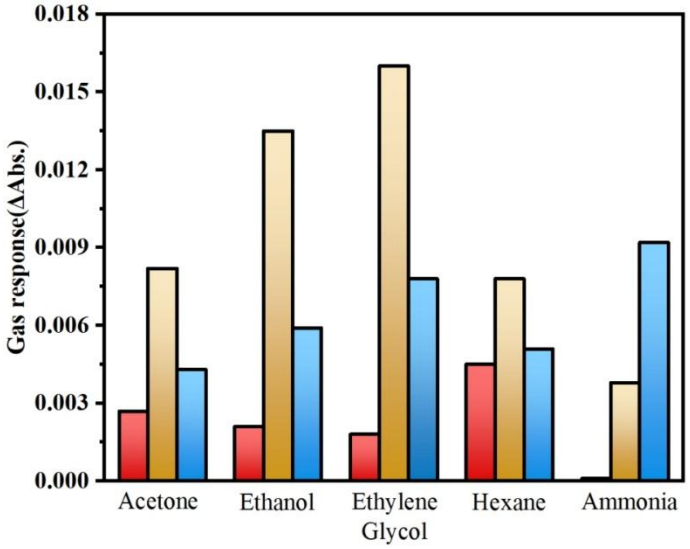

Figure 3.11 Response of the substrate to different gases.

which decreased the number of gas molecules adsorbed by ZIF-8, ultimately leading to a lower response to other gases. As shown in **Figure 3.11**. Gold nano-urchins generating sensitive optical response signals based on LSPR effects. The combination of these mechanisms not only significantly enhances sensor comprehensive performance but also provides innovative insights for developing novel gas sensors.

3.4 Conclusion

In conclusion, this study successfully constructed high-performance composite gas sensing interfaces through sequential modification of PEDOT: PSS conductive polymer layer and ZIF-8 porous framework material on gold nano-urchin substrates. Experimental results confirm that the ZIF-8 encapsulation layer significantly enhanced substrate gas enrichment capability, achieving several-fold improvement in detection sensitivity; while introduction of the PEDOT: PSS functional layer enhanced selective detection of ammonia through specific molecular recognition interactions. This sensing enhancement strategy based on multi-functional material gradient assembly not only demonstrates broad application prospects in gas detection but also provides new insights for designing other types of chemical sensors.

Chapter 4

4. Highly uniform and reproducible silver plasmonic nanosensors fabricated using a three-phase self-assembly method for gas visualization

4.1 Introduction

While my previous chapters 2 and 3 demonstrated two distinct substrates that enhanced plasmonic sensor gas response through in-situ growth strategies, both approaches relied on LSPR detection methodology. Despite offering rapid response times, LSPR detection exhibits inherent limitations in effectively identifying specific gas components. In the realm of plasmonic sensors, SERS has emerged as a powerful complementary technique, widely adopted for molecular identification due to its unique fingerprint characteristics [157]. This led us to develop a novel plasmonic gas sensor specifically optimized for SERS-based gas detection applications.

Traditional interface self-assembly methods primarily consist of liquid-liquid interface (LLI) [158] and liquid-air interface approaches [159]. However, the former typically struggles to produce reliable and reproducible nanoparticle monolayers, while the latter, although capable of generating densely packed nanoparticle assemblies, is limited to hydrophobic nanoparticle fabrication. In this chapter, I employed a three-phase system that synergistically combines the self-healing properties of LLI assembly with the self-driven compression mechanism of the Marangoni effect. This novel approach enabled the fabrication of large-scale, highly reproducible nanoparticle monolayer films regardless of the nanoparticles' hydrophobic or hydrophilic nature. I then transferred this dense monolayer onto a glass substrate to produce a highly uniform and reproducible plasmonic sensor that can be used for SERS detection.

Building upon the development of high-performance sensors, we integrated SERS technology to achieve gas visualization research. The visualization of gas spatial distribution represents a significant extension of

VOC detection technology, which not only enables tracking of odor source locations but also provides crucial data support for intelligent robot positioning algorithms [160-162], while helping to obtain information about the odor source's chemical composition, location, and temporal evolution patterns. Leveraging the advantages of SERS technology, we developed a 3×3 two-dimensional SERS sensor array for gas spatial distribution visualization research. In our experiments, heated benzaldehyde was used as the volatile source, with the sensor array positioned above it for detection. By scanning the sensor array with adsorbed gas molecules using a Raman spectrometer, we collected SERS signals from different locations and generated heat maps through the extraction of characteristic Raman peak intensity information, thereby visually demonstrating the gas spatial distribution characteristics and ultimately achieving precise odor source localization through these distribution patterns.

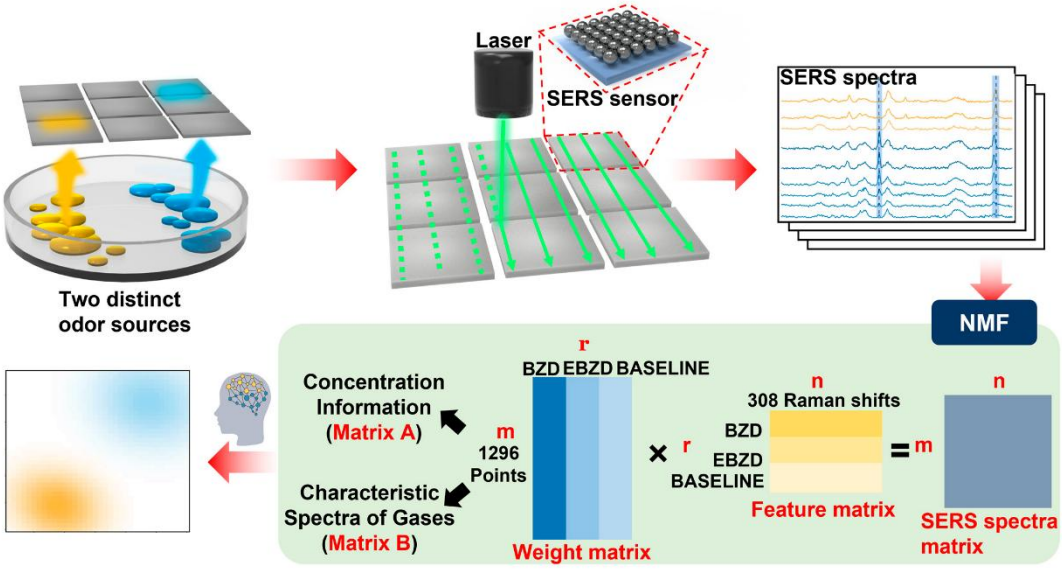

Figure 4.1 Two-dimensional schematic representation of odor detection using a SERS gas sensor array.

4.2 Materials and methods

4.2.1 Instrumentation

UV-visible absorption spectra were recorded on a UV1800 spectrophotometer (Shimadzu, Japan). Gas sensing units were fabricated using an UltimakerS5 3D printer (Ultimaker, Netherlands). Raman spectra were collected using an AvaRaman portable spectrometer (Avantes, Netherlands) equipped with a 532

nm excitation source (1.5 mW). Data analysis was performed using Python 3.6 software package. Morphological characterization was performed using an SU8000 field-emission scanning electron microscope (Hitachi High-Technologies, Japan).

4.2.2 Materials

Trisodium citrate, sodium chloride solution, silver nitrate ($AgNO_3$), ammonia, and ethanol were purchased from Wako Pure Chemical Industries Co., Ltd. (Osaka, Japan). L-ascorbic acid was purchased from Sigma-Aldrich, USA. All reagents were used as received.

4.2.3 Synthesis of Silver Nanoseeds

A mixture of 1 mL sodium citrate solution (1 wt%), 0.25 mL silver nitrate solution (1 wt%), and 0.2 mL sodium chloride solution (20 mM) was added to 1.05 mL deionized water under stirring. After 5 minutes, 80 µL L-ascorbic acid solution was added to 47.5 mL boiling water, followed by the addition of the citrate-silver-chloride mixture after 1 minute. The reaction continued in boiling water bath for 1 hour to obtain silver nanoseed solution.

4.2.4 Synthesis of 90 nm Silver Nanoparticles

Silver-ammonia complex was prepared by mixing 2 mL silver nitrate solution (1 wt%) with 800 µL ammonia solution (25-28 wt%). 550 µL silver nanoseed solution was added to a 50 mL reaction vessel containing 18.92 mL deionized water under stirring. Subsequently, 280 µL silver-ammonia complex solution (43 mM) and 8 mL ascorbic acid solution (2.5 mM) were added sequentially [163]. After 1 hour of stirring, silver nanoparticles were collected by centrifugation and redispersed in 5 mL water. Finally, 100 µL tetrabutyl ammonium nitrate solution was added for surface modification [164].

4.2.5 Fabrication of SERS Sensors

As shown in **Figure 4.2**, Ag NPs monolayer film was formed using an oil/water/oil three-phase system based on the Marangoni effect [163]. 2.5 mL concentrated silver nanoparticle aqueous solution was mixed with 2 mL chloroform in a 15 mL centrifuge tube and manually shaken for 30 seconds. After adding 0.6 µL n-hexane, a dense

monolayer of nanoparticles formed at the water-organic interface. The monolayer was finally transferred onto a glass substrate to obtain the SERS sensor.

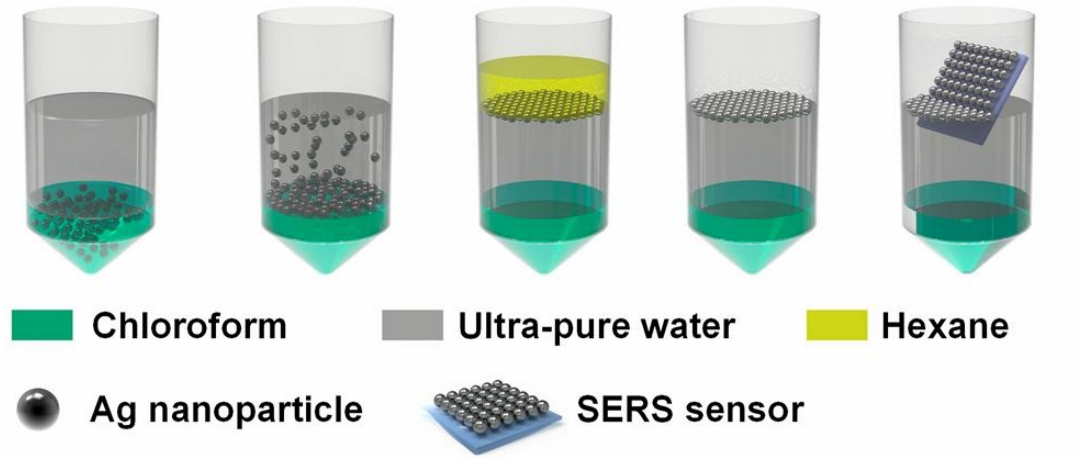

Figure 4.2 Fabrication process of the Surface Enhanced Raman Scattering (SERS) sensors.

4.2.6 Reproducibility of the Fabricated Sensor

To evaluate the reproducibility of SERS sensors, nine independently prepared sensors were immersed in 8 mL of 4-aminothiophenol (4-ATP) ethanol solution (1 μM) and incubated at room temperature (25°C) for 1 hour to achieve molecular modification. The samples were subsequently washed three times with ethanol to remove unbound molecules and dried under high-purity nitrogen flow. The reproducibility of the sensors was assessed through statistical analysis of characteristic Raman peak intensities measured from each sensor surface.

4.2.7 Gas source design and SERS scanning platform

In the odor source preparation, specific volumes of benzaldehyde (BZD) solution were dispensed into aluminum sample wells with both internal diameter and depth of 5 mm. Gas release was accelerated evaporation using a Peltier device with one-minute heating. Five distinct odor source configurations were designed: center point, bottom-left point, top-left/bottom-left dual points, top-right/bottom-left dual points, and center/bottom-left dual points as illustrated in **Figure 4.3**. As shown in **Figure 4.4**, the SERS sensor array was fixed above the odor source within a sealed detection chamber. Following gas

molecule adsorption onto the sensor surface, the sensor array was transferred and secured in the detection chamber, followed by spectral acquisition using a SERS spectra scanning platform showed in **Figure 4.5**. The detection process was automatically controlled, employing a 36×36 point scanning matrix to collect 1,296 SERS spectra, with an interval of 0.4 mm between adjacent sampling points, covering a total scanning area of 14.0 mm×14.0 mm, the acquisition time for each spectral point was set to 1 second.

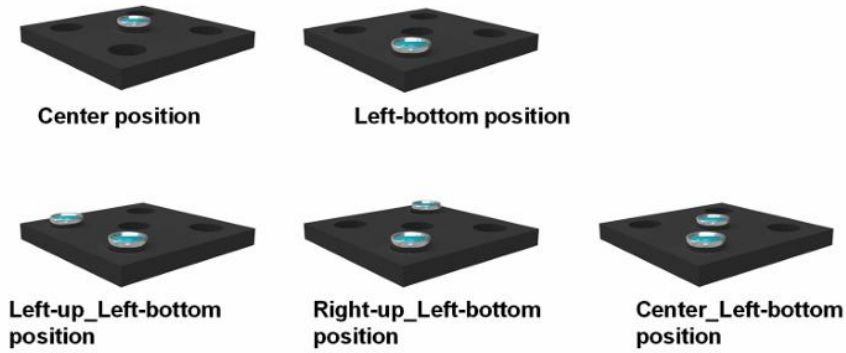

Figure 4.3 Different odor source's location modes.

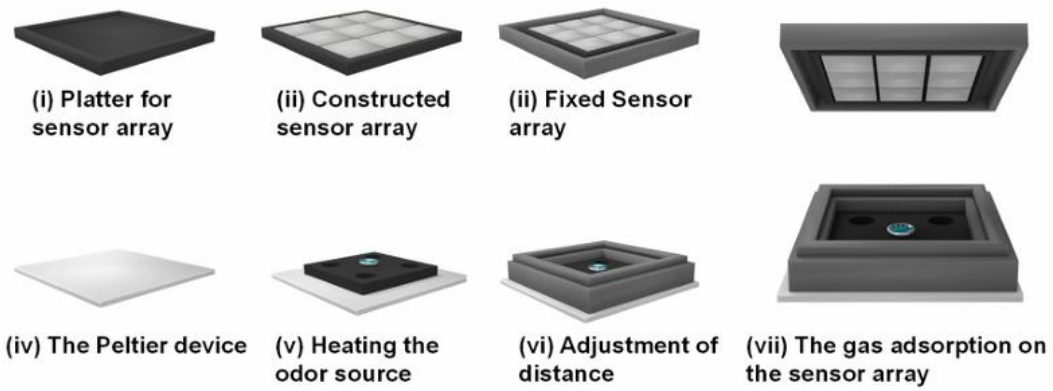

Figure 4.4 Capture process of gas emissions from odor sources by Surface Enhanced Raman Scattering (SERS) Sensor Array.

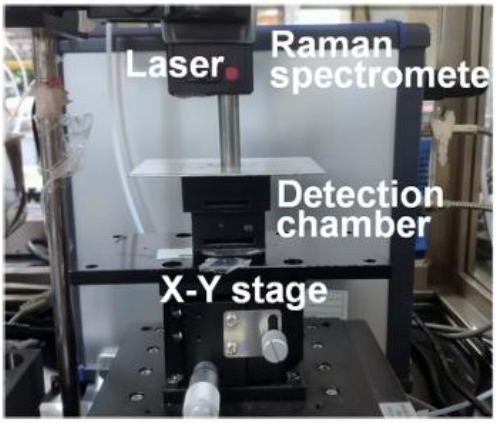

Figure 4.5 SERS spectra scanning platform.

4.3 Results and discussion

4.3.1 Evaluation of SERS sensor

SERS sensors were fabricated by transferring silver nanoparticle (Ag NPs) monolayers onto glass substrates using an oil/water/oil tri-phase interface assembly technique. Large-sized Ag NPs were synthesized via a seed-mediated growth method. As shown in **Figure 4.6**, UV-visible absorption spectroscopy (UV-vis) was employed to characterize the optical properties of both silver seeds and final products. The silver seeds exhibited a characteristic dipole plasmon resonance peak near 400 nm, while the grown Ag NPs showed a red-shifted dipole resonance and a new quadrupole resonance mode appearing at 500 nm.

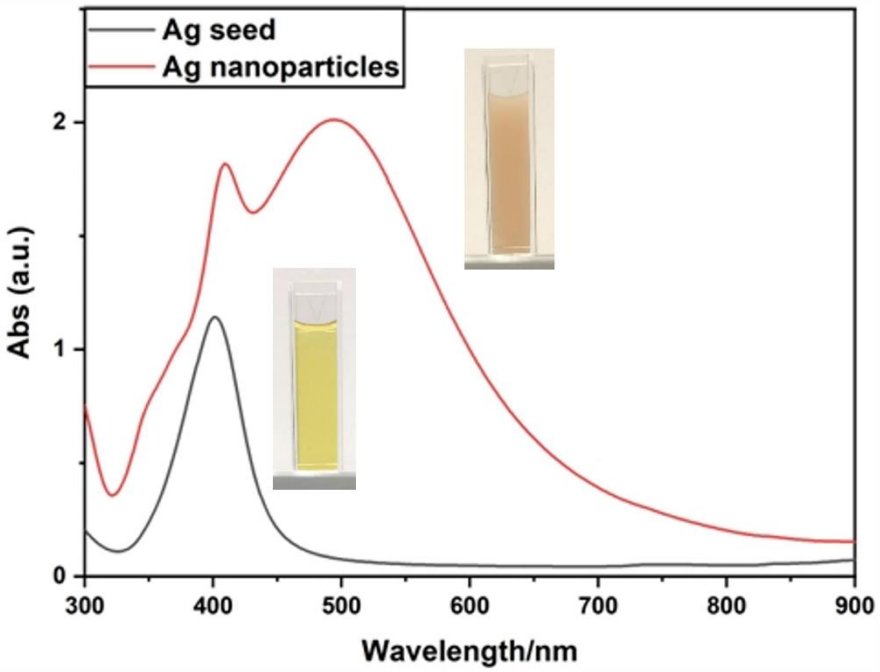

Figure 4.6 UV-vis spectra of the Ag nanoseeds and Ag nanoparticles with average size of 90nm.

Scanning electron microscopy (SEM) images in **Figures 4.7a** and **4.7b** reveal the morphological characteristics of Ag nanoparticles on the SERS sensor surface, confirming the successful transfer of highly dense and regularly arranged nanoparticle monolayers onto the glass substrate. The synthesized Ag NPs demonstrated excellent size uniformity. Statistical analysis of SEM images

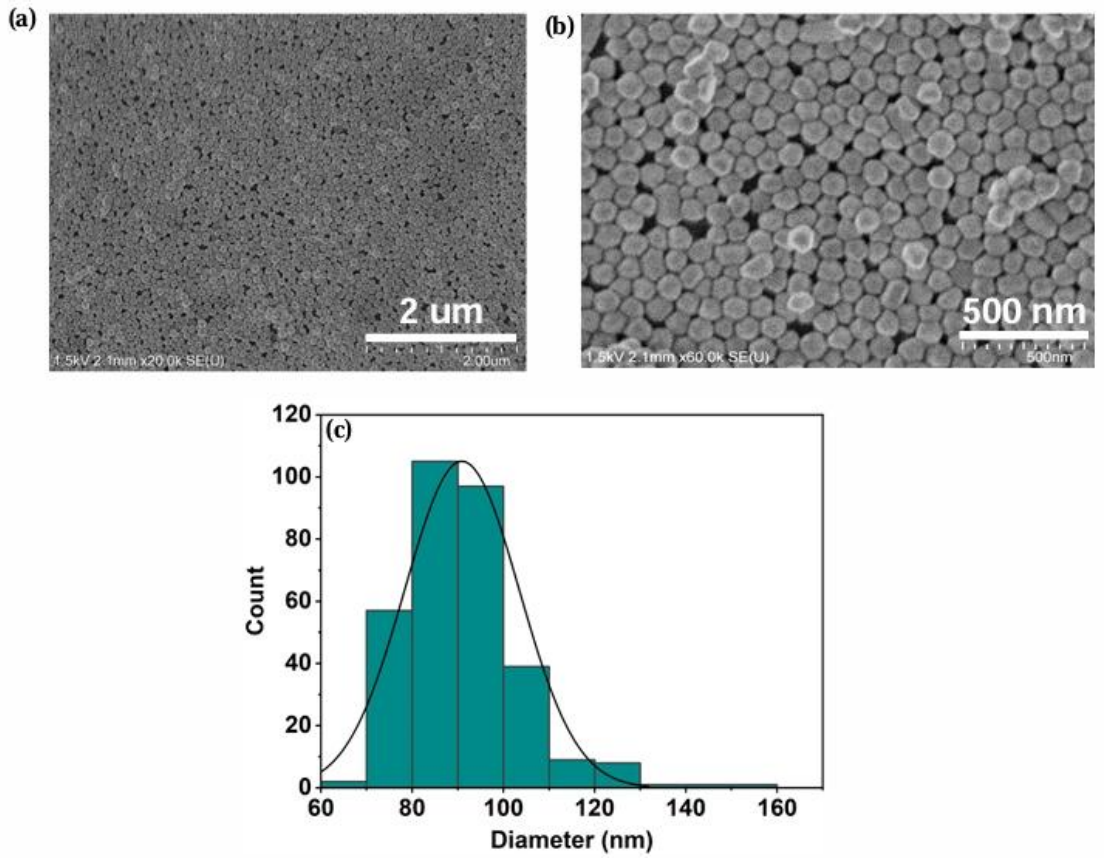

Figure 4.7 (a-b) SEM images of AgNPs distribution onto the substrate; (c) distribution of particle diameter.

using ImageJ software (version 1.53) showed an average particle diameter of 90.90±12.56 nm as shown in **Figure 4.7c**.

To evaluate the uniformity and reproducibility of the prepared SERS sensors, the devices were immersed in 4-aminothiophenol (4-ATP) solution for surface modification, and their SERS spectra were collected in **Figure 4.8a**. One hundred SERS spectra were collected within a 2 mm×2 mm area using a 200 μm step size, **Figure 4.8b** displays the spatial distribution of SERS intensity at the 1082 cm-1 characteristic peak. The relative standard deviation (RSD) of SERS signal intensity was calculated to be 5.45%, demonstrating excellent uniformity over large areas [133,134]. Furthermore, reproducibility assessment was conducted on nine batches of 4-ATP-modified sensors, with **Figure 4.8c** showed the average SERS intensities at 1082 cm^{-1} from 100

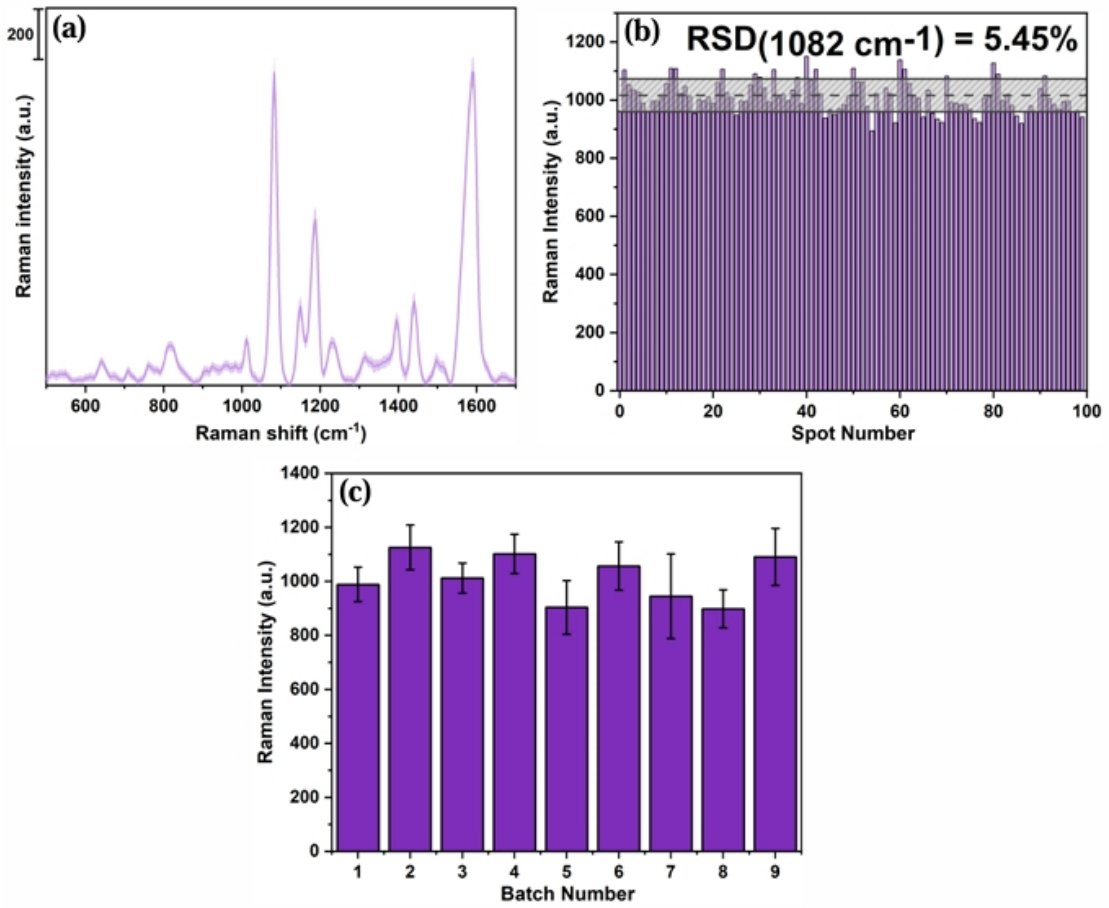

Figure 4.8 (a)Surface-Enhanced Raman Spectrum of 4-ATP molecules on the fabricated SERS sensing substrate; (b) distribution histogram of SERS intensity peaks at 1082 cm^{-1} for 4-ATP across 100 sensor sites; (c) comparative analysis of average SERS intensity at 1082 cm^{-1} from nine different SERS sensors for 4-ATP.

measurement points for each batch. The RSD value of 8.45% across nine batches confirm the excellent batch-to-batch reproducibility of these SERS sensors.

4.3.2 SERS spectra of odor sources

The two-dimensional SERS sensor array was positioned above heated benzaldehyde (BZD) and ethylbenzaldehyde (EBZD) odor sources for around 2 minutes to achieve gas adsorption, followed by transfer to the detection chamber for SERS spectral acquisition. As shown in **Figure 4.9**, sensor baseline spectra and SERS spectra of three gas samples were obtained. BZD exhibits characteristic peaks at 1006 and 1603 cm^{-1} [135], while EBZD shows a single characteristic peak at 1614 cm^{-1}. Notably, the mixture of both gases

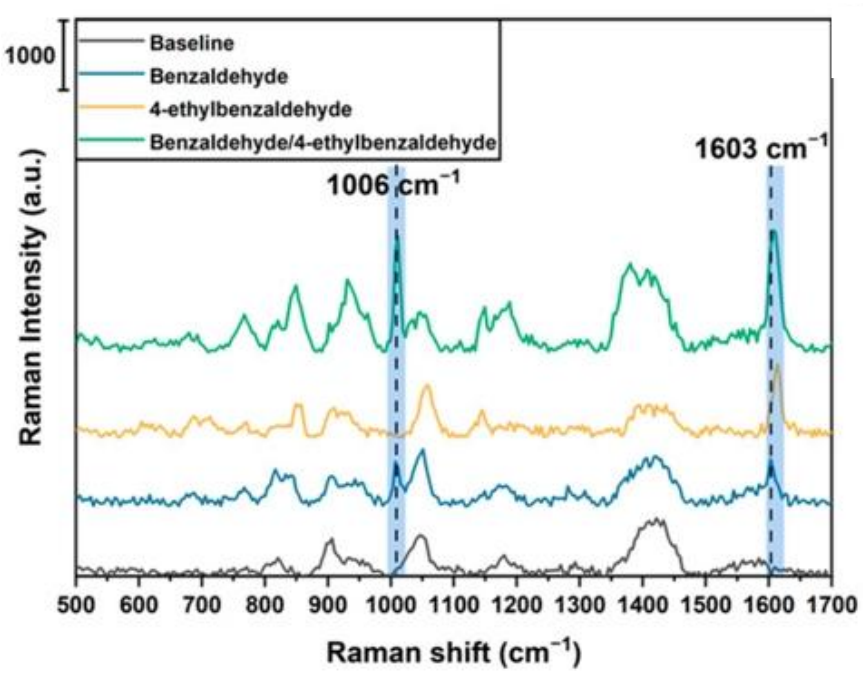

Figure 4.9 SERS spectra of the baseline, BZD, EBZD and their mixture.

displays peaks at 1010 and 1607 cm^{-1}, with the 1010 cm^{-1} peak attributed to BZD. Considering the spectral resolution of approximately 4 cm^{-1} for the Raman spectrometer used in this study, only a single peak (1607 cm^{-1}) could be resolved in the 1603-1614 cm^{-1} range. These distinct spectral features enable differentiation between different gas components.

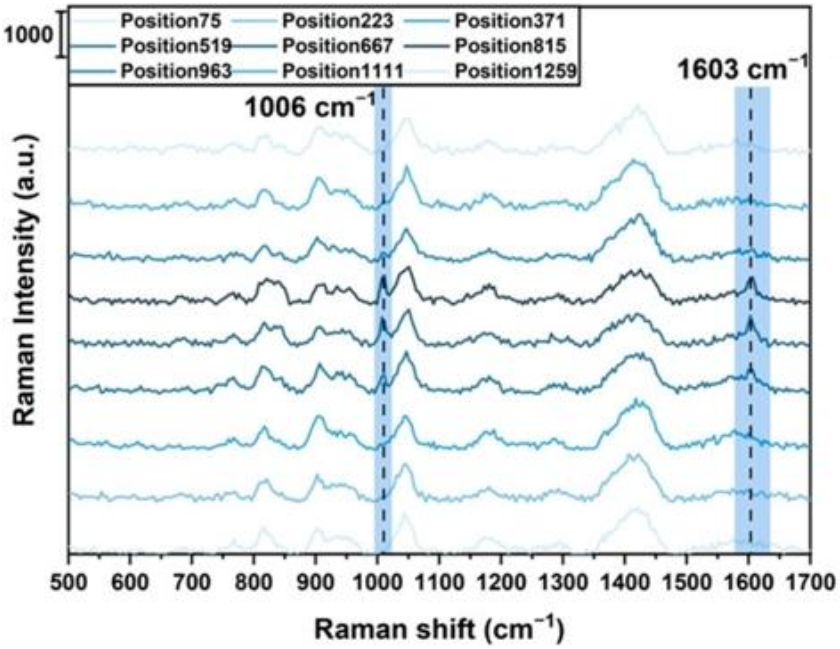

Figure 4.10 SERS spectra collection from diagonal line spots on the sensor array during detection of centrally placed BZD odor source.

4.3.3 Visualization of the odor source

During detection, 1,296 SERS spectra were collected through a 36×36 point matrix scan, proceeding from the upper-left to lower-right corner. With each spectrum acquisition taking 1 second, the total scanning time was 1,296 seconds. As shown in **Figure 4.10**, comparison of spectra collected along the sensor array diagonal reveals variations in SERS signal intensity with position. When the BZD odor source was located at the center position, spectra obtained from the central region showed significantly higher intensity than those from peripheral locations, enabling visualization of the gas spatial distribution.

Each detection yielded 1,296 SERS spectra, with each spectrum containing 308 Raman shift data points, forming a detection result matrix V (1296×308). As shown in **Figure 4.10**, while SERS spectral patterns remain consistent, their intensities vary with gas concentration. Therefore, the matrix V was

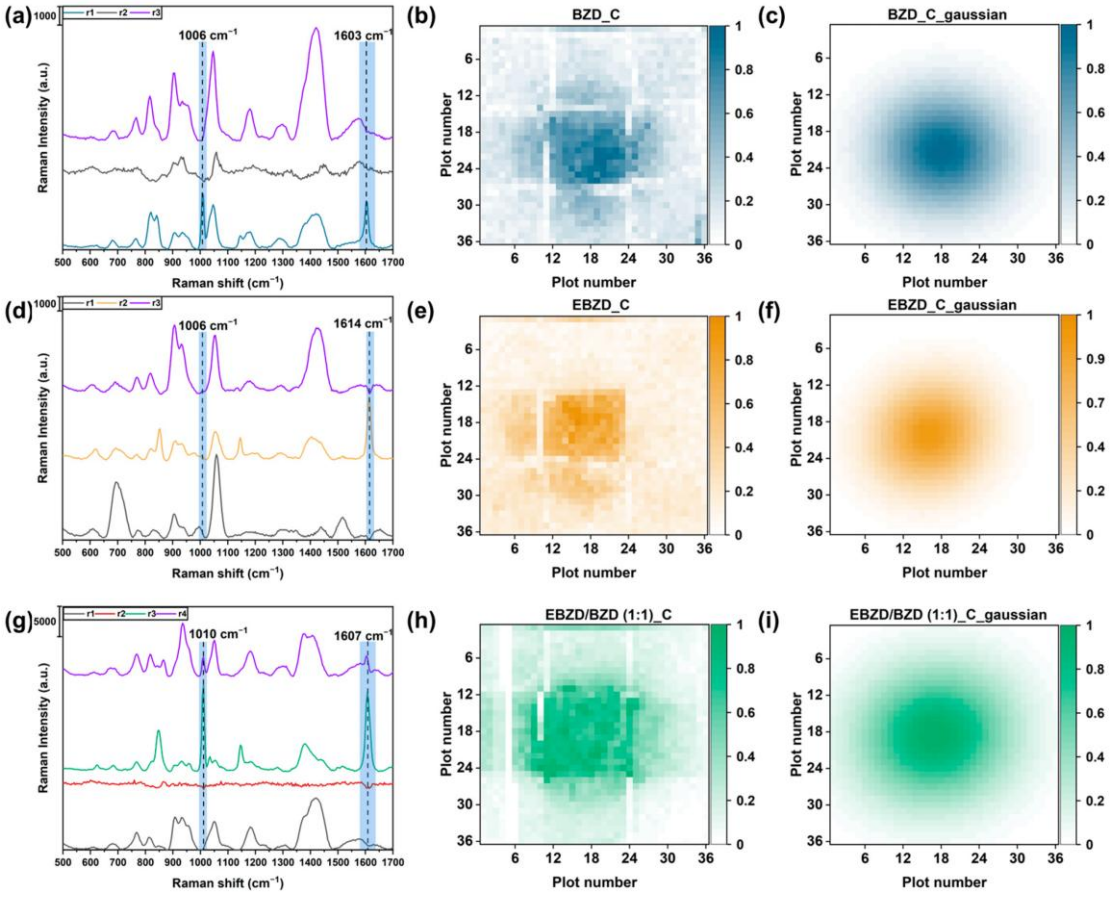

Figure 4.11 Spectral components extracted from feature matrix H through non-negative matrix factorization (NMF) analysis of detection result matrix V (a) BZD, (d) EBZD, and (g) a 1:1 mixture; Heatmap visualization of (b) BZD, (e) EBZD, and (h) mixtures; Gaussian model fitting for odor source visualization of (c) BZD, (f) EBZD, and (i) mixtures.

decomposed into concentration matrix W and feature matrix H using non-negative matrix factorization (NMF) algorithm. For a single odor source, matrix V contains three types of spectra: sensor baseline, target gas signal, and background noise. Spectra collected from small gaps between adjacent sensors in the array were treated as noise signals. Consequently, parameter r in the NMF algorithm was set to 3. In this study, the value of parameter r was determined by adding 2 to the number of gas components.

Initially, the result matrix V (1296×308) for the centrally positioned BZD odor source was decomposed into feature matrix H (3×308) and concentration matrix W (1296×3). As shown in **Figure 4.11a**, component r1 among the three characteristic spectra matches the SERS spectrum of BZD, while the other two components correspond to sensor baseline and noise signals. Raman peaks observed at 900, 1050, and 1400 cm-1 in these two spectra likely originate from chemical reagents remaining on Ag NPs surfaces, as the prepared Ag NPs were not washed prior to transfer onto glass substrates.

The first column of concentration matrix W (representing r1) was normalized and reorganized into a 36×36 matrix to generate a heat map as shown in **Figure 4.11b**. Although individual SERS sensor edges may show non-uniformity, as demonstrated in **Figure 4.8c**, the similar average intensity values from 100 sampling points on each of the nine sensors when detecting 4-ATP at identical concentration indicate good surface uniformity of the sensors. Considering the random nature of BZD gas adsorption on sensor surfaces, Gaussian fitting was applied to process the heat map for enhanced visualization and precise odor source localization. By optimizing the standard deviation parameters of the Gaussian fitting model, a near-circular distribution image was obtained as shown in **Figure 4.11c**, exhibiting high central concentration decreasing radially outward, corresponding to the ideal gas diffusion state from an open cylindrical container.

In addition to BZD, visualization analysis was also performed on single-component EBZD and EBZD/BZD mixture (1:1 volume ratio), as shown in **Figures 4.11f** and **4.11i**. For the mixed gas source, the parameter r in the NMF algorithm was set to 4, considering the presence of two components. Analysis results revealed only one characteristic spectrum corresponding to the EBZD/BZD mixture showed in **Figure 4.11g**, indicating that individual

spectral features of BZD and EBZD could not be resolved in the result matrix V. Different odor sources exhibited distinctly different component characteristics after NMF dimensionality reduction, as shown in **Figures 4.11d** and **4.11g**.

To investigate the relationship between visualization results and actual

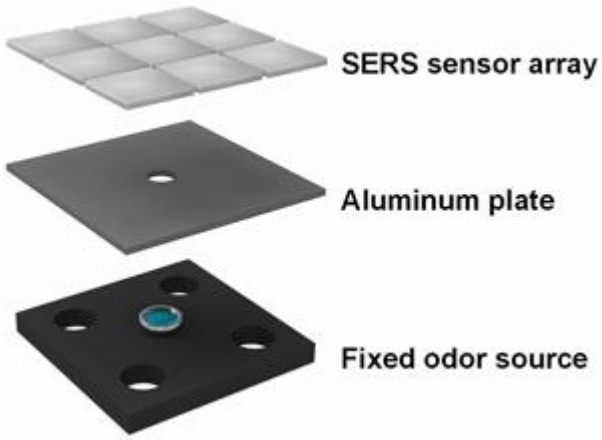

Figure 4.12 Variability in odor source detection based on size modifications

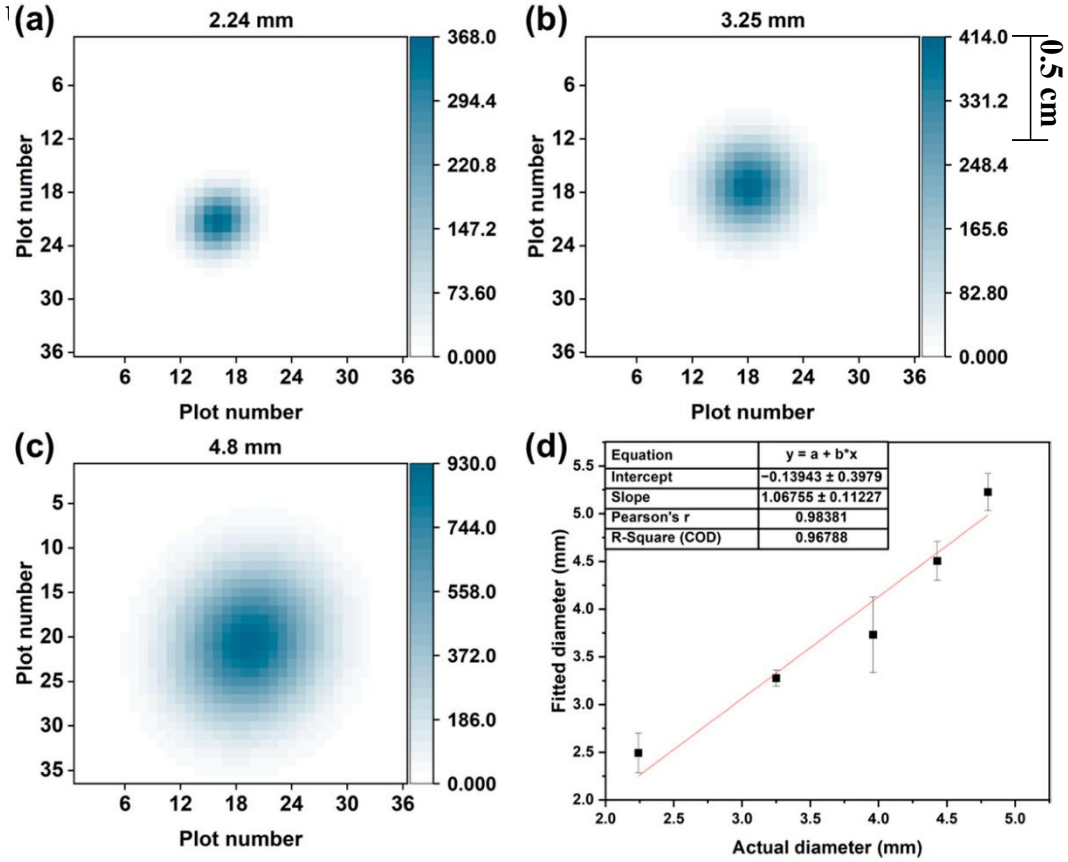

Figure 4.13 Visualization of BZD odor source through varying hole diameters: (a) 2.24 mm; (b) 3.25 mm; (c) 4.8 mm; and (d) linear regression analysis of actual vs. fitted diameters.

odor source dimensions, we controlled the effective release area of BZD by

adjusting the circular aperture diameter (2.24, 3.25, 3.96, 4.43, and 4.8 mm) in the aluminum plate as shown in **Figure 4.12**. **Figures 4.13a-c**, the signal distribution area in the visualization results expanded proportionally with increasing aperture diameter. In the Gaussian fitting model, parameters σ_x and σ_y reflect the spatial distribution characteristics of the gas. Therefore, we used the average of these parameters ($(\sigma_x+\sigma_y)/2$) as an indicator for evaluating the spot size in visualization results. Comparison of calculated fitting diameters with actual aperture diameters as shown in Figure 4.12d, yielded a correlation coefficient R2 of 0.968 through linear regression analysis, demonstrating that fitting diameters can effectively estimate the actual dimensions of odor sources.

I further achieved spatial distribution visualization of dual BZD odor sources. Three source arrangement patterns were designed as shown in **Figure 4.14**: bottom-left/top-left (LB_LU), bottom-left/center (LB_C), and bottom-left/top-right (LB_RU). As shown in **Figure 4.15**, when employing LB_LU and LB_RU patterns, the spatial distribution characteristics of both odor sources exhibited high similarity. Due to the substantial separation between sources in these two patterns, gas diffusion processes showed minimal mutual interference, enabling clear discrimination of individual source locations in the visualization results.

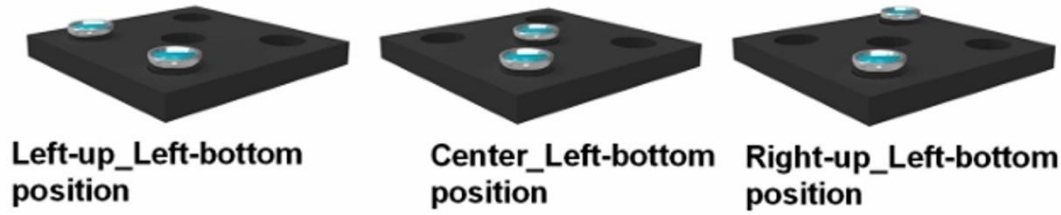

Figure 4.14 Three position patterns of dual BZD odor sources.

Under the LB_C arrangement pattern, the spatial distribution area generated by the centrally positioned source was notably larger than that of the bottom-left position. This difference stems from observations in single-source experiments: the gas diffusion range at the central position consistently exceeds that at corner positions. Moreover, due to the relatively close proximity of the two sources in the LB_C pattern, their spatial distributions showed partial overlap, while still maintaining distinguishable localized distribution characteristics.

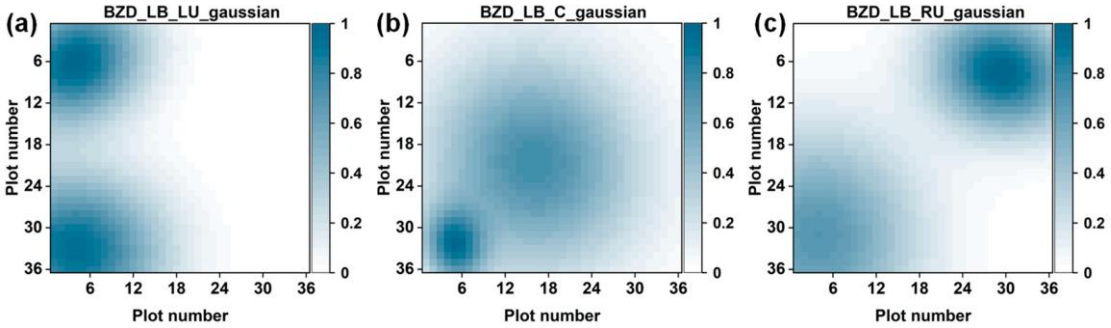

Figure 4.15 Visualization results of two BZD odor sources in three distinct positional patterns: (a) LB_LU; (b) LB_C; and (c) LB_RU.

Spatial distribution visualization of BZD and EBZD odor sources at different positions was achieved using a single SERS sensor array. Gas concentration information was utilized to visualize odor source locations. Spatial distribution images were first obtained separately for both gases, then superimposed according to their respective positions to generate a visualization showing both distributions simultaneously. As shown in **Figure 4.16a**, successful identification and localization of two distinct odor sources was achieved, with the central blue region representing BZD gas distribution and the yellow region indicating EBZD distribution. Due to the close physical proximity of the two sources, an overlapping region was observed where mixed gas spectral features were detected as we observed in **Figure 4.9** before. Additionally, **Figures 4.16b** and **4.16c** demonstrate spatial distribution characteristics when the sources were positioned at alternative locations, showing no distribution interference when source separation was sufficient.

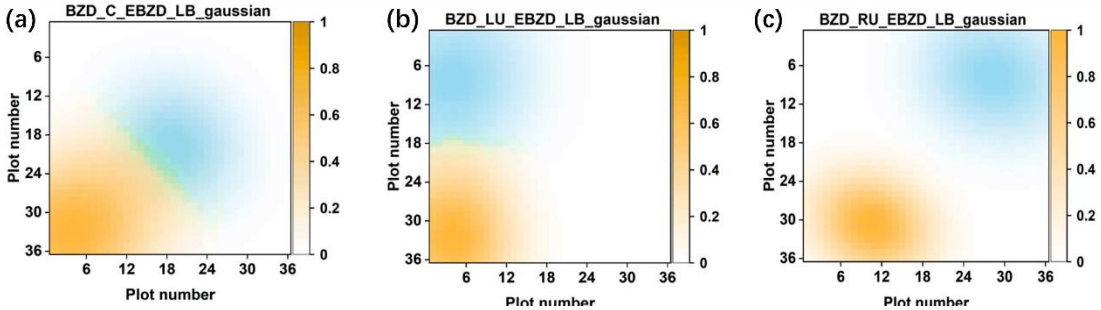

Figure 4.16 Spatial visualization of BZD and EBZD odor sources detected with one SERS sensor array: positioning of EBZD in the LB and BZD at the (a) C; (b) LU; and (c) RU.

4.4 Conclusion

In conclusion, this study established a two-dimensional SERS sensor array for identifying and visualizing the spatial distribution of BZD and EBZD gases. SERS sensors with high reproducibility were fabricated using self-assembly techniques based on the Marangoni effect. Gas adsorption was achieved by positioning the sensor array above odor sources, with SERS spectra collected through scanning to obtain spectral variation information at different locations. The NMF model was employed to decompose detection result matrices, extracting gas concentration and characteristic information, while heat maps visualized gas spatial distribution.

Chapter 5

5. Conclusions and prospects

5.1 Conclusions

Overview

This research systematically developed a series of glass-based plasmonic gas sensors. In terms of material design, we explored various nanostructure combinations to optimize sensing performance, including Au@Ag core-shell nanostructures and metal-organic framework (MOF)-encapsulated Au nanoparticle composite structures. These heterogeneous nanostructures significantly enhanced the response sensitivity of the gas sensors. Regarding assembly processes, we employed in-situ growth and three-phase interface self-assembly methods to achieve precise and controllable preparation of nanomaterials on glass substrate surfaces. These innovative material design strategies and fabrication methods provide new technical approaches for developing high-performance plasmonic gas sensors.

In-situ growth of Au@Ag core-shell nanostructures under photocatalysis

In chapter 2, we successfully fabricated Au@Ag core-shell nanostructures through visible light-induced plasmon-enhanced photochemical reduction. The process involved preparing size-controlled gold nanoseeds on glass substrates via thermal dewetting method, followed by controlled growth of silver shells through catalytic reduction of Ag+ ions in the near-field region, accelerated by the enhanced electromagnetic field generated from visible light excitation of gold nanoparticles. For sensing applications, we innovatively employed a reflection spectroscopy detection mode as an alternative to conventional transmission methods. Through systematic optimization of the reflection probe's incident angle and detection direction, high-quality reflection spectra of the Au@Ag core-shell nanostructures were successfully obtained. A sensing platform was further applied to acetic acid gas detection, demonstrating the feasibility of gas sensing based on reflection detection mode and providing crucial experimental foundation for developing novel portable gas sensors.

MOF shell fabrication to enhance the ability of gas molecular adsorption

In Chapter 3, while we designed Au@Ag core-shell nanostructures in the previous chapter to enhance plasmonic gas sensor sensitivity through metal-metal coupling effects, we also recognized that gas molecule adsorption capability significantly influences sensor performance. Therefore, we developed a high-performance composite gas-sensitive interface by in-situ growth of ZIF-8 porous framework material on gold nano-urchin substrates. Our experimental results confirmed that the ZIF-8 encapsulation layer significantly enhanced the substrate's gas enrichment capability, improving detection sensitivity by several fold. The introduction of the PEDOT: PSS functional layer enhanced selective detection of ammonia through specific molecular recognition interactions. This sensing enhancement strategy based on multi-functional material gradient assembly not only demonstrated broad application prospects in gas detection but also provided new insights for designing other types of chemical sensors.

Highly uniform and reproducible silver plasmonic nanosensors for gas visualization

In Chapter 4, while LSPR detection technology in plasmonic gas sensors enables rapid real-time gas detection, we addressed its limitations in gas identification by introducing SERS detection technology. Taking advantage of SERS's molecular fingerprint characteristics, which provide specific spectral features for different gases, we developed a highly uniform sensing platform. This was achieved through a three-phase self-assembly strategy, where silver nanoparticles were assembled into a monolayer through a Marangoni effect-driven oil/water/oil (O/W/O) interface system. The introduction of $TBA^+NO_3^-$ reduced Coulomb forces between silver nanoparticles, ensuring tight packing in the monolayer. The resulting plasmonic sensors exhibited highly uniform surfaces and excellent reproducibility, successfully demonstrating various gas visualization applications when combined with SERS detection technology.

5.2 Prospects

5.2.1 Dual-mode gas detection platform based on LSPR-SERS combination

LSPR gas detection, based on the plasmon resonance peak shift caused by changes in the refractive index around nanostructures, offers the advantage of rapid response (response time in milliseconds, with detection completed within seconds) [166]. However, LSPR lacks selective recognition of target molecules and typically requires surface modification [92] or combination with specific chemical polymers [95-97] to achieve selectivity, with detection concentration ranges usually around the ppm level. In contrast, while SERS response usually requires longer response time [167] (typical response time of several minutes), it exhibits excellent molecular recognition specificity due to the characteristic Raman fingerprint spectra of gas molecules and can achieve detection sensitivity down to the ppt level [80, 81].

By integrating these two complementary detection techniques onto a single platform, we can achieve a synergistic effect combining rapid response (LSPR) and high molecular specificity (SERS). While LSPR provides real-time, continuous gas concentration monitoring, SERS offers accurate molecular

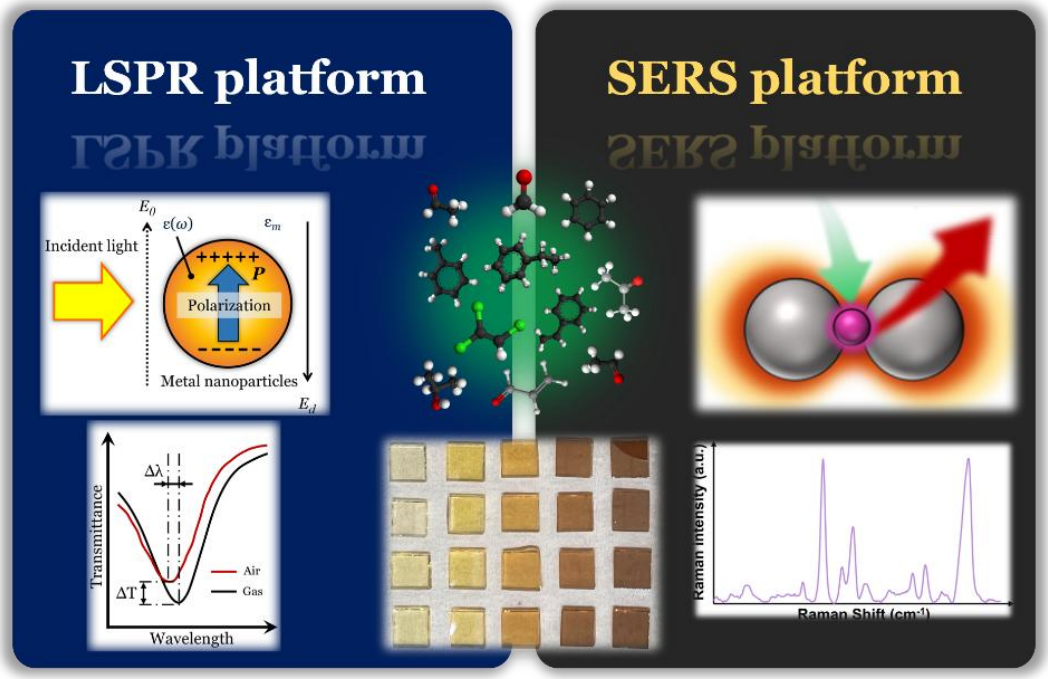

Figure 5.1 Schematic of combination of LSPR and SERS detection platform for VOCs detection.

structural information, significantly enhancing the overall performance of gas detection.

5.2.2 Multi-step dewetting approach to generate gap-enriched Ag nanoislands

Localized Surface Plasmon Resonance (LSPR) and Surface-Enhanced Raman Scattering (SERS) sensing impose different requirements on nanostructure morphology: LSPR demands good nanoparticle dispersion on substrate surfaces to achieve single-particle plasmonic oscillation characteristics [168], while SERS relies on plasmonic hot spot effects between nanoparticles, requiring appropriate interparticle spacing. Therefore, constructing nanostructured substrates with controllable gaps and uniform distribution represents a key scientific challenge for achieving high-performance dual-functional LSPR/SERS detection.

Over the past decade, researchers have developed various high-throughput nanofabrication techniques, including electron beam lithography, nanosphere lithography, and ion etching, for preparing functional substrates with precise nanogaps [116-119]. However, these methods still face challenges in large-area fabrication, cost control, and plasmonic resonance wavelength tuning. While lithography-free solution-phase metal nanoparticle self-assembly offers advantages in large-area preparation and good reproducibility, it requires surface chemical modification of substrates and precise control of factors such as electrostatic forces and fluid dynamics.

Metal film solid-state dewetting, as an alternative strategy, enables preparation of metal nanoisland arrays with significant enhancement effects on large-area substrates, with size and spacing controllable through initial film thickness regulation. However, in single-step dewetting processes, nanoisland dimensions and gaps increase simultaneously with film thickness, limiting its application in high-performance SERS substrate fabrication.

To address this challenge, this research developed a controlled fabrication method for silver nanostructures based on multi-step dewetting as shown in **Figure 5.2**. Compared to single-step dewetting, the multi-step approach not only achieved larger silver nanoislands but also significantly reduced inter-island gap distances [169-171], substantially increasing plasmonic hot spot density. Notably, during multi-step dewetting, inter-island gaps exhibited a continuous decreasing trend with increasing silver nanoisland diameter, contrasting sharply with the proportional changes of size and spacing in traditional single-step dewetting.

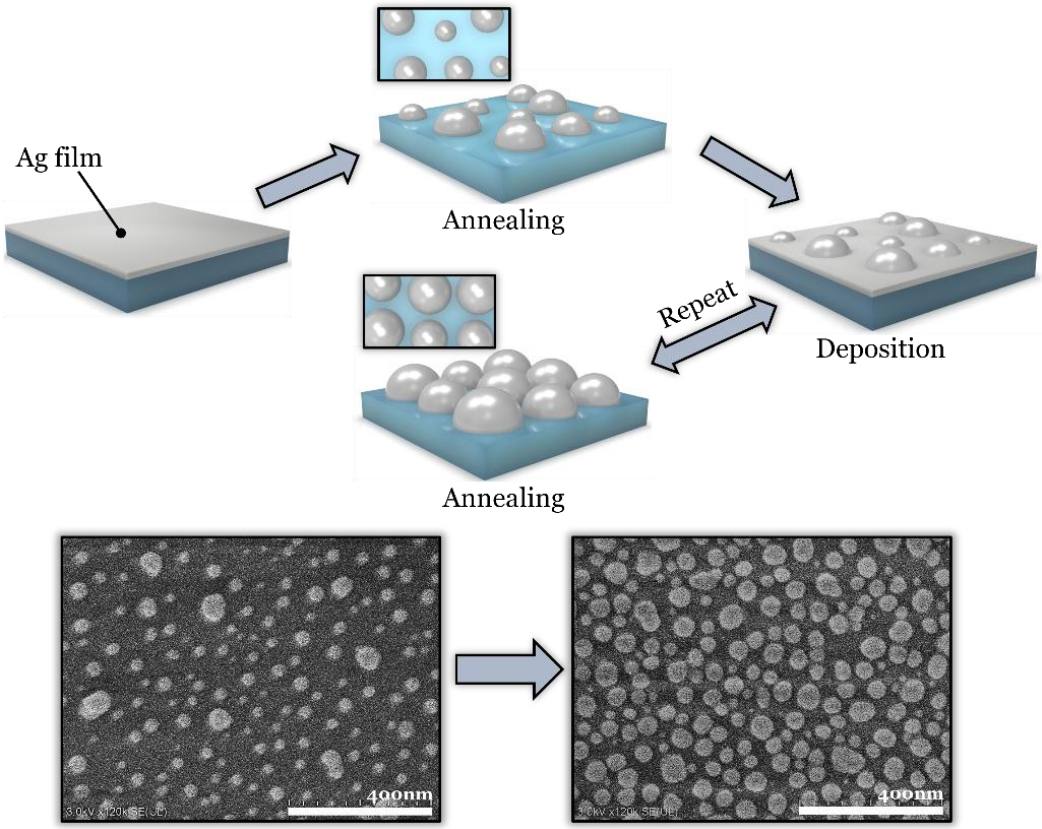

Figure 5.2 Fabrication of Ag nanoisland sensor through multi-step dewetting silver film.

5.2.3 Rapid positioning and identification of gas source

To further promote miniaturization and simplification of LSPR gas detection technology, we propose new technical development strategies.

Reviewing previous LSPR gas detection studies, although spectrophotometers covering a broad spectral range of 300-1200 nm were employed, actual detection primarily relied on monitoring real-time light

intensity changes at specific wavelengths [172]. This characteristic indicates relatively low requirements for light sources and spectral resolution. Drawing from experience in biomolecular LSPR detection, researchers have successfully developed miniaturized detection devices based on single-wavelength LED light sources and photodiode receivers. We plan to introduce this miniaturization design strategy into gas detection and integrate it with SERS probe systems as shown in **Figure 5.3**. This integrated design leverages the complementary advantages of both detection technologies: miniaturized LSPR modules enable real-time gas monitoring and early warning through their rapid response characteristics, while SERS detection provides accurate substance identification through Raman spectral fingerprint information. This LSPR-SERS dual-modal detection strategy shows promise in opening new applications in environmental monitoring, industrial safety, and other fields.

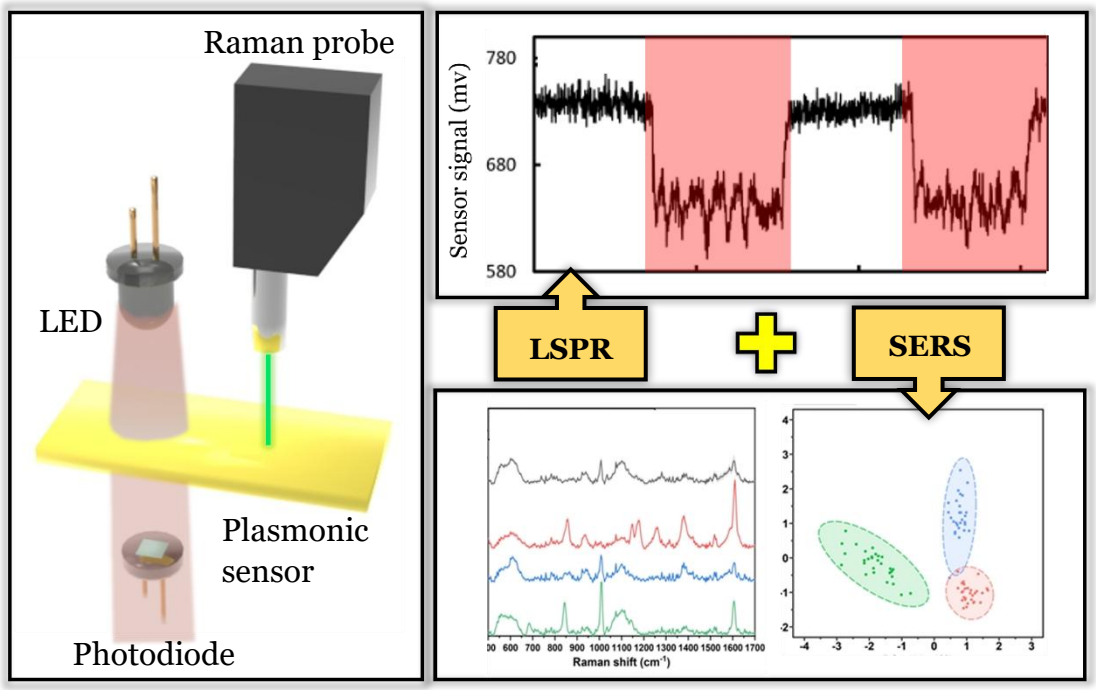

Figure 5.3 Schematic design of LSPR and SERS combination platform.

Reference

[1] Firestein, S. (2001). How the olfactory system makes sense of scents. *Nature*, *413*(6852), 211-218.

[2] Bushdid, C., Magnasco, M. O., Vosshall, L. B., & Keller, A. (2014). Humans can discriminate more than 1 trillion olfactory stimuli. *Science*, *343*(6177), 1370-1372.

[3] Luo, S. X., Axel, R., & Abbott, L. F. (2010). Generating sparse and selective third-order responses in the olfactory system of the fly. *Proceedings of the National Academy of Sciences*, *107*(23), 10713-10718.

[4] Turner, A. P., & Magan, N. (2004). Electronic noses and disease diagnostics. *Nature Reviews Microbiology*, *2*(2), 161-166.

[5] Bartlett, G. (1994). A brief history of electronic noses. *Sens. Actuators B Chem*, *18*, 211-220.

[6] Chiu, H. H., & Kuo, C. H. (2020). Gas chromatography-mass spectrometry-based analytical strategies for fatty acid analysis in biological samples. *Journal of food and drug analysis*, *28*(1), 60-73.

[7] Woollam, M., Teli, M., Angarita-Rivera, P., Liu, S., Siegel, A. P., Yokota, H., & Agarwal, M. (2019). Detection of volatile organic compounds (VOCs) in urine via gas chromatography-mass spectrometry QTOF to differentiate between localized and metastatic models of breast cancer. *Scientific reports*, *9*(1), 2526.

[8] Kim, Y. Y., Kim, M. K., & Shin, H. S. (2022). Determination of volatile organic compounds (VOCs) levels from various smoking cessation aids by using gas chromatography-mass spectrometry methodology. *Journal of Toxicology and Environmental Health, Part A*, *85*(3), 110-120.

[9] Hyodo, T., & Shimizu, Y. (2020). Adsorption/combustion-type micro gas sensors: Typical VOC-sensing properties and material-design approach for highly sensitive and selective VOC detection. *Analytical Sciences*, *36*(4), 401-411.

[10] Yang, L., Li, Y., Sun, Y., Wang, W., & Shao, Z. (2022). Perovskite oxides in catalytic combustion of volatile organic compounds: Recent advances and future prospects. *Energy & Environmental Materials*, *5*(3), 751-776.

[11] Kumar, P., Kim, K. H., Mehta, P. K., Ge, L., & Lisak, G. (2019). Progress and challenges in electrochemical sensing of volatile organic compounds using metal-organic frameworks. *Critical reviews in environmental science and Technology*, *49*(21), 2016-2048.

[12] Ramaiyan, K. P., & Mukundan, R. (2019). Electrochemical sensors for air quality monitoring. *The Electrochemical Society Interface*, *28*(3), 59.

[13] Zhong, X., Li, D., Du, W., Yan, M., Wang, Y., Huo, D., & Hou, C. (2018). Rapid recognition of volatile organic compounds with colorimetric sensor arrays for lung cancer screening. *Analytical and bioanalytical chemistry*, *410*, 3671-3681.

[14] He, C., Liu, L., Korposh, S., Correia, R., & Morgan, S. P. (2021). Volatile organic compound vapour measurements using a localised surface plasmon resonance optical fibre sensor decorated with a metal-organic framework. *Sensors*, *21*(4), 1420.

[15] Jamila, R. M., Narasimman, S., Prasanth, A., Muthukumar, M., Alex, Z. C., & Anand,

G. T. (2024). Fiber optic sensor coated with multiple layers of hexagonal boron nitride nanosheets (BNNS) for the detection of volatile organic compounds. *ACS Applied Materials & Interfaces*, *16*(27), 35525-35540.

[16] Hromadka, J., Tokay, B., Correia, R., Morgan, S. P., & Korposh, S. (2018). Highly sensitive volatile organic compounds vapour measurements using a long period grating optical fibre sensor coated with metal organic framework ZIF-8. *Sensors and actuators B: chemical*, *260*, 685-692.

[17] Knebl, A., Domes, C., Domes, R., Wolf, S., Popp, J., & Frosch, T. (2021). Hydrogen and C2–C6 alkane sensing in complex fuel gas mixtures with fiber-enhanced Raman spectroscopy. *Analytical chemistry*, *93*(30), 10546-10552.

[18] Tropp, J., Ihde, M. H., Williams, A. K., White, N. J., Eedugurala, N., Bell, N. C., ... & Bonizzoni, M. (2019). A sensor array for the discrimination of polycyclic aromatic hydrocarbons using conjugated polymers and the inner filter effect. *Chemical Science*, *10*(44), 10247-10255.

[19] Ahmed, K., Haque, M. J., Jabin, M. A., Paul, B. K., Amiri, I. S., & Yupapin, P. (2019). Tetra-core surface plasmon resonance based biosensor for alcohol sensing. *Physica B: Condensed Matter*, *570*, 48-52.

[20] Tang, X., Haddad, P. A., Mager, N., Geng, X., Reckinger, N., Hermans, S., ... & Raskin, J. P. (2019). Chemically deposited palladium nanoparticles on graphene for hydrogen sensor applications. *Scientific reports*, *9*(1), 3653.

[21] Kumar, V., Majhi, S. M., Kim, K. H., Kim, H. W., & Kwon, E. E. (2021). Advances in In2O3-based materials for the development of hydrogen sulfide sensors. *Chemical Engineering Journal*, *404*, 126472.

[22] Yao, C., Wang, Q., Lin, Y., Jin, W., Xiao, L., Gao, S., ... & Ren, W. (2019). Photothermal CO detection in a hollow-core negative curvature fiber. *Optics letters*, *44*(16), 4048-4051.

[23] Miller, K., Reichert, C. L., & Schmid, M. (2023). Biogenic amine detection systems for intelligent packaging concepts: Meat and Meat Products. *Food Reviews International*, *39*(5), 2543-2567.

[24] Andre, R. S., Ngo, Q. P., Fugikawa-Santos, L., Correa, D. S., & Swager, T. M. (2021). Wireless tags with hybrid nanomaterials for volatile amine detection. *ACS sensors*, *6*(6), 2457-2464.

[25] Sun, L., Rotaru, A., & Garcia, Y. (2022). A non-porous Fe (II) complex for the colorimetric detection of hazardous gases and the monitoring of meat freshness. *Journal of Hazardous Materials*, *437*, 129364.

[26] Sun, M., Yang, X., Zhang, Y., Wang, S., Wong, M. W., Ni, R., & Huang, D. (2018). Rapid and visual detection and quantitation of ethylene released from ripening fruits: the new use of Grubbs catalyst. *Journal of agricultural and food chemistry*, *67*(1), 507-513.

[27] Vong, K., Eda, S., Kadota, Y., Nasibullin, I., Wakatake, T., Yokoshima, S., ... & Tanaka, K. (2019). An artificial metalloenzyme biosensor can detect ethylene gas in fruits and Arabidopsis leaves. *Nature communications*, *10*(1), 5746.

[28] Nguyen, L. H., Oveissi, F., Chandrawati, R., Dehghani, F., & Naficy, S. (2020).

Naked-eye detection of ethylene using thiol-functionalized polydiacetylene-based flexible sensors. *ACS sensors*, *5*(7), 1921-1928.

[29] Giunti, G., Palmeri, V., Algeri, G. M., & Campolo, O. (2018). VOC emissions influence intra-and interspecific interactions among stored-product Coleoptera in paddy rice. *Scientific reports*, *8*(1), 2052.

[30] MacDougall, S., Bayansal, F., & Ahmadi, A. (2022). Emerging methods of monitoring volatile organic compounds for detection of plant pests and disease. *Biosensors*, *12*(4), 239.

[31] Le, T., & Priefer, R. (2023). Detection technologies of volatile organic compounds in the breath for cancer diagnoses. *Talanta*, *265*, 124767.

[32] Rudnicka, J., Kowalkowski, T., & Buszewski, B. (2019). Searching for selected VOCs in human breath samples as potential markers of lung cancer. *Lung Cancer*, *135*, 123-129.

[33] Chang, S. H., Ho, H. Y., Chang, C. C., Zang, C. Z., Hsu, Y. H., Lin, M. C., ... & Wang, D. Y. (2022). Evaluation and optimization of a HS-SPME-assisted GC-MS/MS method for monitoring nitrosamine impurities in diverse pharmaceuticals. *Journal of Pharmaceutical and Biomedical Analysis*, *221*, 115003.

[34] Žnideršič, L., Mlakar, A., & Prosen, H. (2019). Development of a SPME-GC-MS/MS method for the determination of some contaminants from food contact material in beverages. *Food and Chemical Toxicology*, *134*, 110829.

[35] Chen, S., Rui, R., Wang, S., & He, X. (2022). Comparative analysis of the floral fragrance compounds of Panax notoginseng flowers under the Panax notoginseng-pinus agroforestry system using SPME-GC-MS. *Molecules*, *27*(11), 3565.

[36] Godage, N. H., & Gionfriddo, E. (2022). Biocompatible SPME coupled to GC/MS for analysis of xenobiotics in blood plasma. *Journal of Chromatography B*, *1203*, 123308.

[37] Degler, D., Weimar, U., & Barsan, N. (2019). Current understanding of the fundamental mechanisms of doped and loaded semiconducting metal-oxide-based gas sensing materials. *ACS sensors*, *4*(9), 2228-2249.

[38] Cao, P., Yang, Z., Navale, S. T., Han, S., Liu, X., Liu, W., ... & Zhu, D. (2019). Ethanol sensing behavior of Pd-nanoparticles decorated ZnO-nanorod based chemiresistive gas sensors. *Sensors and Actuators B: Chemical*, *298*, 126850.

[39] Park, J. A., Moon, J., Lee, S. J., Kim, S. H., Zyung, T., & Chu, H. Y. (2010). Structure and CO gas sensing properties of electrospun TiO2 nanofibers. *Materials Letters*, *64*(3), 255-257.

[40] Li, X., Wang, Y., Lei, Y., & Gu, Z. (2012). Highly sensitive H 2 S sensor based on template-synthesized CuO nanowires. *Rsc Advances*, *2*(6), 2302-2307.

[41] Eslamian, M. (2017). Inorganic and organic solution-processed thin film devices. *Nano-micro letters*, *9*(1), 3.

[42] Singh, P., Kushwaha, C. S., Singh, V. K., Dubey, G. C., & Shukla, S. K. (2021). Chemiresistive sensing of volatile ammonia over zinc oxide encapsulated polypyrrole based nanocomposite. *Sensors and Actuators B: Chemical*, *342*, 130042.

[43] Kwon, C. H., Ko, Y., Shin, D., Lee, S. W., & Cho, J. (2019). Highly conductive electrocatalytic gold nanoparticle-assembled carbon fiber electrode for high-performance glucose-based biofuel cells. *Journal of Materials Chemistry A*, *7*(22), 13495-13505.

[44] Koudehi, M. F., & Pourmortazavi, S. M. (2018). Polyvinyl alcohol/polypyrrole/molecularly imprinted polymer nanocomposite as highly selective chemiresistor sensor for 2, 4 - DNT vapor recognition. *Electroanalysis*, *30*(10), 2302-2310.

[45] Zhang, W., Wu, Z., Hu, J., Cao, Y., Guo, J., Long, M., ... & Jia, D. (2020). Flexible chemiresistive sensor of polyaniline coated filter paper prepared by spraying for fast and non-contact detection of nitroaromatic explosives. *Sensors and Actuators B: Chemical*, *304*, 127233.

[46] Hekiem, N. L. L., Ralib, A. A. M., Hatta, M. A. M., Ahmad, F. B., Ab Rahim, R., & Za'bah, N. F. (2021, August). Performance analysis of VOCs detection using polyisobutylene and chitosan overlayed on QCM sensor. In *2021 IEEE regional symposium on micro and nanoelectronics (RSM)* (pp. 157-160). IEEE.

[47] Nuhoglu, D., Tasaltin, C., & Gurol, I. (2024). QCM and SAW gas and VOC sensors based on metal oxide composites (principles, fabrication, sensing materials, and performances). In *Complex and Composite Metal Oxides for Gas VOC and Humidity Sensors Volume 1* (pp. 223-252). Elsevier.

[48] Ayad, M. M., Abdelghafar, M. E., Torad, N. L., Yamauchi, Y., & Amer, W. A. (2023). Green synthesis of carbon quantum dots toward highly sensitive detection of formaldehyde vapors using QCM sensor. *Chemosphere*, *312*, 137031.

[49] Völkle, J., Kumpf, K., Feldner, A., Lieberzeit, P., & Fruhmann, P. (2022). Development of conductive molecularly imprinted polymers (cMIPs) for limonene to improve and interconnect QCM and chemiresistor sensing. *Sensors and Actuators B: Chemical*, *356*, 131293.

[50] Sun, L., Rotaru, A., Robeyns, K., & Garcia, Y. (2021). A colorimetric sensor for the highly selective, ultra-sensitive, and rapid detection of volatile organic compounds and hazardous gases. *Industrial & Engineering Chemistry Research*, *60*(24), 8788-8798.

[51] Jin, K., Moon, D., Chen, Y. P., & Park, J. (2024). Comprehensive Qualitative and Quantitative Colorimetric Sensing of Volatile Organic Compounds Using Monolayered Metal–Organic Framework Films. *Advanced Materials*, *36*(8), 2309570.

[52] Hussain, S., Majumder, S., De, U. C., Bhattacharjee, D., Hussain, S., & Hussain, S. A. (2024). Colorimetric sensor for detecting volatile organic compounds. *Interactions*, *245*(1), 303.

[53] Park, D. H., Heo, J. M., Jeong, W., Yoo, Y. H., Park, B. J., & Kim, J. M. (2018). Smartphone-based VOC sensor using colorimetric polydiacetylenes. *ACS applied materials & interfaces*, *10*(5), 5014-5021.

[54] Zheng, Z., & Zhang, C. (2022). Electronic noses based on metal oxide semiconductor sensors for detecting crop diseases and insect pests. *Computers and Electronics in*

Agriculture, *197*, 106988.

[55] Leggieri, M. C., Mazzoni, M., Fodil, S., Moschini, M., Bertuzzi, T., Prandini, A., & Battilani, P. (2021). An electronic nose supported by an artificial neural network for the rapid detection of aflatoxin B1 and fumonisins in maize. *Food Control*, *123*, 107722.

[56] Cui, S., Inocente, E. A. A., Acosta, N., Keener, H. M., Zhu, H., & Ling, P. P. (2019). Development of fast e-nose system for early-stage diagnosis of aphid-stressed tomato plants. *Sensors*, *19*(16), 3480.

[57] Fuentes, S., Tongson, E., Unnithan, R. R., & Gonzalez Viejo, C. (2021). Early detection of aphid infestation and insect-plant interaction assessment in wheat using a low-cost electronic nose (E-nose), near-infrared spectroscopy and machine learning modeling. *Sensors*, *21*(17), 5948.

[58] Nurputra, D. K., Kusumaatmaja, A., Hakim, M. S., Hidayat, S. N., Julian, T., Sumanto, B., ... & Triyana, K. (2022). Fast and noninvasive electronic nose for sniffing out COVID-19 based on exhaled breath-print recognition. *NPJ Digital Medicine*, *5*(1), 115.

[59] Behera, B., Joshi, R., Vishnu, G. A., Bhalerao, S., & Pandya, H. J. (2019). Electronic nose: A non-invasive technology for breath analysis of diabetes and lung cancer patients. *Journal of breath research*, *13*(2), 024001.

[60] Binson, V. A., & Subramoniam, M. (2021). Design and development of an e-nose system for the diagnosis of pulmonary diseases. *Acta of Bioengineering and Biomechanics*, *23*(1).

[61] [60] A., Vieira, V. D., ... & Garcia-Ramirez, A. R. (2018). Development of an electronic nose to characterize odours emitted from different stages in a wastewater treatment plant. *Water research*, *134*, 92-100.

[62] Bieganowski, A., Józefaciuk, G., Bandura, L., Guz, Ł., Łagód, G., & Franus, W. (2018). Evaluation of hydrocarbon soil pollution using e-nose. *Sensors*, *18*(8), 2463.

[63] Ari, D., & Alagoz, B. B. (2022). An effective integrated genetic programming and neural network model for electronic nose calibration of air pollution monitoring application. *Neural Computing and Applications*, *34*(15), 12633-12652.

[64] Kumar, K., Chaudhri, S. N., Rajput, N. S., Shvetsov, A. V., Sahal, R., & Alsamhi, S. H. (2023). An IoT-enabled E-Nose for remote detection and monitoring of airborne pollution hazards using LoRa network protocol. *Sensors*, *23*(10), 4885.

[65] Grassi, S., Benedetti, S., Opizzio, M., di Nardo, E., & Buratti, S. (2019). Meat and fish freshness assessment by a portable and simplified electronic nose system (Mastersense). *Sensors*, *19*(14), 3225.

[66] Chen, J., Gu, J., Zhang, R., Mao, Y., & Tian, S. (2019). Freshness evaluation of three kinds of meats based on the electronic nose. *Sensors*, *19*(3), 605.

[67] Raudienė, E., Gailius, D., Vinauskienė, R., Eisinaitė, V., Balčiūnas, G., Dobilienė, J., & Tamkutė, L. (2018). Rapid evaluation of fresh chicken meat quality by electronic nose. *Czech journal of food sciences*, *36*(5), 420-426.

[68] Rasekh, M., & Karami, H. (2021). E-nose coupled with an artificial neural network to detection of fraud in pure and industrial fruit juices. *International Journal of*

Food Properties, *24*(1), 592-602.

[69] Abdullah, A. H., Sudin, S., Ajit, M. I. M., Saad, F. S. A., Kamaruddin, K., Ghazali, F., ... & Bakar, M. A. A. (2018, August). Development of esp32-based wi-fi electronic nose system for monitoring lpg leakage at gas cylinder refurbish plant. In *2018 international conference on computational approach in smart systems design and applications (ICASSDA)* (pp. 1-5). IEEE.

[70] Hossain, B., Paul, A. K., Islam, M. A., Hossain, M. F., & Rahman, M. M. (2022). Design and analysis of highly sensitive prism based surface plasmon resonance optical salinity sensor. *Results in Optics*, *7*, 100217.

[71] Bolduc, O. R., Live, L. S., & Masson, J. F. (2009). High-resolution surface plasmon resonance sensors based on a dove prism. *Talanta*, *77*(5), 1680-1687.

[72] Singh, P. (2016). SPR biosensors: historical perspectives and current challenges. *Sensors and actuators B: Chemical*, *229*, 110-130.

[73] Singh, Y., Paswan, M. K., & Raghuwanshi, S. K. (2021). Sensitivity enhancement of SPR sensor with the black phosphorus and graphene with bi-layer of gold for chemical sensing. *Plasmonics*, *16*, 1781-1790.

[74] Kumar, R., Pal, S., Prajapati, Y. K., Kumar, S., & Saini, J. P. (2022). Sensitivity improvement of a MXene-immobilized SPR sensor with Ga-doped-ZnO for biomolecules detection. *IEEE Sensors Journal*, *22*(7), 6536-6543.

[75] Yu, H., Chong, Y., Zhang, P., Ma, J., & Li, D. (2020). A D-shaped fiber SPR sensor with a composite nanostructure of MoS2-graphene for glucose detection. *Talanta*, *219*, 121324.

[76] Sepúlveda, B., Angelomé, P. C., Lechuga, L. M., & Liz-Marzán, L. M. (2009). LSPR-based nanobiosensors. *Nano today*, *4*(3), 244-251.

[77] Gazit, N., Klinger, L., & Rabkin, E. (2017). Chemically-induced solid-state dewetting of thin Au films. *Acta Materialia*, *129*, 300-311.

[78] Yadav, M. J., Aravindan, S., & Rao, P. V. (2024). Enhanced control over size, areal density, and shape of substrate-supported Au and Ag nanoparticles by solid-state dewetting and alloying. *Nanotechnology*, *35*(23), 235302.

[79] Pérez-Jiménez, A. I., Lyu, D., Lu, Z., Liu, G., & Ren, B. (2020). Surface-enhanced Raman spectroscopy: benefits, trade-offs and future developments. *Chemical science*, *11*(18), 4563-4577.

[80] Zhang, L., Chang, H., Hirata, A., Wu, H., Xue, Q. K., & Chen, M. (2013). Nanoporous gold based optical sensor for sub-ppt detection of mercury ions. *ACS nano*, *7*(5), 4595-4600.

[81] Senapati, D., Dasary, S. S., Singh, A. K., Senapati, T., Yu, H., & Ray, P. C. (2011). A label - free gold - nanoparticle - based SERS assay for direct cyanide detection at the parts - per - trillion level. *Chemistry–A European Journal*, *17*(30), 8445-8451.

[82] Kaye and Laby, Tables of physical & chemical constants, National Physical Laboratory,

[83] Farnood, A., Ranjbar, M., & Salamati, H. (2020). Localized surface plasmon resonance (LSPR) detection of hydrogen gas by Pd2+/Au core/shell like colloidal nanoparticles. *International Journal of Hydrogen Energy*, *45*(1), 1158-1169.

[84] Su, Y. D., Wuenschell, J., & Ohodnicki, P. (2023, June). Bimetallic nanoparticle-based localized surface plasmon resonance for enhanced sensitivity of reflective fiber optic H2 sensing. In *Optical Waveguide and Laser Sensors II* (Vol. 12532, pp. 20-28). SPIE.

[85] Demirdjian, B., Ozerov, I., Bedu, F., Ranguis, A., & Henry, C. R. (2021). CO and O2 adsorption and CO oxidation on Pt nanoparticles by indirect nanoplasmonic sensing. *ACS omega*, *6*(20), 13398-13405.

[86] Proença, M., Rodrigues, M. S., Vaz, F., & Borges, J. (2021). Carbon monoxide (CO) sensor based on Au nanoparticles embedded in a CuO matrix by HR-LSPR spectroscopy at room temperature. *IEEE Sensors Letters*, *5*(5), 1-3.

[87] Proença, M., Rodrigues, M. S., Meira, D. I., Castro, M. C. R., Rodrigues, P. V., Machado, A. V., ... & Vaz, F. (2022). Optimization of Au: CuO thin films by plasma surface modification for high-resolution LSPR gas sensing at room temperature. *Sensors*, *22*(18), 7043.

[88] Proença, M., Rodrigues, M. S., Moura, C., Machado, A. V., Borges, J., & Vaz, F. (2024). Nanoplasmonic Au: CuO thin films functionalized with APTES to enhance the sensitivity of gas sensors. *Sensors and Actuators B: Chemical*, *401*, 134959.

[89] Karakouz, T., Vaskevich, A., & Rubinstein, I. (2008). Polymer-coated gold island films as localized plasmon transducers for gas sensing. *The Journal of Physical Chemistry B*, *112*(46), 14530-14538.

[90] Chen, B., Ota, M., Mokume, M., Liu, C., & Hayashi, K. (2013). High-speed gas sensing using localized surface plasmon resonance of sputtered noble metal nanoparticles. *IEEJ Transactions on Sensors and Micromachines*, *133*(3), 90-95+6.

[91] Chen, B., Liu, C., Watanabe, M., & Hayashi, K. (2013). Layer-by-layer structured AuNP sensors for terpene vapor detection. *IEEE Sensors Journal*, *13*(11), 4212-4219. 6519263.

[92] Chen, B., Liu, C., Ota, M., & Hayashi, K. (2013). Terpene Detection Based on Localized Surface Plasma Resonance of Thiolate-Modified Au Nanoparticles. *IEEE Sensors Journal, 13*, 1307-1314.

[93] Chen, B., Liu, C., Shang, L., Guo, H., Qin, J., Ge, L., ... & Hayashi, K. (2020). Electric-field enhancement of molecularly imprinted sol–gel-coated Au nano-urchin sensors for vapor detection of plant biomarkers. *Journal of Materials Chemistry C*, *8*(1), 262-269.

[94] Chen, B., Guo, H., Liu, C., Shang, L., Ye, X., Chen, L., ... & Hayashi, K. (2020). Molecularly imprinted sol-gel/Au@ Ag core-shell nano-urchin localized surface plasmon resonance sensor designed in reflection mode for detection of organic acid vapors. *Biosensors and Bioelectronics*, *169*, 112639.

[95] Chen, B., Liu, C., & Hayashi, K. (2014). Selective terpene vapor detection using molecularly imprinted polymer coated au nanoparticle LSPR sensor. *IEEE Sensors Journal*, *14*(10), 3458-3464.

[96] Chen, B., Liu, C., Ge, L., & Hayashi, K. (2016). Localized surface plasmon resonance gas sensor of Au nano-islands coated with molecularly imprinted polymer: Influence of polymer thickness on sensitivity and selectivity. *Sensors and Actuators*

B: Chemical, *231*, 787-792.

[97] Chen, B., Liu, C., Xie, Y., Jia, P., & Hayashi, K. (2016). Localized Surface Plasmon Resonance Gas Sensor Based on Molecularly Imprinted Polymer Coated Au Nano-Island Films: Influence of Nanostructure on Sensing Characteristics. *IEEE Sensors Journal, 16*, 3532-3540.

[98] Shang, L., Liu, C., Watanabe, M., Chen, B., & Hayashi, K. (2017). LSPR sensor array based on molecularly imprinted sol-gels for pattern recognition of volatile organic acids. *Sensors and Actuators B: Chemical*, *249*, 14-21.

[99] Shang, L., Liu, C., Chen, B., & Hayashi, K. (2018). Development of molecular imprinted sol-gel based LSPR sensor for detection of volatile cis-jasmone in plant. *Sensors and Actuators B: Chemical*, *260*, 617-626.

[100] Shang, L., Liu, C., Chen, B., & Hayashi, K. (2018). Plant biomarker recognition by molecular imprinting based LSPR sensor array: performance improvement by enhanced hotspot of Au nanostructure. *ACS Sens.*, *3*, 1531-1538.

[101] Chen, B., Liu, C., Shang, L., Guo, H., Qin, J., Ge, L., ... & Hayashi, K. (2020). Electric-field enhancement of molecularly imprinted sol–gel-coated Au nano-urchin sensors for vapor detection of plant biomarkers. *Journal of Materials Chemistry C*, *8*(1), 262-269.

[102] Chen, B., Guo, H., Liu, C., Shang, L., Ye, X., Chen, L., ... & Hayashi, K. (2020). Molecularly imprinted sol-gel/Au@ Ag core-shell nano-urchin localized surface plasmon resonance sensor designed in reflection mode for detection of organic acid vapors. *Biosensors and Bioelectronics*, *169*, 112639.

[103] Jonas Sandsten, Hans Edner, and Sune Svanberg, "Gas visualization of industrial hydrocarbon emissions," Opt. Express 12, 1443-1451 (2004)

[104] Yang, Z., Soeda, T., Sassa, F., & Hayashi, K. (2019). Development of Odor Visualization System with Two-Dimensional LSPR Gas Sensor for Mobile Robot. In *ISOEN 2019 - 18th International Symposium on Olfaction and Electronic Nose, Proceedings.*

[105] Phan-Quang, G. C., Yang, N., Lee, H. K., Sim, H. Y. F., Koh, C. S. L., Kao, Y. C., ... & Ling, X. Y. (2019). Tracking airborne molecules from afar: three-dimensional metal–organic framework-surface-enhanced Raman scattering platform for stand-off and real-time atmospheric monitoring. *ACS nano*, *13*(10), 12090-12099.

[106] Huang, L., Zhu, Y., Xu, C., Cai, Y., Yi, Y., Li, K., ... & Wang, Y. (2022). Noninvasive diagnosis of gastric cancer based on breath analysis with a tubular surface-enhanced Raman scattering sensor. *ACS sensors*, *7*(5), 1439-1450.

[107] Huang, Y., Xie, T., Zou, K., Gu, Y., Yang, G., Zhang, F., ... & Yang, S. (2021). Ultrasensitive SERS detection of exhaled biomarkers of lung cancer using a multifunctional solid phase extraction membrane. *Nanoscale*, *13*(31), 13344-13352.

[108] Chen L, Guo H, Sassa F, Chen B, Hayashi K. SERS Gas Sensors Based on Multiple Polymer Films with High Design Flexibility for Gas Recognition. Sensors (Basel). 2021 Aug 18;21(16):5546.

[109] Bonvicini, S. N., Fu, B., Fulton, A. J., Jia, Z., & Shi, Y. (2022). Formation of Au, Pt, and bimetallic Au–Pt nanostructures from thermal dewetting of single-layer or

bilayer thin films. *Nanotechnology*, *33*(23), 235604.

[110] Yadav, M. J., Aravindan, S., & Rao, P. V. (2024). Enhanced control over size, areal density, and shape of substrate-supported Au and Ag nanoparticles by solid-state dewetting and alloying. *Nanotechnology*, *35*(23), 235302.

[111] Ray, N. J., Yoo, J. H., McKeown, J. T., Elhadj, S., Baxamusa, S. H., Johnson, M. A., ... & Feigenbaum, E. (2019). Enhanced tunability of gold nanoparticle size, spacing, and shape for large-scale plasmonic arrays. *ACS Applied Nano Materials*, *2*(7), 4395-4401.

[112] Ray, N. J., Yoo, J. H., Baxamusa, S., Nguyen, H. T., Elhadj, S., & Feigenbaum, E. (2021). Tuning gold nanoparticle size with fixed interparticle spacing in large-scale arrays: implications for plasmonics and nanoparticle etching masks. *ACS Applied Nano Materials*, *4*(3), 2733-2742.

[113] Quan, J., Zhang, J., Qi, X., Li, J., Wang, N., & Zhu, Y. (2017). A study on the correlation between the dewetting temperature of Ag film and SERS intensity. *Scientific reports*, *7*(1), 14771.

[114] Kvitek, O., Havelka, V., Vesely, M., Reznickova, A., & Svorcik, V. (2020). Preparation of alloyed and "core-shell" Au/Ag bimetallic nanostructures on glass substrate by solid state dewetting. *Journal of Alloys and Compounds*, *829*, 154627.

[115] Roa, S., & Burgos, M. J. C. (2023). Dewetting regimes in ultra-thin nanocrystalline Ag films. *Materials Letters*, *336*, 133863.

[116] Vazquez-Mena, O., Sannomiya, T., Villanueva, L. G., Voros, J., & Brugger, J. (2011). Metallic nanodot arrays by stencil lithography for plasmonic biosensing applications. *ACS nano*, *5*(2), 844-853.

[117] Jayram, N. D., Aishwarya, D., Sonia, S., Mangalaraj, D., Kumar, P. S., & Rao, G. M. (2016). Analysis on superhydrophobic silver decorated copper oxide nanostructured thin films for SERS studies. *Journal of colloid and interface science*, *477*, 209-219.

[118] Šakalys, R., Kho, K. W., & Keyes, T. E. (2021). A reproducible, low cost microfluidic microcavity array SERS platform prepared by soft lithography from a 2 photon 3D printed template. *Sensors and Actuators B: Chemical*, *340*, 129970.

[119] Im, H., Bantz, K. C., Lindquist, N. C., Haynes, C. L., & Oh, S. H. (2010). Vertically oriented sub-10-nm plasmonic nanogap arrays. *Nano letters*, *10*(6), 2231-2236.

[120] Su, Q., Ma, X., Dong, J., Jiang, C., & Qian, W. (2011). A reproducible SERS substrate based on electrostatically assisted APTES-functionalized surface-assembly of gold nanostars. *ACS applied materials & interfaces*, *3*(6), 1873-1879.

[121] Li, H., Zhang, J., Zhou, X., Lu, G., Yin, Z., Li, G., ... & Zhang, H. (2010). Aminosilane micropatterns on hydroxyl-terminated substrates: fabrication and applications. *Langmuir*, *26*(8), 5603-5609.

[122] Bartschmid, T., Farhadi, A., Musso, M. E., Goerlitzer, E. S. A., Vogel, N., & Bourret, G. R. (2022). Self-assembled au nanoparticle monolayers on silicon in two-and three-dimensions for surface-enhanced Raman scattering sensing. *ACS Applied Nano Materials*, *5*(8), 11839-11851.

[123] Xu, Y., Konrad, M. P., Trotter, J. L., McCoy, C. P., & Bell, S. E. (2017). Rapid One -

Pot Preparation of Large Freestanding Nanoparticle - Polymer Films. *Small*, *13*(2), 1602163.

[124] Lu, X., Huang, Y., Liu, B., Zhang, L., Song, L., Zhang, J., ... & Chen, T. (2018). Light-controlled shrinkage of large-area gold nanoparticle monolayer film for tunable SERS activity. *Chemistry of Materials*, *30*(6), 1989-1997.

[125] Tian, T., Yi, J., Liu, Y., Li, B., Liu, Y., Qiao, L., ... & Liu, B. (2022). Self-assembled plasmonic nanoarrays for enhanced bacterial identification and discrimination. *Biosensors and Bioelectronics*, *197*, 113778.

[126] Leong, S. X., Leong, Y. X., Tan, E. X., Sim, H. Y. F., Koh, C. S. L., Lee, Y. H., ... & Ling, X. Y. (2022). Noninvasive and point-of-care surface-enhanced Raman scattering (SERS)-based breathalyzer for mass screening of coronavirus disease 2019 (COVID-19) under 5 min. *ACS nano*, *16*(2), 2629-2639.

[127] Castro-Grijalba, A., Montes-García, V., Cordero-Ferradás, M. J., Coronado, E., Pérez-Juste, J., & Pastoriza-Santos, I. (2020). SERS-based molecularly imprinted plasmonic sensor for highly sensitive PAH detection. *Acs Sensors*, *5*(3), 693-702.

[128] Liu, Y., Chui, K. K., Fang, Y., Wen, S., Zhuo, X., & Wang, J. (2024). Metal–Organic Framework-Enabled Trapping of Volatile Organic Compounds into Plasmonic Nanogaps for Surface-Enhanced Raman Scattering Detection. *ACS nano*, *18*(17), 11234-11244.

[129] Samal, A. K., Polavarapu, L., Rodal-Cedeira, S., Liz-Marzán, L. M., Pérez-Juste, J., & Pastoriza-Santos, I. (2013). Size Tunable Au@ Ag core–shell nanoparticles: synthesis and surface-enhanced raman scattering properties. *Langmuir*, *29*(48), 15076-15082.

[130] Haldar, K. K., Kundu, S., & Patra, A. (2014). Core-size-dependent catalytic properties of bimetallic Au/Ag core–shell nanoparticles. *ACS applied materials & interfaces*, *6*(24), 21946-21953.

[131] Ma, Y., Li, W., Cho, E. C., Li, Z., Yu, T., Zeng, J., ... & Xia, Y. (2010). Au@ Ag core–shell nanocubes with finely tuned and well-controlled sizes, shell thicknesses, and optical properties. *ACS nano*, *4*(11), 6725-6734.

[132] Awiaz, G., Lin, J., & Wu, A. (2023, February). Recent advances of Au@ Ag core–shell SERS - based biosensors. In *Exploration* (Vol. 3, No. 1, p. 20220072).

[133] He, L., Gao, C., Yang, L., Zhang, K., Chu, X., Liang, S., & Zeng, D. (2020). Facile synthesis of MgGa2O4/graphene composites for room temperature acetic acid gas sensing. *Sensors and Actuators B: Chemical*, *306*, 127453.

[134] Khojier, K. (2017). Sol-gel spin coating derived ZnO thin film to sense the acetic acid vapor. *International Journal of Nano Dimension*, *8*(2), 164-170.

[135] Wang, C., Ma, S., Sun, A., Qin, R., Yang, F., Li, X., ... & Yang, X. (2014). Characterization of electrospun Pr-doped ZnO nanostructure for acetic acid sensor. *Sensors and Actuators B: chemical*, *193*, 326-333.

[136] Proença, M., Rodrigues, M. S., Meira, D. I., Castro, M. C. R., Rodrigues, P. V., Machado, A. V., ... & Vaz, F. (2022). Optimization of Au: CuO thin films by plasma surface modification for high-resolution LSPR gas sensing at room temperature. *Sensors*, *22*(18), 7043.

[137] Yuan, H., Li, N., Fan, W., Cai, H., & Zhao, D. (2022). Metal - organic framework based gas sensors. *Advanced Science*, *9*(6), 2104374.

[138] Shen, Y., Tissot, A., & Serre, C. (2022). Recent progress on MOF-based optical sensors for VOC sensing. *Chemical Science*, *13*(47), 13978-14007.

[139] Chen, Q. Q., Hou, R. N., Zhu, Y. Z., Wang, X. T., Zhang, H., Zhang, Y. J., ... & Li, J. F. (2021). Au@ ZIF-8 core–shell nanoparticles as a SERS substrate for volatile organic compound gas detection. Analytical Chemistry, 93(19), 7188-7195.

[140] Zhang, Y., Wang, M., San, X., Zhang, L., Wang, N., Wang, G., ... & Shen, Y. (2024). Highly selective gas sensors for formaldehyde detection based on ZnO@ ZIF-8 core-shell heterostructures. Sensors and Actuators B: Chemical, 398, 134689.

[141] Jin, L., Yang, K., Chen, L., Yan, R., He, L., Ye, M., ... & Zhang, K. (2023). Flexible synergistic MoS2 quantum dots/PEDOT: PSS film sensor for acetaldehyde sensing at room temperature. Analytical Chemistry, 95(23), 8859-8868.

[142] Seekaew, Y., Lokavee, S., Phokharatkul, D., Wisitsoraat, A., Kerdcharoen, T., & Wongchoosuk, C. (2014). Low-cost and flexible printed graphene–PEDOT: PSS gas sensor for ammonia detection. Organic Electronics, 15(11), 2971-2981.

[143] Li, J., Wu, J., Zhang, X., Liu, Y., Zhou, D., Sun, H., ... & Yang, B. (2011). Controllable synthesis of stable urchin-like gold nanoparticles using hydroquinone to tune the reactivity of gold chloride. *The Journal of Physical Chemistry C*, *115*(9), 3630-3637.

[144] Tian, L., Sun, Y., Huang, H., Guo, X., Qiao, Z., Meng, J., & Zhong, C. (2020). Porous ZIF - 8 Thin Layer Coating on ZnO Hollow Nanofibers for Enhanced Acetone Sensing. *ChemistrySelect*, *5*(8), 2401-2407.

[145] Chen, Z., Liu, W., Si, X., Guo, J., Huo, J., Zhang, Z., ... & Du, Z. (2023). In situ assembly of one-dimensional Pt@ ZnO nanofibers driven by a ZIF-8 framework for achieving a high-performance acetone sensor. *Nanoscale*, *15*(42), 17206-17215.

[146] Liu, T., Jia, X., Zhang, J., Yang, J., Wang, S., Li, Y., ... & Song, H. (2022). Selective detection of ethanol at low concentration by ZnO@ ZIF-8 porous nanosheets. *Sensors and Actuators B: Chemical*, *372*, 132661.

[147] Ren, G., Li, Z., Yang, W., Faheem, M., Xing, J., Zou, X., ... & Du, Y. (2019). ZnO@ ZIF-8 core-shell microspheres for improved ethanol gas sensing. *Sensors and Actuators B: chemical*, *284*, 421-427.

[148] Kou, H., Shao, T., Dong, J., Zhang, F., Tian, S., & Wang, X. (2024). Highly Sensitive Ethylene Glycol Gas Sensor Based on MIL-68 (In)@ ZIF-8 Derivative. *ACS sensors*.

[149] Wang, P., Li, R., Cheng, X., Wang, Y., Wang, Q., Wu, Z., ... & Xie, E. (2023). High Response of ZIF-8-Derived ZnO Nanorods to Low-Concentration Ethylene Glycol. *ACS Applied Nano Materials*, *6*(23), 22069-22079.

[150] Li, J., Zhong, J., Huang, W., Xu, R., Zhang, Q., Shao, H., & Gu, X. (2014). Study on the development of ZIF-8 membranes for gasoline vapor recovery. *Industrial & Engineering Chemistry Research*, *53*(9), 3662-3668.

[151] Zhang, D., Kang, Z., Liu, X., Guo, J., & Yang, Y. (2022). Highly sensitive ammonia sensor based on PSS doped ZIF-8-derived porous carbon/polyaniline hybrid film coated on quartz crystal microbalance. *Sensors and Actuators B: Chemical*, *357*, 131419.

[152] Qin, Z., Cao, R., Zhang, P., Qiu, M., & Li, M. (2024). Development and characterization of ZIF-8/WS2 composites for NH3 detection at room temperature. *Materials Letters*, *372*, 137010.

[153] Seekaew, Y., Lokavee, S., Phokharatkul, D., Wisitsoraat, A., Kerdcharoen, T., & Wongchoosuk, C. (2014). Low-cost and flexible printed graphene–PEDOT: PSS gas sensor for ammonia detection. *Organic Electronics*, *15*(11), 2971-2981.

[154] Bai, H., & Shi, G. (2007). Gas sensors based on conducting polymers. *Sensors*, *7*(3), 267-307.

[155] Gao, F., Yang, J., Tu, X., Yu, Y., Liu, S., Li, M., ... & Lu, L. (2021). Facile synthesis of ZIF-8@ poly (3, 4-ethylenedioxythiophene): poly (4-styrenesulfonate) and its application as efficient electrochemical sensor for the determination dichlorophenol. *Synthetic Metals*, *277*, 116769.

[156] Zhang, D., Kang, Z., Liu, X., Guo, J., & Yang, Y. (2022). Highly sensitive ammonia sensor based on PSS doped ZIF-8-derived porous carbon/polyaniline hybrid film coated on quartz crystal microbalance. *Sensors and Actuators B: Chemical*, *357*, 131419.

[157] Zong, C., Xu, M., Xu, L. J., Wei, T., Ma, X., Zheng, X. S., ... & Ren, B. (2018). Surface-enhanced Raman spectroscopy for bioanalysis: reliability and challenges. *Chemical reviews*, *118*(10), 4946-4980.

[158] Shi, S., & Russell, T. P. (2018). Nanoparticle assembly at liquid–liquid interfaces: From the nanoscale to mesoscale. *Advanced Materials*, *30*(44), 1800714.

[159] Liu, D., Cai, W., Marin, M., Yin, Y., & Li, Y. (2019). Air - liquid interfacial self - assembly of two - dimensional periodic nanostructured arrays. *ChemNanoMat*, *5*(11), 1338-1360.

[160] Chen, X. X., & Huang, J. (2019). Odor source localization algorithms on mobile robots: A review and future outlook. *Robotics and Autonomous Systems*, *112*, 123-136.

[161] Jing, T., Meng, Q. H., & Ishida, H. (2021). Recent progress and trend of robot odor source localization. *IEEJ Transactions on Electrical and Electronic Engineering*, *16*(7), 938-953.

[162] Terutsuki, D., Uchida, T., Fukui, C., Sukekawa, Y., Okamoto, Y., & Kanzaki, R. (2021). Real-time odor concentration and direction recognition for efficient odor source localization using a small bio-hybrid drone. *Sensors and Actuators B: Chemical*, *339*, 129770.

[163] Xing, L., Xiahou, Y., Zhang, P., Du, W., & Xia, H. (2019). Size control synthesis of monodisperse, quasi-spherical silver nanoparticles to realize surface-enhanced Raman scattering uniformity and reproducibility. *ACS applied materials & interfaces*, *11*(19), 17637-17646.

[164] Xu, Y., Konrad, M. P., Lee, W. W., Ye, Z., & Bell, S. E. (2016). A method for promoting assembly of metallic and nonmetallic nanoparticles into interfacial monolayer films. *Nano Letters*, *16*(8), 5255-5260.

[165] Lin, X., Fang, G., Liu, Y., He, Y., Wang, L., & Dong, B. (2020). Marangoni effect-driven transfer and compression at three-phase interfaces for highly reproducible

nanoparticle monolayers. *The Journal of Physical Chemistry Letters*, *11*(9), 3573-3581.

[166] Yang, Z., Sassa, F., & Hayashi, K. (2018). A robot equipped with a high-speed LSPR gas sensor module for collecting spatial odor information from on-ground invisible odor sources. *ACS sensors*, *3*(6), 1174-1181.

[167] Chen, Q. Q., Hou, R. N., Zhu, Y. Z., Wang, X. T., Zhang, H., Zhang, Y. J., ... & Li, J. F. (2021). Au@ ZIF-8 core–shell nanoparticles as a SERS substrate for volatile organic compound gas detection. *Analytical Chemistry*, *93*(19), 7188-7195.

[168] Ye, J., Bonroy, K., Nelis, D., Frederix, F., D'Haen, J., Maes, G., & Borghs, G. (2008). Enhanced localized surface plasmon resonance sensing on three-dimensional gold nanoparticles assemblies. *Colloids and Surfaces A: Physicochemical and Engineering Aspects*, *321*(1-3), 313-317.

[169] Kang, M., Park, S. G., & Jeong, K. H. (2015). Repeated solid-state dewetting of thin gold films for nanogap-rich plasmonic nanoislands. *Scientific reports*, *5*(1), 14790.

[170] Hincheeranan, W., Chananonnawathorn, C., Duangkanya, K., Waiwijit, U., Wongpanya, K., Amarit, R., ... & Horprathum, M. (2024). A study of multiple solid-state dewetting of sputtered Au ultra-thin films for chip-based LSPR sensor applications. *Optical Materials*, *157*, 116137.

[171] Pal, A., Roshini, R. A., & Varma, M. M. (2024). De-wetted gold nanostructures for SERS-based sensing of static and dynamic targets. *Applied Surface Science*, *678*, 161096.

[172] Chen, Z., Zhang, F., Lu, Y., Li, Y., Liu, G., Shan, J., & Liu, Q. (2022). Bioelectronic modulation of single-wavelength localized surface plasmon resonance (LSPR) for the detection of electroactive biomolecules. *Chinese Chemical Letters*, *33*(6), 3144-3150.

Acknowledgements

After completing my undergraduate studies, I experienced uncertainty about my future path. The opportunity to study in Japan, immerse myself in a different culture, conduct research, and pursue a doctoral degree was beyond my expectations - all of which would not have been possible without the support of my professors, colleagues, and family.

I am deeply thankful to Professor Kenshi Hayashi for providing me with the opportunity to research gas sensors and guiding me through complex experimental design and implementation. His mentorship enhanced my understanding of sensor development and applications, while his patience and encouragement allowed me to freely explore my ideas. His steadfast support, both academically and emotionally, helped me overcome challenges and persevere through my doctoral research.

Special thanks to Associate Professor Bin Chen, whose thoughtful advice and expertise in nanomaterial and sensor fabrication significantly improved the quality of my research. Additionally, I am grateful for the insights of Associate Professor Fumihiro Sassa, whose suggestions helped refine my work.

The staff members of the Hayashi and Sassa Laboratory were instrumental in my academic journey. Ms. Maiko Moribe facilitated my transition to Japan and provided valuable support. Mr. Shigeru Kaneko and Ms. Yuuko Saruwatari ensured the availability of necessary equipment and materials, enabling efficient research progress.

During my doctoral studies, I encountered numerous challenges and am grateful to those who helped me overcome them. Dr. Lingpu Ge, with whom I collaborated the longest in Japan, inspired me with his persistence and dedication. I also thank Dr. Ye Xiao for his theoretical insights that broadened my perspective, and Dr. Lin Chen and Mr. Cong Wang for their assistance with data analysis. Ms. Shiyi Zhang provided valuable suggestions for my experiments, and I appreciate Mr. Zeping Yu and other laboratory members for their encouragement and collaboration.

I am especially thankful to my roommate, with whom I lived for five years. We supported each other through tough times and shared many happy moments. Over these years, we moved homes twice, helped each other in everyday life, and often went for walks together to relax. Last year, I attended

his wedding and was thrilled to see him so happy and confident. Just two months ago, his child was born, and I am extremely happy for him. I truly wish him and his family a bright and happy future.

Finally, I would like to express my deepest gratitude to my parents and grandparents. Their unwavering love and support have been the strongest foundation throughout my journey of growth.

With less than ten days until the traditional Chinese New Year, I extend my heartfelt wishes for a prosperous year ahead. I will continue to strive forward, aspiring to become someone who can make meaningful contributions to society.